DECAY OF IMPRINTED SURFACE WAVES IN POLYMERS: A METHOD TO PROBE NEAR-SURFACE DYNAMICS

Dissertation

zur Erlangung des Grades

”*Doktor der Naturwissenschaften*”

am Fachbereich Chemie und Pharmazie

der Johannes Gutenberg-Universität

in Mainz

Kirstin Petersen

geboren in Aachen

Mainz 2003

”If you don’t make mistakes you are not working on hard enough problems,

and that’s a big mistake.”

Frank Wilczek

Contents

1. INTRODUCTION

Polymers are widely used in industry and science. The easy processing, as well as the variety of unique properties, has been the focus of much research in industry and academia. One of these unique and attractive properties is the strong dependence of mechanical and optical properties on the temperature. For amorphous polymers the drastic change in polymer properties upon heating occurs at the glass "transition" temperature. Since this transition is not a true transition as defined by thermodynamics, the characteristic temperature will be referred to as the glass temperature, abbreviated as T_{g}. Well below T_{g}, the polymer is brittle and hard, above T_{g} it is soft, easy to form and tacky.

The temperature dependent properties have to be taken into consideration and can be very useful in polymer processing. However, following the trend toward miniaturization, the use of polymeric materials brings up new problems. The failure of miniaturized devices can be prevented if the properties of confined polymers are known. It has to be checked if confinement, in the form of a surface, an interface, or a thin film has an influence on the properties of the material. This is especially true for polymers with their large intrinsic length scales, for example the radius of gyration [Fer80]. The radius of gyration is a few nanometers and thus the range of perturbation by a surface or interface is much larger than in metals or crystals with short intrinsic length scales. Confined polymers could therefore have characteristics different from the bulk. This could result in a change in T_{g}, segmental mobility and relaxation time, amongst others.

Polymers in confined geometries have attracted the interest of many scientists and some controversial results are discussed in chapter 2. Still no single theory for these phenomena has been agreed upon.

An all inclusive model describing the behavior of polymers under confinement would not only be useful for material processing but it could also enlighten one's understanding of the fundamental processes in polymeric materials and macromolecular physics.

The research presented in this work focuses on surface-induced confinement of poly(methyl methacrylate) (PMMA) and polystyrene (PS). The work is arranged into two parts.

The first section focuses on the influence of surface perturbations on T_g.
The effect of the polymer chain length and chain entanglement with respect to the magnitude of this effect is investigated by a series of measurements performed with different molecular weights below and above the entanglement molecular weight.
Investigations on the possible influence of the technique on the resulting surface glass temperature will also be presented. It may be that a reduction of the probing depth increases the surface effect.

In the second section the dynamics at the surface are investigated. One of the favored explanations for a decrease in T_g near the surface is an enhanced mobility of the polymer chains at the free surface. An enhanced mobility should affect the relaxation times and thus the dynamics of the polymer. Measurements for PMMA and PS related to the surface dynamics are presented. The validity of time-temperature superposition (TTS) for the surface relaxation processes of PMMA and PS is checked for a series of molecular weights. The shift factors extracted from the TTS are analyzed in respect to free volume, expansion, activation energies for relaxation processes, and fragilities.

2. LITERATURE OVERVIEW: Current Status

This chapter is an overview on the research published in the field of polymers in confined geometry.

The first part of this chapter gives an overview of the literature concerning glass temperatures, T_gs.
In the second part literature is presented which describes dynamic effects occurring under confined geometry as found at surfaces and in thin films. Publications dealing with deviations from, and conformity with, the bulk behavior in diffusive processes, mobilities, and activation energies will be covered in this part of the overview.

Glass Temperatures

The techniques and methods to determine the T_g for thin films and surfaces are numerous and so are the results, which do not always agree. The techniques usually detect discontinuities in second derivatives of the free energy. These are changes in heat capacity and expansivity or changes in properties related to them, such as refractive index, viscosity, and diffusivity.

The technique most obvious for the determination of the T_g in thin films is, in analogy to bulk determinations, a differential scanning calorimeter (DSC). Efremov and coworkers [EWO+02] designed a calorimeter for ultrathin films and remedied the lack of sensitivity by using Micro-Electro-Mechanical Systems-technology (MEMS-technology). MEMS-technology is the integration of mechanical elements, sensors, actuators, and electronics on a common silicon substrate through the utilization of microfabrication technology. The results for polydisperse polystyrene (PS) revealed both an increased T_g and an increased fictive temperature for thin films in comparison to the bulk. The fictive temperature is the temperature of intersection of the extrapolated equilibrium liquid and glass enthalpy versus temperature curves - the fictive equilibrium transition temperature.

Measurements performed by Grohens et al. [GBL+98], using ellipsometry also point toward a T_g differing from the bulk value. This was found using PMMA with different tacticities on various substrates. Polymer films with thicknesses between 20 and 40 nm showed an increased T_g in the case of iso- and a-tactic PMMA, and a decreased T_g in the case of syndiotactic PMMA on silicon and on aluminum substrates. An influence of the tacticity on T_g might be assumed but a deviation of the thin film T_g caused by the interaction of the polymer with the substrate might also be a reason for the varying T_g.

Wallace and coworkers [WZW95] and Tsui and Zhang [TZ01] investigated the dependence of T_g on the film thickness with X-ray reflectivity and ellipsometry measurements, respectively. Both groups obtained a decreasing T_g, reducing the film thickness of monodisperse PS films on silicon. The experiments of Tsui and Zhang cover thin film T_gs at two different film thicknesses for a wide range of molecular weights (13.7 to 2300 kg/mol).

Jones and coworkers tested thin supported PS films with ellipsometry for a thickness dependence of T_g. The experiments revealed an increasing reduction of T_g with decreasing film thickness [KJ01]. They found not only the reduction in T_g but also that the width of the transition increases with decreasing film thickness.

The question of how much the interface influences the thin film properties, and T_g in particular, was addressed by Fryer and coworkers [FPK+01]. Changing the interface properties by altering the silicon substrate with a hexadimethylsilane (HDMS) coating, revealed an effect opposite to the one on a bare silicon substrate. Comparing it with the bulk value, on silicon the thin film T_g of PS was higher, whereas on the HDMS treated silicon surfaces it was lower [FNdP00]. X-ray exposures of variable doses applied to octadecyltrichlorosilane (OTS) covered silicon substrates altered the properties of the OTS films and with it the interfacial energy at the polymer-substrate interface. PS and PMMA samples, prepared on the modified substrates were investigated with thermal probe analysis, ellipsometry, and X-ray reflectivity. In comparison with bulk measurements the thin film T_g was lower for small values of interfacial energy and higher than the bulk T_g for stronger interactions. The strength of the effect increased with decreasing thickness.

By means of uncovered and sandwiched layers of deuterated PS, Zheng and coworkers [ZRS97] as well as Pochan et al. [PLSW01] investigated sub- and superstrate interactions. The measurements confirmed the *three layer model*, which describes the material properties of thin supported films. The material properties are altered within a characteristic distance from the in-

terface as well as within a certain distance from the surface; the layer in-between is unperturbed and bulk-like. This model is also supported by experiments of the group of deMaggio [DFG97]. Their positronium annihilation lifetime analysis of silicon supported PS suggests a 5 nm substrate and a 2 nm surface perturbation. Dielectric loss spectroscopy analysis of supported PS layers also corroborates the three layer model [FM00b]. Grafting the polymer films to the substrate gives even longer characteristic distances, within which the T_g is disturbed [TFP$^+$01]. The results from these references show how much influence the substrate can have on the properties of a thin film. Theory also supports the dependence of T_g on the substrate for thin films [TNdP00]. The calculations point to a reduction of T_g in the case of a weak attraction and an increase in T_g in the case of a strong attraction between the substrate and the polymer chains.

Trying to understand the confinement effect, it is helpful to separate substrate and surface effects, which is difficult in the case of thin supported films.

When the perturbation actually provoked by the geometric confinement at the surface shall be investigated one has to avoid substrate interactions. This requirement is fulfilled in thin free-standing films or surfaces of thick films. For the surface investigations, films much thicker than the range of the interaction with the substrate are used. Free-standing films have the advantage of two surfaces, which enhances the perturbation on the thin film.

A considerable number of papers concerning free-standing films have been published. Brillouin light scattering experiments on free-standing PS films with varying thickness also support the model of a perturbed, liquid-like surface layer [FDVSD96], [FM00a]. Forrest and coworkers stated an enhancement of the surface effect comparing free-standing films with uncapped and capped supported films of PS [FDVD97] and found a special morphology in symmetrically capped thin free-standing PS films [DVND99].

Surface confinement may not be the only cause for the free-standing film results. Free-standing films are usually floated off a substrate. The removal of water or solvents is difficult without changing or even rupturing the thin film. Residual water or solvent in the polymer would act as a plasticizer and decrease T_g [PN96]. Another influence on the T_g of thin, free-standing films could be stress in the unsupported film caused by gravity.

Several methods of acquiring information from thick supported films have been described. Zaporojtchenko and coworkers looked for changes in X-ray photo-emission intensities from embedded noble metal clusters in PS and PC surfaces to determine T_g. Scanning force measurements, for example lateral force microscopy and shear modulation force microscopy, have

been reported extensively. Surprisingly, Overney et al. [GPZ+00], [OBLD00] could not sense any difference of T_g in comparison with the bulk values, whereas the numerous publications of Kajiyama and coworkers found a reduced T_g at the surface [TTG+96], [KTT97], [STK99], [TTK00].

In these experiments a possible influence of the probe (metal cluster or AFM tip) cannot be ruled out. Making the interaction as small and well defined as possible using small probes with a particular geometry can diminish this problem.

Therefore the best way to probe surface T_g's might be a techniques without direct contact to the polymer. Kim and coworkers carried out X-ray photon-correlation spectroscopy on PS films and could not find evidence for a reduced surface T_g [KRL+].

The problem, whether surfaces affect the T_g at all, seems still not completely resolved. One way to get more insight is to not only investigate perturbations of T_g but also to have a closer look into other anomalies such as the dynamics in confined geometry. This topic is covered in the second part of the literature overview. Anomalies in surface dynamics would be apparent in altered diffusion coefficients, relaxation times, mobilities, activation energies or fragilities, to mention some examples.

Surface Dynamics

To corroborate a difference between the T_g of the bulk and the surface and to exclude that possible changes of T_g at a surface are caused by the probing technique, it is necessary to confirm the difference in T_g with different dynamical properties at the polymer surface compared to the bulk. Thus, a reduced T_g at the surface should be correlated with an increased mobility of the polymer chains or of large chain segments.

An influence of confinement on the dynamics in thin films, in particular on the diffusion processes, is claimed for low molecular weight PS in a publication by Tseng and coworkers [TTD00]. The tracer diffusion experiments reveal that the mobility of polymer chains in thin films increases with decreased PS film thickness on quartz samples.

Molecular-dynamic simulations of Varnik *et al.* [VBB02] predict this enhanced mobility of polymer segments close to a wall. The higher mobility of the polymer segments close to the wall trigger the motion of adjacent segments and provoke an overall acceleration of the thin film dynamics. Different dynamics in thin films can be inferred, as well, from the activation enthalpy determined by fitting ultrathin film DSC data obtained at different cooling rates [EWO+02]. The

fitting was performed using the Tool-Narayanaswamy-Moynihan (TNM) model [Moy94]. The algorithm is described in [Hod94]. The activation enthalpy obtained from ultrathin film DSC is significantly smaller than the one obtained from conventional DSC.
Dielectric relaxation processes in thin PS films [FM00b] give evidence for a correlation between a reduced T_{g} and the distribution of α relaxation times. The influence of the interface on the thin film properties must not be ignored in the just mentioned techniques.

The mobility of polymers at the surface can be investigated by different techniques. The technique used by Kerle *et al.* [KLKR01] was to artificially roughen a PS surface and investigate the structural changes upon annealing by AFM in tapping mode. They found a partial relaxation at temperatures below the bulk T_{g} and also a dependence of the rate and the degree of terminal relaxation on the annealing temperature and observed a structure size dependent mobility driven by enthalpy.

Viscoelasticity measurements by means of friction force microscopy from Haugstad et al. [HHG] on PMMA and PS surfaces point to an enhanced molecular freedom at the surface in comparison with the bulk. They explain activation energies for PMMA differing from the bulk by a hindered rotation of the $-COOCH_3$ groups. The relation between the friction coefficient and the α and β relaxation processes is described by the same group in [HMG96] and [HGH99].

A whole series of investigations on surface relaxation processes and mobilities was performed by the Kajiyama group [TTK97], [KTST98], [Tan00], [JYT$^+$01]. They correlate the reduced surface T_{g} with a reduced activation energy for α relaxation process, which reveals not only a localization of chain end groups but also a reduced cooperativity at the surface as interpreted by the Ngai coupling model [NRP98]. They also showed a strong dependence of T_{g} on the end groups and their concentration at the surface. A less pronounced surface effect in the case of polydisperse PS is explained by the chemical structure of the chain end groups.

Two methods without direct mechanical interactions with the polymer surface are X-ray reflectivity [GSG$^+$00] and near edge X-ray absorption fine structure (NEXAFS) analysis [LRS$^+$97] used by Geue and coworkers and Liu et al., respectively. The X-ray reflectivity measurements were performed with dye induced holographic gratings and showed an enhanced mobility. However, this might also be caused by the dye acting as a plasticizer. The NEXAFS investigations for high molecular weight PS did not show a significant difference in segmental mobility between bulk and surface.

It is conspicuous, that the investigation methods that do not mechanically interact with the surface do not show a clear surface anomaly in the case of PS. This seems to be the case for T_g and the surface dynamics. Further research is required to provide satisfactory explanations.

3. EXPERIMENTAL TECHNIQUES AND MODES OF MEASUREMENT

In this chapter the experimental foundations for this work are laid. This work concentrates on the changes of polymer gratings investigated by laser diffraction and AFM analysis. The production of polymer gratings is described, which consists of the polymer film preparation and the hot-embossing with a lithographically produced master. Some details about the master preparation are given. The experimental setup used for the hot-embossing and the laser diffraction experiments is presented. The two modes of measurements, quasi-static measurements to determine an estimate for T_{g} at the surface and dynamic measurements to investigate the relaxation behavior of polymers at a surface, are introduced.

3.1 Experimental Techniques

3.1.1 Sample and Master Preparation

Polymer Film Preparation

The preparation of polymer films on silicon substrates was performed for all the experiments. Silicon was used as a substrate because the native oxide layer of the silicon is very smooth (rms roughness $\approx$ 1 nm) and the area where a grating was imprinted is apparent. The smooth oxide layer was assumed to be helpful for the preparation of smooth polymer films. However, not only the smoothness of the substrate but also the the polymer-substrate interaction plays an important role in the film preparation. The interaction determines the stability of the polymer film. Polymers with hydrophilic or polar side chains prefer hydrophilic substrates for example a native oxide layer of a silicon wafer. In order to prepare stable films of hydrophobic or non polar polymers on the native oxide layer of a silicon wafer a hydrophobic substrate is

necessary such as a hydrogen terminated silicon [MIST+01]. The different properties of the two polymers used in this work, poly(methyl methacrylate) (PMMA) and polystyrene (PS), require a different substrate treatment before the spincasting procedure.

Atactic, monodisperse PMMA and PS of molecular weights (M_w) below and above the entanglement molecular weight (M_e) [Mar96], were purchased from Polymer Standard Service (PSS, Mainz, Germany). Characteristics of the materials are listed in the Tabs. 3.1 and 3.2.

M_w(kg/mol)	4.2	14.0	23.2	65.0	M_e=10 -11 kg/mol
D= M_w/M_n	1.09	1.03	1.03	1.03	
R_g(nm)	1.85	3.33	4.27	7.07	
$T_{g,bulk}$(°C)	97±2	117±2	118±2	123±2	

Table 3.1: Characteristics of PMMA: molecular weight M_w, entanglement molecular weight M_e [Mar96], polydispersity index D, radius of gyration R_g [KKI75], and bulk glass temperature $T_{g,bulk}$ measured with differential scanning calorimetry and extrapolated to a zero heating rate.

M_w(kg/mol)	3.47	10.3	18.0	34.0	65.0	M_e=13 kg/mol
D= M_w/M_n	1.06	1.03	1.04	1.04	1.02	
R_g(nm)	1.6	2.8	3.8	5.2	7.1	
$T_{g,bulk}$(°C)	75±2	94±2	97±2	100±2	103±2	

Table 3.2: Characteristics of PS, variables as in table 3.1, R_g of PS is calculated according to [DFG97].

PMMA and PS were chosen to investigate the influence of the side chain. Both polymers have the same backbone structure with different side chains. The weight of the repeating units is similar, 100 g/mol for PMMA and 104 g/mol for PS. The entanglement molecular weight of PMMA and PS are also in the same molecular weight range. Thus, the requirement for investigations of the side chain influence is met. The structure of PMMA and PS is given in Fig. 3.1.

Figure 3.1: The structure of the repeat unit of PMMA (left-hand side) and PS (right-hand side) differs in the side groups.

The sample preparation is demanding in respect to cleanliness and film thickness. Special care has to be taken not to contaminate the samples and to prepare films with a thickness, such that the properties at the surface will not be influenced by a possible interaction of the polymer with the substrate. Contaminants introduced at any point during or after the sample preparation procedure will move to the surface and possibly distort the properties or induce dewetting [dG85], [Mit93], [ANK95], [GNPJ97], [Her99], [MG00], [SHJ01]. The substrate influence (for example a change in T_{g} and/or a reduced mobility due to adhesion) usually has a range of not more than few 100 nm. This can be estimated from experiments with altered properties of the substrate polymer interface as Keddie et al. [KJC94] and Fryer et al. [FNdP00] showed for PS and PMMA. Effects on the surface properties caused by the substrate is circumvented by preparing the polymer films with a thickness above 1 μm. The large film thickness also has the welcome side effect that a slight tilt of the master in respect to the polymer surface is not so critical anymore, since the master can sink into the hot, soft polymer.

To prepare the PMMA samples, the silicon wafers were cut, ultrasonically cleaned in Chloroform ($CHCl_3$), and dried with nitrogen (N_2). PMMA of varying M_{w} was dissolved in $CHCl_3$ at a concentration of 90 mg polymer/l ml solvent. It was then stirred for more than two hours and spincast at 400 rpm onto the silicon substrates. The optimum values for the spincasting parameters, which are the concentration of the polymer solution and the speed of rotation, were determined by a calibration series. The calibration curve was used to make a prediction of the final film thickness and its dependence on concentration and speed of rotation. The thickness was determined with a surface profiler (KLA Tencor, San Jose, U.S.A.).

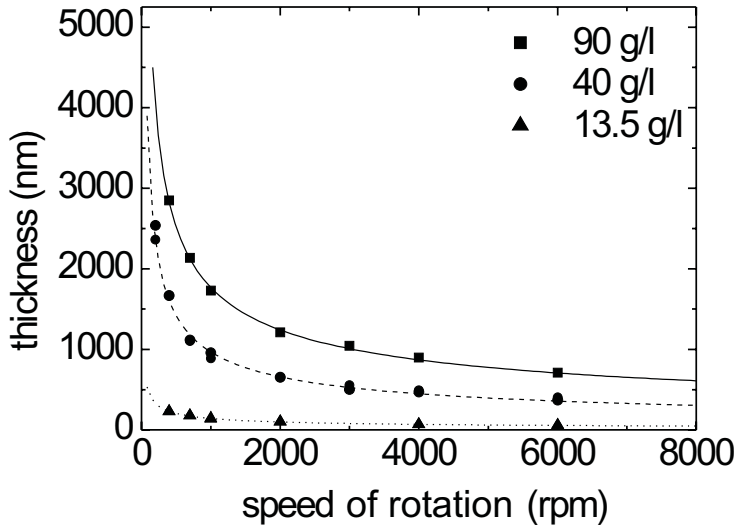

Figure 3.2: Calibration curve for spincasting: thickness in dependence on concentration and speed of rotation for PMMA with M_w=65.0 kg/mol. The lines are a guidance for the eye.

The calibration curve for PMMA with M_w of 65.0 kg/mol, Fig. 3.2, shows that the choice of a speed of 400 rpm and a concentration of at least 90 mg/1 ml results in a film thickness above 2 μm. The resulting film thickness is thus sufficient to decouple the near-surface dynamics from the substrate influence. Even if the master sinks into the polymer film during the embossing process, the necessary thickness for decoupling is still guaranteed. Thickness also depends on molecular weight, but it is only necessary to ensure a minimum thickness, and this was double-checked with the profiler after the spincasting.

Even though the spinning speed is chosen to be very low, the films are smooth. Surface profiler measurements revealed an upper limit of the root-mean square (rms) roughness of some nm (ca. 5 nm). The final step for the film preparation is annealing under vacuum for 12 hours at 100 °C to remove residual solvent or water. The annealing step also reduces the surface roughness.

The preparation of the PS films was more complicated. Bubble development and dewetting seriously inferred with the formation of smooth films when preparing PS the same way as the PMMA samples. It is possible that a thin solvent layer remained on the substrate. Upon heating the film, the residual solvent layer evaporated and caused the formation of bubbles. The dewetting is explained by the hydrophobic character of PS, the adhesion between substrate and polymer films is too small and prevents the film from staying on the sample.

Cleaning the substrates in a different way, namely with a 2 % v/v solution of Hellmanex (HELLMA, Germany), a cationic detergent, in the ultrasonicator bath with a following rinsing series in MilliQ water, a final sonication in ethanol, and annealing at 180 °C under vacuum after the cleaning procedure, prevented the mentioned problems. AFM force-distance curves show that the Hellmanex treatment changes the surface chemistry. The comparison of force curves taken before and after the treatment shows a large change in the adhesive contribution, Fig. 3.3.

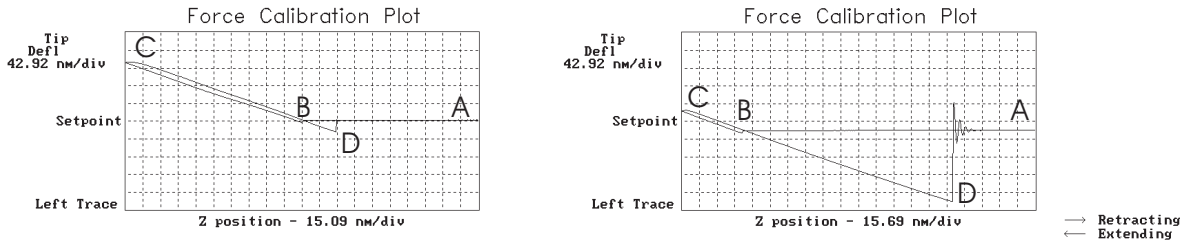

Figure 3.3: AFM force distance curves (deflection vs. z-piezo travel) for a bare silicon surface (left-hand side) and a Hellmanex treated silicon surface (right-hand side) measured with the same cantilever. The curve for the bare master shows the typical features: A→B: approach of cantilever, B: ”snapping” into contact with the surface, B→C: increased bending/deflection of the cantilever, C→D: reduced and then inverted bending/deflection of cantilever after crossing the abscissa due to adhesion, ”sticking”, D: ”snapping” from the surface and D→A: retraction of the free cantilever. For the untreated silicon substrate, the tip shows little interaction with the surface, revealed in the small features at B and D. The features at B and D are pronounced after the Hellmanex treatment - showing strong adhesion between tip and surface. The same cantilever with a spring constant k=48 N/m (MikroMasch, Estonia) was used for both force curves.

After the Hellmanex cleaning procedure a smooth film could be prepared without bubble formation or dewetting. The residual solvent in the subsequently applied polymer was finally removed by a second annealing of the film under vacuum at 100 °C for 12 h, as was performed with the PMMA films.

For clarity table 3.3 comprises all the important steps of the sample preparation for PMMA and PS.

PMMA	PS
• ultrasonic cleaning of Si substrates in ClCH_3	• ultrasonic cleaning of Si substrates in Hellmanex
	• rinsing in MilliQ
	• ultrasonic cleaning and rinsing in ethanol
• drying with N_2	• drying with N_2
	• vacuum annealing at 180 °C for 12 h
• spin casting: 90 mg/1 ml PMMA/ClCH_3 at 400 rpm	• spin casting: 90 mg/1 ml PS/toluene at 400 rpm
• vacuum annealing at 100 °C for 12 h	• vacuum annealing at 100 °C for 12 h

Table 3.3: Sample preparation steps for PMMA and PS.

Master Preparation

The detailed protocol for the preparation of sinusoidally corrugated masters with photolithography can be found in the thesis of Mark Hamdorf [Ham99]. Here, only some additional details for the master treatment prior to hot-embossing will be described.

The master gratings have to be covered with a thin anti-adhesive coating. Two different coatings were tested in preparation for this work: ultra-thin polytetraflouroethylene (PTFE)-like films deposited by plasma polymerization and self assembled fluoro-silane monolayers.

The PTFE-like films can be obtained by reactive sputtering [LFW78] or plasma polymerization [NKCD92],[GSS96]. The teflon-like test films were deposited by Zhihong Zhang. The anti-adhesive property of the PTFE-like film is very good, however, there is the disadvantages of a very soft film and the unavoidable transfer of small fluorinated entities from the coated master to the replica [JSS$^+$99]. It is also possible that the thin films are not homogeneous. The polymer properties, which shall be investigated, are distorted in the case of a transfer of teflon-like material from the master to the polymer surface. The polymer chains from the coating material change the surface energy of the polymer film, which is the object of investigation. This makes the material unfavorable for this purpose.

Fluoro-silane (Tridecafluoro-1,1,2,2-tetrahydroctyl)-triethoxysilane ($C_{14}H_{19}F_{13}O_3Si$) (ABCR, Karlsruhe, Germany) treatment provided a more suitable antiadhesive surface. The masters

were cleaned carefully and the silane deposited from the gas phase under Ar atmosphere overnight. A final curing at 110 °C for one hour was necessary to fix the silane layer. The final coating should be less than 1 nm thick, very smooth and consequently the surface structure of the master is hardly altered. The latter was verified by AFM imaging which shows no recognizable difference while the altered surface property is reflected in the force-distance curves obtained before and after silanizing. Figure 3.4 shows a comparison of the two force-distance curves. The curves show that the adhesive forces are strongly reduced after the coating is applied.

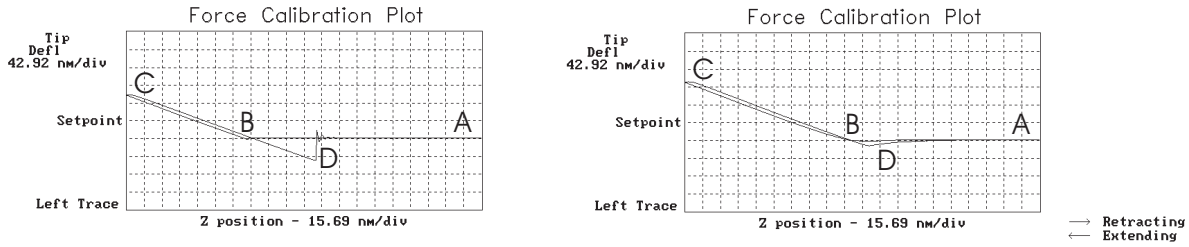

Figure 3.4: AFM force-distance curves (deflection vs. z-piezo travel) for the bare master (left-hand side) and the silanized master (right-hand side) measured with the same cantilever. The force-distance curve for the bare master shows the typical features: A→B: approach of cantilever, B: ”snapping” into contact with the surface, B→C: increased bending/deflection of the cantilever, C→D: reduced and then inverted bending/deflection of the cantilever after crossing the abscissa due to adhesion, ”sticking”, D: ”snapping” from the surface and D-A: retraction of the free cantilever. For the silanized master, the tip shows little interaction with the surface. The features at B and D are much smaller than in the case of the untreated master. The strongly reduced adhesion and only the bending of the cantilever determines the shape of the force-distance curve.

The features caused by the interaction of the cantilever tip with the surface disappear: The ”snapping” (point B in the left-hand graph of Fig. 3.4) of the cantilever into contact with the surface in the advancing is already very small for the bare master. This ”snapping”, as well as the ”sticking” to the surface when retracting the cantilever (point D in the graphs of Fig. 3.4) is strongly reduced after silanizing the master. Double checking of the antiadhesive property of the master with contact angle measurements gave a change of the angle from less than 80° to above 100° after silanizing, which is in good agreement with values stated in literature [ZAL$^+$97].

The strong covalent -Si-O-Si- bond should prevent the transfer of material from the master to the polymer surface as soon as all the surplus material from the silanizing step is removed. The

first imprinting procedure after silanizing the master takes away the surplus silane material and contaminates the sample. This sample was discarded. The following imprints do not show any changes in properties for example in the decay behavior of the polymer grating. This showed that the surface viscosity was not altered by material coming off the master. An additional benefit of the anti-adhesive coating is its protective character for the master.

In order to reduce the probing depth of this technique, gratings with smaller grating constants are necessary. Apart from the photo-lithographic masters, stepped silicon masters with smaller grating constants were used to imprint structures. These masters were produced by annealing slightly miscut (cut with few degrees in respect to a low index plane) silicon wafers in ultra high vacuum. The annealing time determines the step width of the surface structure. The stepped silicon masters used for hot embossing had grating constants between 40 and 200 nm and were produced in Bayreuth (Andreas Hund und Chun Wang from the group of Prof. Krausch). However, the structures are not sinusoidal but triangular and the periodicity of the stepped silicon gratings was not so accurate. The amplitudes were very small, decreasing with decreasing grating constant. Consequently, the Fourier transform is not only one sharp peak but is a broader distribution of peaks with lower intensity. This made any investigation of changes in structure much more complicated. For this reason only the results for experiments with lithographically produced masters are presented.

3.1.2 Experimental Setup

The setup is composed of two parts. The embossing unit and the detection unit.

The embossing unit consists of a heatable stage, on which the sample can be mounted, as well as of a heatable embossing bolt with the master attached to it. The sample is clamped to the heating stage with two brass plates, which are attached to the stage with screws. The sample is slightly pressed against the heating stage to ensure good thermal contact avoiding breakage of the sample. The master fixed on a metal holder was placed upside down and good thermal contact was achieved. The master holder can tilt in one direction, so that the surface of the master can adjust to the polymer surface to ensure optimum contact for the hot embossing process. An illustration of the embossing unit is given in Fig. 3.5.

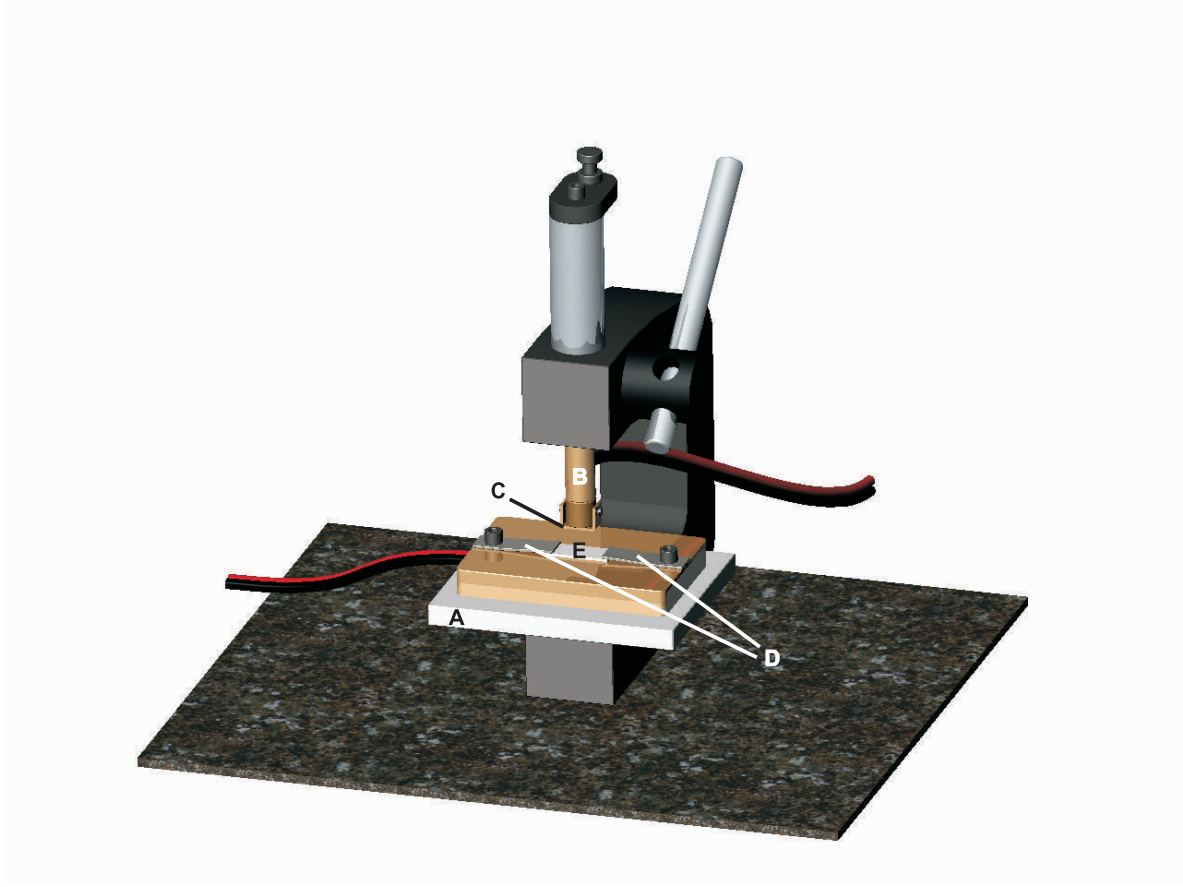

Figure 3.5: Experimental Setup: Embossing unit. The main parts of the embossing unit are a heatable stage (A), a heatable embossing bolt (B), the master holder with the master fixed to it (C), and two brass plates (D), which slighly pressed the sample (E) to the heating stage.

The heating of the embossing unit is controlled by two homebuilt temperature units. The temperature units are linearized and have a temperature stability of 0.1 °C in the experimental range from room temperature to 200 °C. The whole heating procedure is automated and controlled by a computer. Both temperature ramps and constant temperatures can be programmed.

To investigate the polymer grating decay under a well controlled temperature the detection units were necessary. Figure 3.6 shows a sketch of the optical unit for the observation of the grating decay by detecting the diffracted intensity:

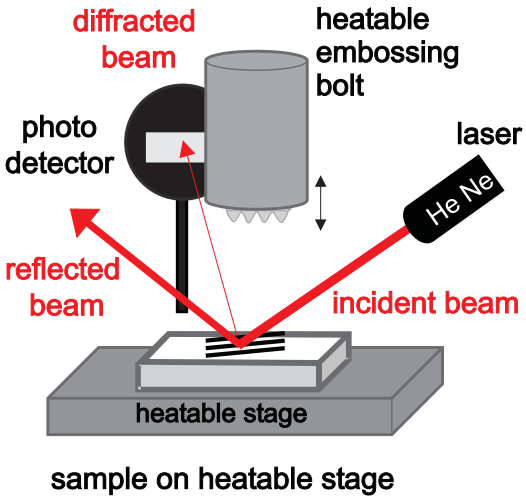

Figure 3.6: Experimental Setup: Detection unit.

The main parts of the optical detection unit are a Helium-Neon laser, a photo diode, a beam chopper and a lock-in amplifier. The laser light is modulated by the beam chopper and directed through an aperture via a mirror onto the sample. The diffracted light from the grating is detected by the photodiode. The spectral response, the linearity, and the temperature effect have to be considered when choosing the right diode. The appropriate diode's sensitive area is small ($2.4 \times 2.4\ mm^2$). The photodiode is placed close to the grating in such a way that the photo diode does not get so hot that a thermal background is induced. Heat can thermally excite electron-hole pairs and thus increase the dark current. The maximum temperature of the detector was 40°C, which is within the optimum operating range. The AC voltage from the photodiode, created by the modulated intensity is amplified with a lock-in amplifier, $EG\&G\ 5210$, (time constant $\tau_{lock-in}$ = 300 ms) and recorded by the computer.

The diffraction efficiency is proportional to the square of the grating amplitude. Thus, changes in the gratings with a grating constant close to the wavelength of the laser light can be detected with the diffraction unit. The out-of-plane angle between the incident laser light and the grating plane and the in-plane angle of the grating have to be aligned so that the wave vectors match and yet a diffracted intensity is detectable and also not blocked by the embossing bolt. At an incidence angle of approximately 22 degrees, the diffracted spot on the detector is slightly elongated and the diffraction efficiency is reduced in comparison to perpendicular incidence. The voltage from the photo diode resulting from the grating diffraction at room temperature is

about 1 mV. The background voltage without diffracted signal about $10^{-5}V$, which gives an initial signal-to-background ratio of approximately 100. The signal-to-noise ratio decreases with progressing decay of the grating. The way to extract information from the diffracted intensity data is described in Secs. 3.2.1 and 3.2.2.

Investigations of gratings with grating constants much smaller than the wavelength of the HeNe-laser were performed with an atomic force microscope (AFM). The first method considered for carrying out experiments on smaller grating constants, to increase the surface sensitivity, was small angle X-ray scattering. The contrast between air and a single polymer surface, however, is very small and very long data collection times of at least a day are necessary. A difference between the polymer grating before and after a thermally induced decay could be probed. To reduce the measurement time, investigations of small grating amplitudes in combination with high temperature requires high intensity X-ray sources such as a synchrotron. The disadvantage of the high intensity radiation is a possible change of the polymer structure and properties. Consequently, it was refrained from X-ray investigations and AFM measurements were preferred instead.

A comprehensive review covering AFM is given in [She00]. In this work the AFM is mainly operated in contact mode. Contact mode can be measured with constant height (z-piezo position) detecting the deflection, known as constant height contact mode, and with constant force (deflection) detecting the height (z-piezo movement), referred to as constant force contact mode. In this case for topography measurements the constant force mode was applied. The force of the sample exerted on the tip is kept constant and very small by a feedback loop. Information about the average grating amplitude can be extracted from the topography images by performing a power spectral density analysis. The power spectral density (PSD) is the square of the modulus or the Fourier transform of the surface structure. Changes in the PSDs reflect changes in the surface structure. A sinusoidal grating appears as a single peak in the PSD at a wavelength equaling the grating constant. The decrease in the average grating amplitude can thus be determined by analyzing the PSD at the wavelength of the grating. PSDs and diffracted intensities both give information about the surface, since they are proportional to the square of the surface's Fourier transform and thus it is easy to compare the results of the different probing methods. The only difference is the interaction with the sample (optical or mechanical). The analysis is explained in Sec. 3.2.1.

3.1.3 Hot Embossing

There are several different ways to produce a grating on the surface of a polymer film such as photo-lithography [Ham99], ion- [GMF+01] or e-beam lithography [PCT99], [MT97], [CMLP97], [CP98], [DFM+98], [CWS90], [ARA+95], [OBT+98], X-ray lithography [SHS+89], [Hec98], SPM lithography [NFC+99], [LFH+99], [WQSK98], contact imprinting [BCW+98], [WCBB99], and cold molding [KL00]. A prerequisite for the investigations, which shall be performed on the gratings, is that the polymer properties are original and unperturbed. Most of the techniques cannot fulfill this prerequisite. For example cross-linking (specially in the case of high energy methods like ion-, e-beam and X-ray lithography), residual solvent in the polymer grating, and a lack of reproducibility are present.

The method which perturbs the polymer the least is hot embossing [CKR95], [CKR96], [CK97], [KC97], [JSGS98], [SJDG99], [KhHL99].
Hot embossing is a low cost, highly reproducible technique to nano-mold a thermoplastic polymer. It is well-suited to produce low aspect ratio structures. The sample and the master are heated above T_{g} so that the polymer is soft enough to be molded. This is referred to as the embossing temperature. It is important to let the sample and the master reach the embossing temperature before slowly lowering the master into the soft polymer melt. Heating the sample and the master with the master already in contact with the polymer prevents a proper embossing procedure by thermal expansion of the polymer and occasionally by vaporizing solvent or water left in the polymer film. The interplay of capillary and compressive effects in the polymer film confined between master and sample provokes viscous fingering and patterns similar as in [SHdMG01]. Residual water in the polymer film is more critical for PMMA, which has a hydrophilic side chain. The removal of water trapped in the samples is another advantage of the hot embossing technique over other techniques.

The duration of the embossing procedure also has to be chosen carefully. The duration should be longer than the ”terminal relaxation time” of the polymer to give the polymer chains the chance to relax completely in the new surface relief structure [Ham99]. The ”terminal relaxation time” of a polymer is shorter the more the embossing temperature exceeds T_{g}.

One aspect to be considered in respect to perturbation of the polymer properties is the temperature memory [Fer80]. The memory effect can influence the properties of a polymer at a certain temperature. Heating the polymer above T_{g} for longer than the ”terminal relaxation

time", ensures total relaxation, consequently the memory is lost. As soon as the sample is cooled below T_g the state at T_g is frozen in. The system has a memory of the state at T_g. It is important that the temperature ramping for the embossing step is not performed too fast. A controlled heating is indispensable, not only since a well-controlled ramping is only possible when the whole system can follow the set temperature but also because of the temperature memory. The state frozen in at T_g depends on the cooling rate, so the temperature parameters have to be standardized.

The standard parameters chosen for the embossing process were a heating rate of 3 °C/min, a final embossing temperature of 160 °C and a embossing duration of 2 hours. Embossing durations longer than two hours did not show any different results. However, for the low molecular polymer samples, in particular in the case of PS with a molecular weight of 3.47 kg/mol, a lower embossing temperature was used, so as to avoid dewetting of the polymer film. The low molecular weight PS (3.47 kg/mol) was embossed with a temperature of 130 °C. Total relaxation of the low molecular weight material is still guaranteed since the T_g is lower and its relaxation times at this temperature are comparable to the ones of higher molecular weight at the higher embossing temperature. After the embossing time has elapsed there are two ways to continue depending on the experiments:

1) For quasi-static measurements to determine the glass temperature (Secs. 3.2.1 and 5.1.1) the temperature is lowered from the embossing temperature to room temperature at the same rate as it was raised. At room temperature the master can be taken off uncovering the fresh grating. The typical course of the temperature for a ramping experiment is depicted in the left-hand graph of Fig. 3.7.

2) The dynamic measurements for the mastering and the determination of the Arrhenius behavior or the fragility require a constant temperature at which the decay of the grating can be detected. It is preferable to avoid rapid changes in temperature to reach the required decay temperature since these changes induce thermal stress in the polymer sample. Another disadvantage of using temperature jumps to reach the decay temperature is the partial decay which already takes place during the time until the decay temperature is reached. Consequently, the initial state of the grating is not well-defined due to the impossibility of perfect temperature jumps.

The advantage of the hot embossing technique is the possibility to reach the decay temperature without prior partial decay and, even more important, the possibility to let the system reach equilibrium at the decay temperature before the master is lifted and the decay initiated. Thus, the sample-master assembly is only cooled to the desired decay temperature, close to the T_g of the polymer, with a rate of 3°C/min. The system is left at this decay temperature for about one hour to reach equilibrium. The master is then lifted off the hot sample and the decay of the grating is detected immediately. The temperature course for a dynamic measurement consisting of the hot embossing procedure with the subsequent transition and equilibration at the temperature chosen for the decay is plotted in the graph on the right-hand side of Fig. 3.7.

Letting the sample equilibrate before investigating the grating's decay at a constant temperature is only possible with the hot embossing technique. Using other techniques the grating is produced at room temperature and the only way to perform measurements at a temperature close to T_g is to expose the system to an imperfect temperature jump.

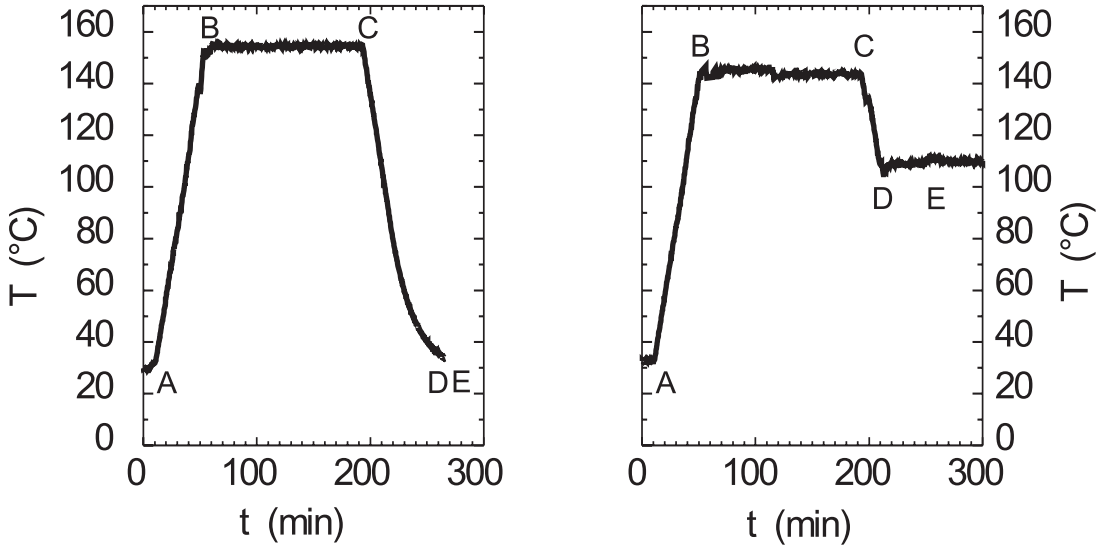

Figure 3.7: Typical course of the sample temperature during an embossing procedure for quasi-static (left graph) and dynamic measurements (right graph), A→B: heating, B: master lowered onto polymer film, B→C: embossing, C→D: cooling, E: removal of the master

For the laser-diffraction measurements (5.1.1, 5.2) gratings with a grating constant close to the wavelength of the laser light are needed. The grating constant chosen in this case is 641 nm. The vertical amplitude of the 641 nm gratings is $5 - 15$ nm, which is small enough to

ensure local flatness and avoid non-linear flow behavior.

The second type of gratings used, were gratings with a smaller grating constant, namely 267 nm and with a higher aspect ratio. The grating amplitude was $20 - 30$ nm. These gratings were used to perform experiments with AFM as a detection technique (5.1.2).

Polymer gratings, which were hot embossed with these two types of gratings, are shown in Fig. 3.8, the line scans in Fig. 3.9 for the gratings show the different aspect ratios of 0.02 and 0.10, respectively.

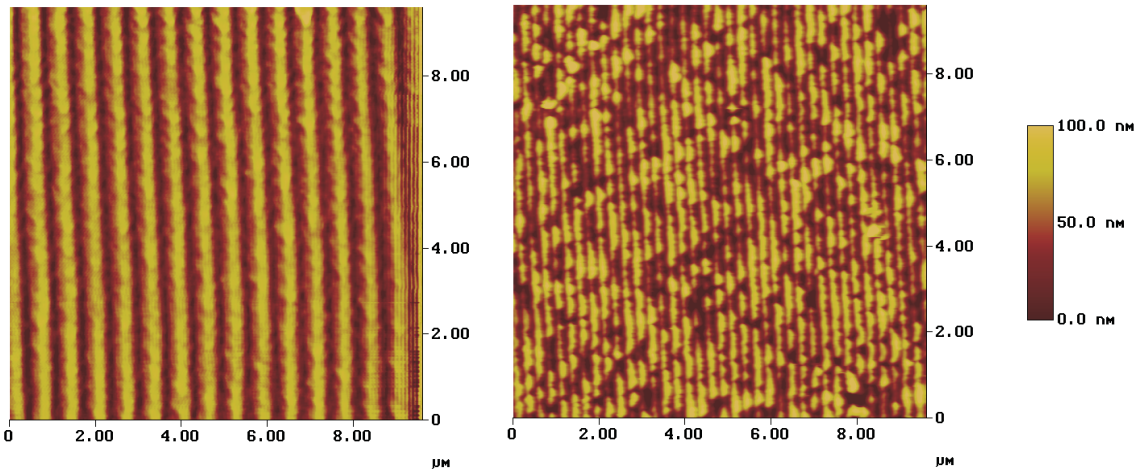

Figure 3.8: Hot embossed polymer films with grating constants of 641 nm (left image) and 267 nm (right image).

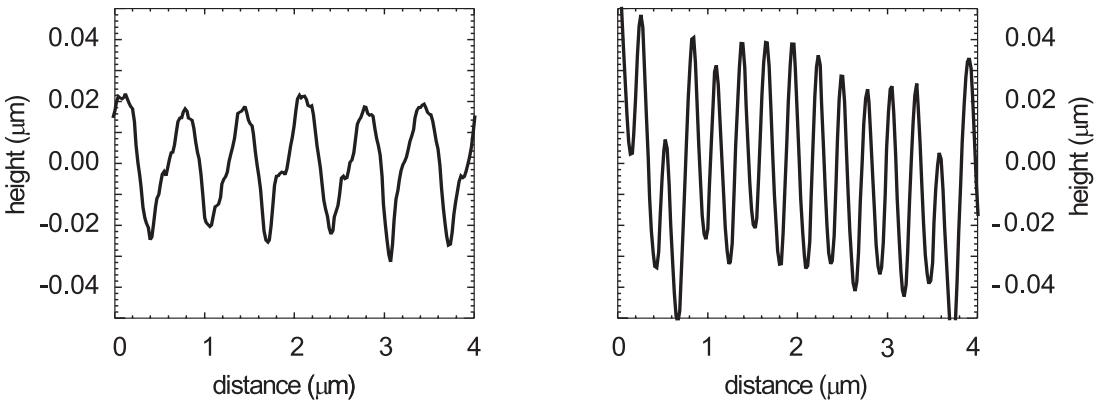

Figure 3.9: Line scans from gratings with average grating constants of 641 nm (left image) and 267 nm (right image).

3.2 Modes of Measurement

3.2.1 Quasi-Static:

Temperature Ramps and an Estimate for Surface Glass Temperature - T_{dec}

Surface tension and viscosity determine the structure of the surface during the decay. This is described in more detail in the theory part of this work, Sec. 4.1. The viscosity can be seen as a resistance to a shape change of the surface structure, the surface tension promotes small curvatures and drives the smoothing of the surface. At temperatures at which viscosity prevails no change of the surface structure will occur. As soon as the temperature is high enough for the enhanced mobility of the polymer chains, surface tension dominates the decay process and the surface will start to smooth out.

This is the effect which the T-ramp experiments make use of. For a wide range of temperatures, well below T_{g}, temperature does not have a noteworthy effect on the surface structure and the amplitude of the polymer grating, since the viscosity of the polymer is very high. At temperatures around T_{g} the viscosity reduces by many orders of magnitude and structural changes driven by the surface tension occur, resulting in a rapid change of the amplitude of the corrugated grating at the surface.

The temperature of the sample is continuously increased with a small, constant heating rate. The temperature at the sample surface is recorded simultaneously with the diffracted signal from the surface corrugation grating. This measurement provides data about the temperature dependent changes of the surface structure. The temperature at which a distinct decrease or decay of the grating amplitude takes place will hereafter be called the decay temperature, T_{dec}.

The technique to gain information about the surface corrugation grating, in particular about the amplitude, was chosen depending on the grating constant. For the 641 nm gratings it was laser diffraction, for the 267 nm gratings atomic force microscopy was used. The extraction of data for the two different investigation methods will be described in the following.

Laser-Diffraction Analysis

The temperature dependence of the amplitude can be investigated employing laser diffraction with a He-Ne-laser only for the larger grating constant of 641 nm. The diffracted intensity

is proportional to the square of the surface's Fourier transform at the inverse grating constant [SPT+95]. A data set with simultaneously recorded diffracted intensity and substrate temperature with time is plotted in Fig. 3.10.

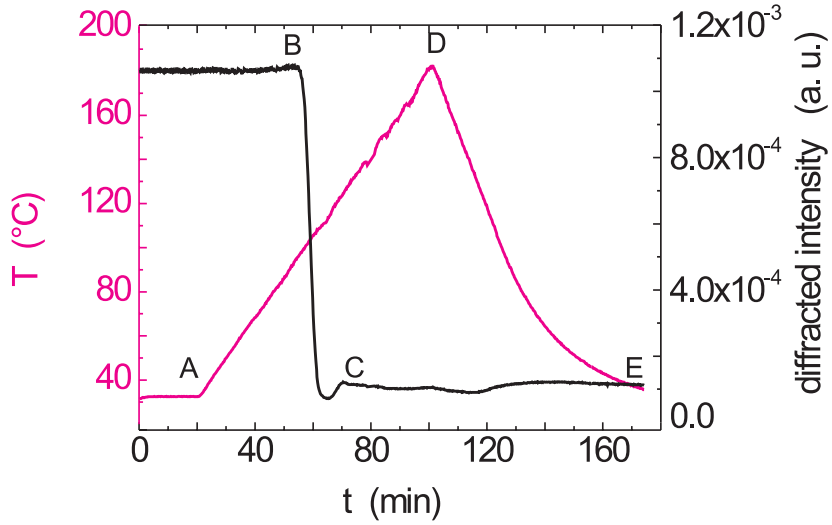

Figure 3.10: Typical data set for ramping experiments recording the diffraction intensity (gray) and the temperature (black) versus time. A: T=30 °C, amplitude $u_{\mathrm{t}=0} \approx 10$ nm, ramp start, B: T_{dec}, grating starts to decay, C: total decay of the corrugation, D: maximum temperature, E: T=30 °C, $u_{\mathrm{t}} \approx 0$ nm no detectable diffraction efficiency. The variations in intensity after the grating is erased are most probably due to changes in diffuse scattering caused by changes in the surface roughness.

The temperature T_{dec} extracted from such a data set is illustrated in Fig. 3.11. The intensity from the temperature ramp curve is plotted versus the corresponding temperature. T_{dec} can be determined by extrapolation of the glassy behavior and the transition region to the liquid state. The decay temperature is the intersection temperature of the linear extrapolated glassy (line parallel to the x-axis through initial intensity) and transition zone (inclined line through the steep drop of intensity).

A second way to extract an estimated surface glass temperature from the decay data is by fitting the intensity curves by a function, which describes a transition. The two standard functions are the error function and the tanh function. The tanh function is used here and the intensity normalized to the initial intensity I_0 is fit by $I_{\mathrm{norm}}(T) = \frac{I}{I_0}(T) = \frac{1}{2}(1 - tanh(\frac{T-T_1}{T_2}))$. The temperature T_1 is the inflection point of the tanh function and corresponds to the center of the transition. The value T_2 is a measure for the width of the transition. The points $T_1 \pm T_2$ are the

points of intersection between the tangent to $I_{\mathrm{norm}}(T)$ at $T = T_1$ and the asymptotes $I_{\mathrm{norm}} = 1$ and $I_{\mathrm{norm}} = 0$. Thus the width of the transition is $\Delta T_{\mathrm{dec,fit}} = (T_1 + T_2) - (T_1 - T_2) = 2T_2$. The right graph in Fig. 3.11 shows a fit intensity curve. $T_{\mathrm{dec,fit}}$=$T_1 - T_2$ is a second estimation for the surface glass temperature. This method may be not as accurate as the first one since the whole curve is fit and the $\frac{S}{N}$-ratio decreases with decreasing grating amplitude. However, using this analysis additional information is gained, *e.g.* the width of the transition zone, $\Delta T_{\mathrm{dec,fit}}$=$2T_2$.

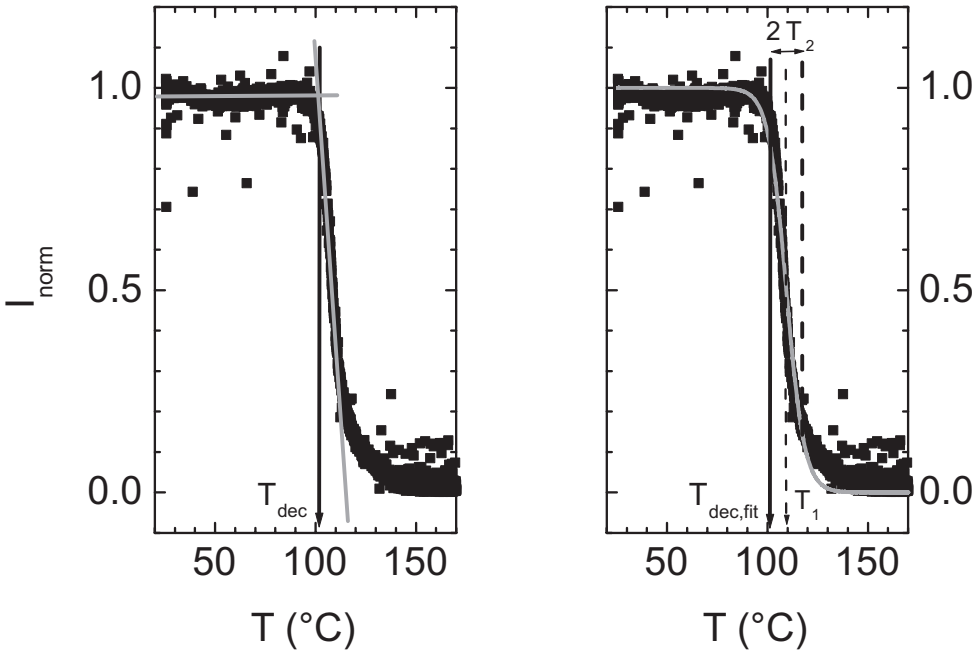

Figure 3.11: Extraction of T_{dec} and $T_{\mathrm{dec,fit}}$ from the temperature ramp data. In the left-hand graph the extraction of T_{dec} by means of linear extrapolation of the initial glassy region and the transition zone (grey lines) is shown. The intersection temperature of the two extrapolated lines is called T_{dec}. The right graph shows the data fit by a tanh-function: $I_{\mathrm{norm}} = \frac{I}{I_0} = \frac{1}{2}(1 - tanh(\frac{T-T_1}{T_2}))$. The temperature $T_{\mathrm{dec,fit}} = T_1 - T_2$ and additionally to the other method also the width of the transition region $\Delta T_{\mathrm{dec,fit}}$=$2T_2$ can be extracted. The temperature ramp data for PMMA of M_{w} = 4.2 kg/mol data shown in the two graphs is measured at a heating rate of 0.1 °C/min.

Ramping experiments with detection of the diffraction efficiency at different ramping rates between 0.1 °C/min and 5 °C/min are performed for each molecular weight. The decay temperature, T_{dec}, is further used to estimate the surface glass temperature. The T_{dec}s for the different ramping rates do not show a specific dependence and thus are extrapolated linearly to find a T_{dec} at a 0 °C/min ramping rate, $T_{\mathrm{dec},0}$. This is an estimate for the surface glass temperature. The extrapolation is done in analogy to differential scanning calorimetry (DSC) measurements,

generally used to determine the bulk glass temperature. These are also performed at different heating rates and extrapolated to a 0 °C/min heating rate. The extrapolated glass temperature for the bulk will be called $T_{\mathrm{g,bulk}}$ in the following discussion.

AFM Analysis

The temperature dependence of the grating's amplitude for a heating rate of 1 °C/min was also investigated with AFM. Special requirements for the heating stage and the tips have to be fulfilled. It necessary that the heating stage is thermally insulated to prevent piezo-drifts and oscillations and the tips have to be uncoated or coated with the same material all over to avoid deflection caused by thermal expansion of the coating material. Still, thermal convection of the air, thermal motion of the tip and reduced sample temperature beneath the tip make accurate measurement difficult in trying to obtain good AFM images at elevated temperatures. Since attempts to determine the surface structure of the grating at elevated temperatures while ramping the temperature were not satisfactory another way was chosen to get to the information needed. In order to avoid all the complications and possible artifacts, the AFM imaging was performed at room temperature. The gratings are heated, quenched and imaged to ascertain the temperature dependent changes in amplitude. This guarantees that the changes in amplitude, which are small, are not obscured by instrumental artifacts. The best way to mimic the continuous temperature ramp is the following stepwise procedure: The topography of the sample is measured at room temperature, the sample removed from the AFM and the grating specimen is put in a heat box for a fixed time (5 or 10 min) at a certain temperature, quenched to room temperature and measured again. The temperature of the heat box is increased by a fixed amount (5 or 10 °C) and the procedure repeated until the topography images reveal that the grating completely decayed. It is assumed that the state of the sample right before quenching is conserved and thus can be measured at room temperature.

One source of error are local variations of the grating's amplitude, either already existent on the master or caused during the embossing process. Thus, two main requirements are essential to make this type of analysis with AFM feasible: On the first instance scanning over a large area reduces the influence of local heterogeneity on the average amplitude. Otherwise choosing distinct features on the sample surface, *i.e.* landmarks, ensures measurement of the same region on the sample after each heating step. An actual disadvantage of the quenching method is the delay with which the sample will reach the heat box's temperature. Under the prerequisite of

a large heat capacity of the heat box and a quick insertion and withdrawal of the sample, this method turned out to be the best compromise.

The AFM images are analyzed extracting the power spectral densities (PSDs). The power spectral density is the square of the Fourier transform of the surface and gives insight into the distribution of wavelengths on the sample surface. The grating determines the most frequent wavelength.

A typical data set for the ramping experiments measured by AFM, with the PSD at the grating constant plotted versus the temperature, is demonstrated in Fig. 3.12:

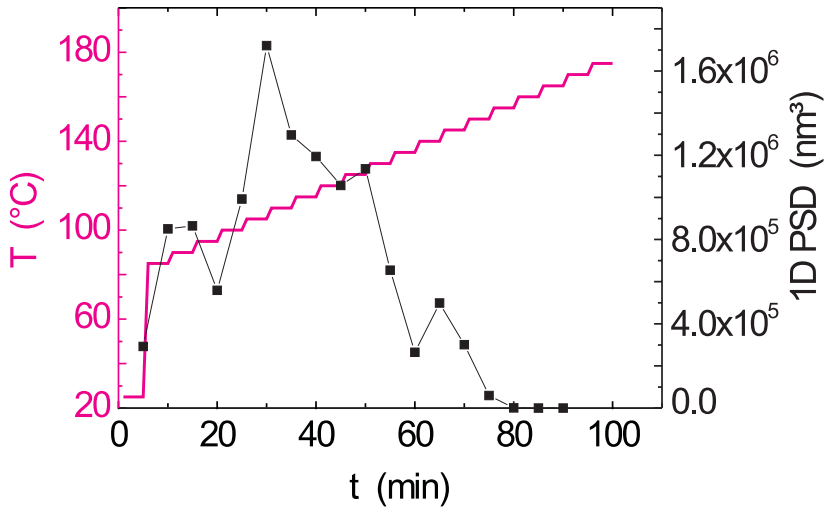

Figure 3.12: Typical data set for ramping experiments analyzing a AFM power spectral density (solid squares with line) and the temperature (stepped line) versus time

The information received from the two different investigation methods, PSDs from AFM images and diffraction efficiency, are much alike since both represent squares of the Fourier transform of the corrugated surface. The difference is the probe-sample interaction and the range of grating constants possibly investigated. One way to make it possible to compare AFM measurements of gratings with a small grating constant and diffraction experiments is to calibrate the AFM measurements. This calibration basically excludes the differences in probe - sample interaction by comparison of AFM and diffraction measurements performed with the same grating constant.

3.2.2 Dynamic:
Constant Temperature, Mastering, Activation Energies and Fragilities

The dynamic measurements observe the decrease of the grating's amplitude at a constant temperature close to $T_{\mathrm{dec},0}$. These kinds of measurements are only performed with the 640 nm gratings using diffraction as the detection technique. After the embossing process the temperature is lowered to a value close to $T_{\mathrm{dec},0}$. The system is left at this temperature for about an hour to equilibrate before the master is lifted off the sample. If the viscosity close to $T_{\mathrm{dec},0}$ is low enough, the decay of the grating is driven by the surface tension. In Fig. 3.13 a typical data set for an embossing procedure with a subsequent decay measurement is displayed. The small step, at about 260 min, on the left-hand side of the intensity jump, is the intensity scattered of the embossing bolt after opening the laser shutter.

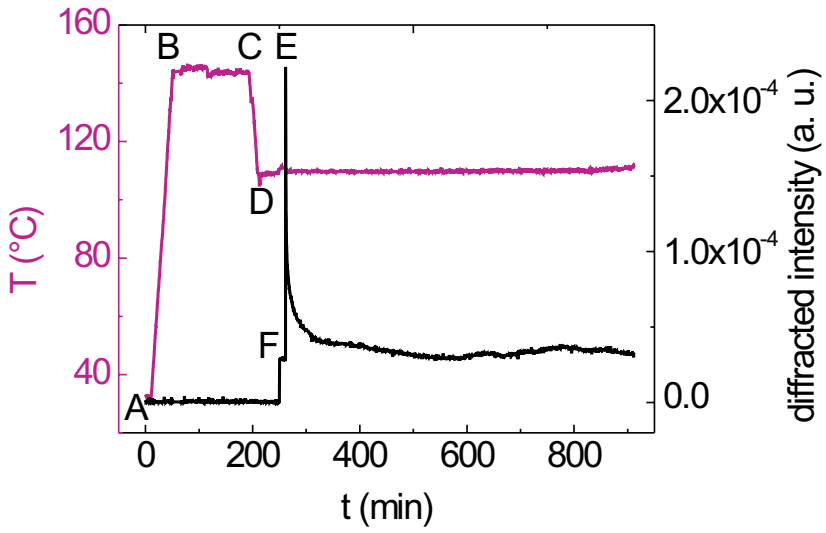

Figure 3.13: Typical data set for dynamic experiments, temperature (black) and intensity (grey) recorded versus time. Explanation of the different process steps: A→B heating, B→C embossing, C→D cooling to temperature chosen for the decay experiment, D→E equilibration step, F: laser shutter opened, E: master lifted from sample and subsequent decay.

A set of measurements is collected with "decay curves" recorded at different temperatures. An example is the set shown in the left-hand graph of Fig. 3.14, which shows the log-log plot of the normalized intensity versus the time. The aim was to check if the normalized data can be superimposed after rescaling of the time scales for the single "decay curves". By rescaling the time scales for the different "decay curves" the acceleration or slowing down of processes

for higher or lower temperatures is considered, respectively. The rescaling on the linear time scale can be also expressed by shifting on the logarithmic time scale. The logarithmic shifts will further be referred to as shift factors. If the rescaling or shifting in respect to one reference ”decay curve” works the result is one master curve consistent with several ”decay curves”. The log-log master plot is presented in the right-graph of Fig. 3.14. This would prove the validity of time-temperature superposition [WLF55] (Sec. 4.3) for the investigated system. The resulting master plot stretches over several orders of magnitude on the time scale.

The accompanying shift factors determined for the different temperature-curves of one

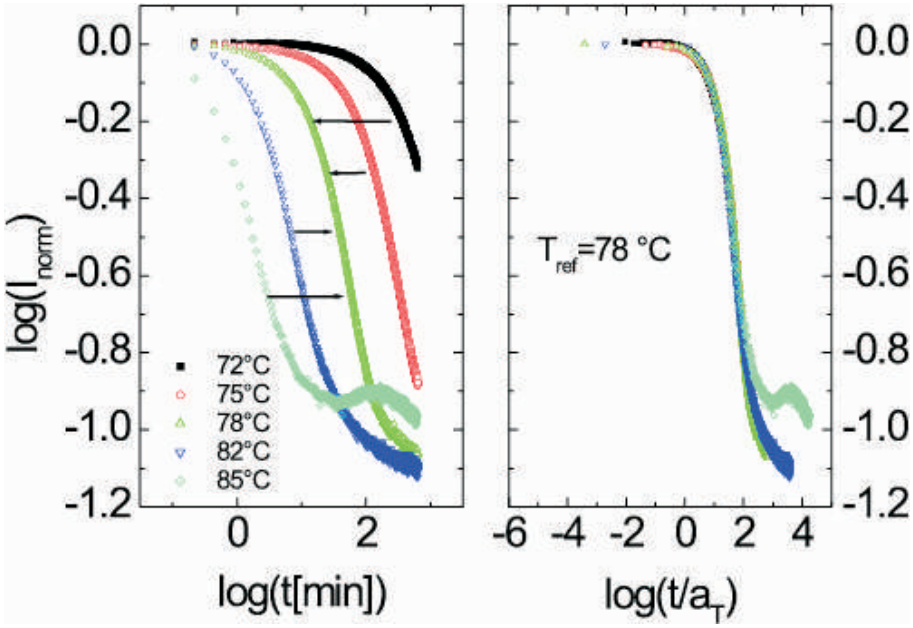

Figure 3.14: The left-hand side log-log graph presents a set of ”decay curves” measured at different temperatures close to $T_{\mathrm{dec},0}$. The data is normalized to the intensity right after lifting the master of the polymer surface. The ”decay curves” of the graph on the right-hand side are shifted on the logarithmic time scale to check if mastering in respect to a single reference temperature works. The shifted ”decay curves” for PS with M_{w}=3.47 kg/mol show that a master curve can be produced.

set of measurements can be analyzed. The shift factors can be analyzed using the free volume based theory of William, Landel and Ferry [WLF55], which extracts information about the free volume and expansion coefficients (see 4.3). The Arrhenius analysis [Büc55] determines activation energies for structural changes (see 4.4). Analyzing the shift factors according to Angell [BA92], [BNAP93] gives an impression about the fragility of a polymer (see 4.5). The theory for the connection between the shift factors and the mentioned values is stated in more detail in chapter 4.

4. THEORETICAL BACKGROUND

In this chapter the theory is presented. The model of surface waves is the basis of describing the decay of sinusoidal gratings driven by surface tension. The time-temperature superposition principle is explained, making use of the models for viscoelastic materials. The different relaxation processes, which are connected to specific activation energies, are treated in this section. The spectrum of relaxations determines the polymer's characteristic viscoelastic properties. The most drastic changes in polymer properties occur at T_{g}. The concept of the temperature dependence of the activation energy above T_{g}, known as fragility, is discussed. Polymeric glass formers can be divided into two categories "strong" and "fragile" according to the temperature dependence of the activation energy above T_{g}. The division into "strong" and "fragile" materials can be done analyzing the shift factors and will be described in detail in a section of this chapter.
The last subsection describes how information about free volume and expansion coefficients can be extracted from the shift factors using the free volume theory.

4.1 Surface Waves

All the experiments described in this work deal with temperature induced decay of polymer surface gratings close to T_{g}.
The two ways the polymer flow will be probed in this work are:

1) The temperature induced flow at a constant heating rate detected with increasing temperature $\rightarrow T_{\mathrm{dec},0}$ measurements, as described in Sec. 3.2.1.
2) The flow at a constant temperature detected with time $\rightarrow$ decay measurements to determine $log(a_{\mathrm{T}})$, as described in Sec. 3.2.2.

Using the model of surface waves [HPP91], the amplitude changes of a sinusoidal grating in a liquid-like state can also be described mathematically. The equations of hydrodynamics can be used as a starting point. The surface waves are eigenfunctions of the Navier–Stokes equation using the assumption that the surface tension is constant. They describe a surface modulation, or displacement, u($\vec{r}$, t) as a function of space and time and have a characteristic in-plane periodicity with a wave vector $\vec{q} = \frac{2\pi}{\lambda}\,\vec{e}_{\mathrm{inplane}}$. In the case, that the eigenvalues for the eigenfunctions are independent, the eigenfunctions can be factorized into a space- and time-dependent factor: $u(\vec{r},t) = A(\vec{r})\,\theta(t))$. Any distortion of the surface can be described by a sum of surface waves $u_{\vec{q}}(\vec{r},t)$ with $\vec{q}$ being the wave vector. Capillary waves are thermally excited surface waves [Ste98], [FBL$^+$00]. A surplus energy at a surface or interface causes a height modulation and this modulation decreases exponentially with depth. The amplitudes of capillary surface waves are usually small. The exponential decay of the modulation in the polymer normal to the surface is illustrated in Fig. 4.1.

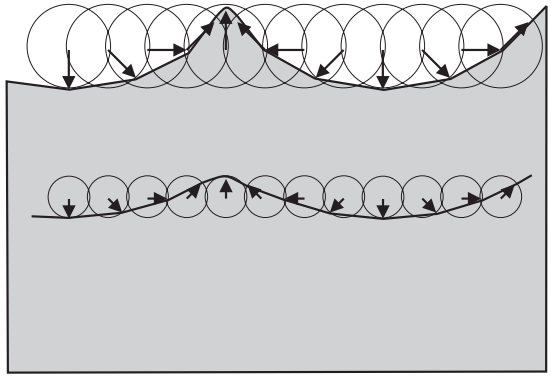

Figure 4.1: Sketch of a capillary surface wave developing at a polymer surface because of an energy surplus. The amplitude of the modulation decreases exponentially in the polymer with distance from the surface. This is mimicked with the second, bottom wave.

Firstly, the space-dependent part $A(\vec{r})$ of the surface wave solutions will be discussed: The coordinates are independent and the function $A(\vec{r}) = A((x,y,z))$ can be factorized, $A((x,y,z)) = A(x)A(y)A(z)$. The in-plane periodicity can be expressed as a cosine function in one of the in-plane directions (x or y), for example the x-direction, $A(x) = A_{x_0}\,cos(\frac{2\pi\,x}{\lambda})$. $A(y)$ is constant, $A(y) = A_{y_0}$. The contribution in the z-direction expresses the exponential decay in the polymer

with distance from the surface at z=0, $A(z) = A_{z_0} exp(-\frac{2\pi z}{\lambda})$

The depth of the modulation in the polymer depends on the amplitude and the grating constant. The amplitude determines the amount of surface modulation, the grating constant how quickly the modulation diminishes in the polymer film. An illustration of the penetration depth of the modulation in the bulk polymer is shown in Fig. 4.2. Three different gratings with the same amplitude but different grating constants in the ratio 100:10:1 are compared.

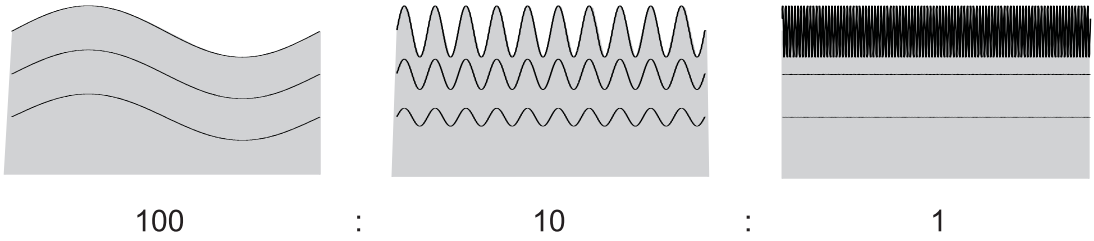

Figure 4.2: The illustration shows how the modulation of the surface grating proceeds into the polymer film. In the illustration the horizontal scale is compressed and the amplitudes seem exaggerated. The amplitude of the three gratings is the same only the grating constants have a ratio of 100:10:1 as indicated below the sketches. The almost unchanged grating with a large grating constant is modulated deeply into the film while at small grating constants the modulation is much shallower.

Defining the probing depth ζ as the depth at which the amplitude is reduced to the $\frac{1}{e}$th part of the surface amplitude, the exponential relation can be expressed as in equation (4.1):

$$\begin{aligned} A(\vec{r}) = A(x,y,z) &= A(x,y,z=0)\, exp(-\frac{2\pi z}{\lambda}) \\ &= A_0\, cos(\zeta\, x)\, exp(-\frac{z}{\zeta}) \end{aligned} \tag{4.1}$$

In equation (4.1) A(x,y,z) is the surface modulation at the position (x,y,z) with the $A_0 = A_{x_0} A_{y_0} A_{z_0}$ and λ is the grating constant. This shows, that in theory the surface sensitivity of the detection technique using polymer gratings as a surface viscoelasticity sensor increases when the grating constant is reduced.

The time and temperature dependent characteristics of the modulation are expressed by the time-dependent part θ(t). The decay of surface waves in a polymer depends on the flow behavior of the polymer. The change of the amplitude with time is detected at a constant heating rate and at a constant temperature. The amplitude decreases at temperatures above T_{g}. This is

sketched in Fig. 4.3. The additional lines indicate the exponential decay of the modulation into the polymer film.

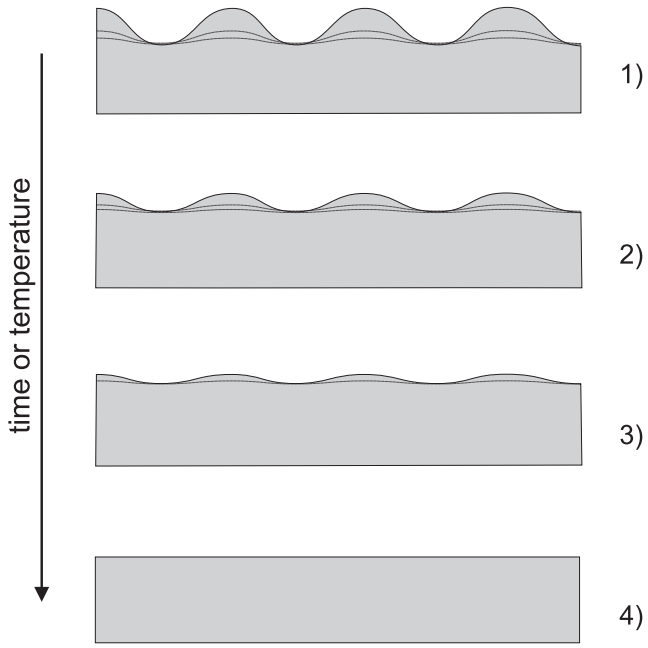

Figure 4.3: Schematic illustration of the either temperature induced decay at a constant heating rate or time induced decay at a constant temperature. 1) Original polymer grating, 2) and 3) decay with time or increasing temperature and 4) the final erasure of the grating after a long time or at high temperatures. The penetration of the modulation in the polymer film is indicated by the additional sinusoidal lines.

A mathematical description of the macroscopic flow behavior of a polymer above T_{g} was done by Hamdorf *et al.* [HJ00] describing the flow of a viscous fluid and supplying the viscosity with a memory function.

The assumptions made in the mathematical treatment are:

The calculations lead to an expression for the viscosity, which can be described in terms of the

- incompressible, isotropic medium
- sinusoidal surface gratings with small aspect ratios to avoid non linear flow dynamics
- linear rheological response (linear stress-strain relation)

grating amplitude and it's first time derivative.

$$\eta(T) = \frac{\pi\gamma}{2\lambda} \frac{u(x,y,z,t)}{\frac{du(x,y,z,t)}{dt}} = \frac{\pi\gamma}{2\lambda} \frac{\theta(t)}{\frac{d\theta(t)}{dt}} \tag{4.2}$$

Another way to describe the same process is to consider the two dominant forces competing at the surface. The surface tension and the viscous drag.
The surface tension as a function of temperature in °C was investigated by Wu *et al.* [Wu70]. The following equations 4.4 contain the temperature dependence of the surface tension γ in 10^{-3}N/m for PMMA and PS.

$$\gamma_{\mathrm{PMMA}} = 41.1 - 0.076(T - 20) \tag{4.3}$$

$$\gamma_{\mathrm{PS}} = 40.7 - 0.072(T - 20) \tag{4.4}$$

The Laplace pressure caused by the surface tension is proportional to the curvature of the surface. The state of minimal surface tension is the state of zero curvature. Thus, the surface tension causes a smoothing of the surface corrugation.
The viscous drag can be considered the resistance to shape changes. Below T_{g} the viscosity of a polymer is very large ($> 10^{13}$ Pa s) and the surface tension is negligible in comparison to the viscous drag. However, the viscosity decreases by many orders of magnitude when the temperature exceeds T_{g}. The decrease is caused by a release of main chain motions from the frozen state below T_{g} as described in Sec. 4.4.
As soon as the viscosity drops, the surface tension can drive the energetically preferred reduction of the surface corrugation (curvature) and the grating amplitude decreases.

The molecular dynamics, which cause the changes in properties such as the viscosity, can be described by theoretical models. Even though no particular model has been definitely proved yet, the compatibility of many models with experimental data has been shown. Theoretical concepts for polymer dynamics of single-chain polymers will be described in the next section.

4.2 Theoretical Models for Polymer Dynamics

The dynamics of the polymer chains can be considered diffusive processes. The self-diffusion can be quantified by determining the mean-square displacement of the center of mass. It is proportional to the observation time t and can be expressed as:

$$\left\langle \left(s\left(t\right) - s\left(0\right)\right)^2 \right\rangle = 2nDt \tag{4.5}$$

In equation (4.5) $s(t)$ is the position at time t, n is the dimensionality of the system, D the diffusion constant, and t the observation time. If $s(t)$ is replaced by $R_{\mathrm{g}}(t)$ the equation describes the diffusion of the entire polymer chain.

At shorter observation times motions on shorter length scales occur. Frictional forces counteract the driving forces for diffusion. Friction occurs either between monomeric units and the surrounding solvent molecules in solution or amongst monomeric units in the melt. The *Einstein relation* (4.6) relates the diffusion coefficient, and the friction coefficient ξ.

$$D = \frac{k_{\mathrm{B}}T}{\xi} \tag{4.6}$$

In the Einstein equation k_{B} is the Boltzmann constant, T the temperature and ξ the friction coefficient.

One model describing this polymer motion and the viscoelastic properties of a polymer was suggested by Rouse - the bead spring model [Rou53]. It is a model to describe single chain motions using a mean-field approach and assuming the validity of Gaussian statistics (orientation along the chain follows a random walk) for the polymer chain.

4.2.1 Bead-Spring Model

Rouse [Rou53] developed the bead-spring model, which describes the viscoelastic properties of a polymer in solution or in a melt of non-interacting chains. The polymer chain is divided into subsections, which are large enough to show rubber like elasticity (springy behavior as small elongations). The subsections are roughly spherical and can be modeled as beads. If the bead, *i.e.* the subsection, performs small motions, it experiences a drag with respect to the remainder of the melt. It can be expressed by the friction coefficient. The whole polymer

chain can then be modeled as a series of springs, which represent the Gaussian entropy, and rigid beads, which express the friction. A graphic illustration of the subdivision of a polymer chain into springs and beads is Fig. 4.4.

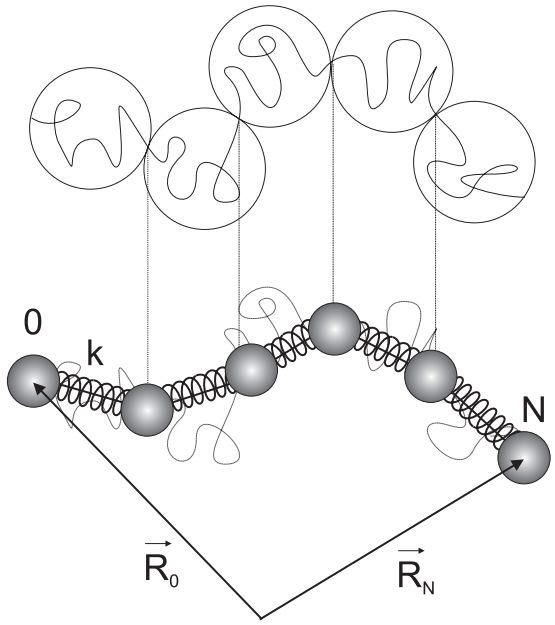

Figure 4.4: The bead spring model divides a polymer chain in elastic and resistive parts. The elastic parts are expressed by springs (spring constant k), the resistive parts by beads (n=0 to N). If the chain follows a random walk the average end-to-end distance of the chain $< (R_N - R_0)^2 >= Nb^2$, where b is the effective bond length.(see **??**)

The Rouse theory [Rou53] is based on the change of free energy associated with the decrease of entropy and the energy dissipation is calculated from sinusoidally oscillating deformations. The forces acting on the beads are friction, elasticity along the chain and stochastic forces (noise and impact of adjacent beads). The chains perform harmonic oscillations with different modes (similar to phonons in crystalline solids). In polymers these modes are damped.

The assumptions of the model are:

- the polymer chain follows Gaussian statistics
- exluded volume effects are negligible (chains can penetrate each other)
- hydrodynamic interactions are negligible

The mean-square displacement of the polymer chain shows distinct power laws in dependence on the observation time. Power law dependencies are often encountered in condensed matter physics and the power can be extracted from log-log plots. The slope of a straight line in a log-log plot is the power of the function. Three regimes with different power law dependencies can be distinguished in the Rouse model:

1) In the first region for short times, fast short ranged isotropic segmental motions occur. The beads do not experience the interconnectivity and perform pure Brownian motion. The Brownian behavior is reflected in the linear time dependence. In this regime the slope of the log-log plot of the mean-square displacement versus time is one.
2) The second region extends between the segmental relaxation time τ_{seg} and the Rouse time τ_{R}. The beads are affected by their neighbors and the Gaussian chain performs many-body oscillations. The power in this region is $\frac{1}{2}$.
3) For times longer than the Rouse time τ_{R} the entire chain performs the diffusive process and not only segments of the chain as described in 1). The Brownian motion of the entire chain is reflected in the t^1 dependence of the mean-square displacement.

Figure 4.5 illustrates the length scales of motion and Fig. 4.6 shows the respective power laws presented in a log-log plot.

The relaxation time τ_R can be extracted from the mathematical treatment of the Rouse model as a many-body oscillator. Here, just a sketch of the deduction should be presented, a more detailed description of the mathematical treatment of this problem can be found in [Doi96]. Graph 4.4 already introduced most of the variables used to describe the polymer. The starting point is the *Langevin equation* (4.7)

$$\frac{d}{dt}(\vec{R}_n) = \frac{1}{\xi}\frac{\partial U}{\partial \vec{R}_n} + g(t) \tag{4.7}$$

with $\vec{R}$ the displacement, ξ the friction coefficient for one bead, $g(t)$ is a probability function with $< g(t) >$=0. The potential U is the potential for the harmonic many-body oscillator (4.8):

$$U = \frac{1}{2}k\sum_{n=1}^{N}(\vec{R}_n - \vec{R}_{n-1})^2 \tag{4.8}$$

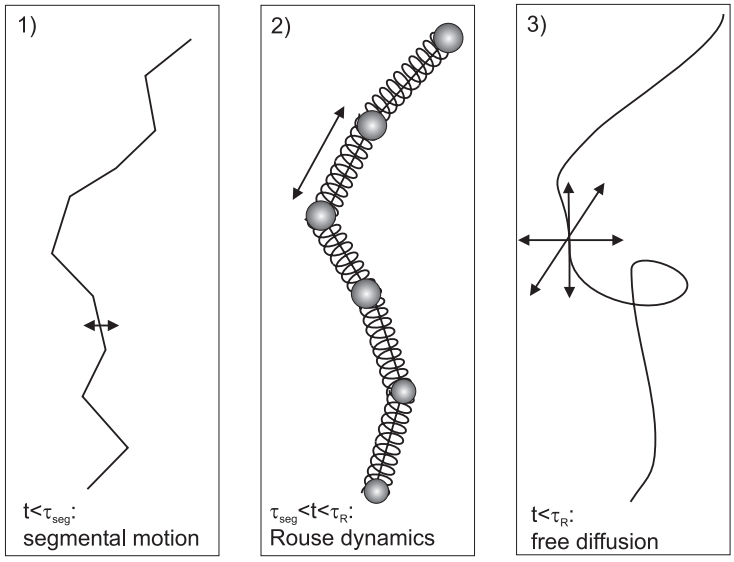

Figure 4.5: Illustration of the dynamic modes in the Rouse model. The motions of chain segments or of the entire chain lead to different power laws.

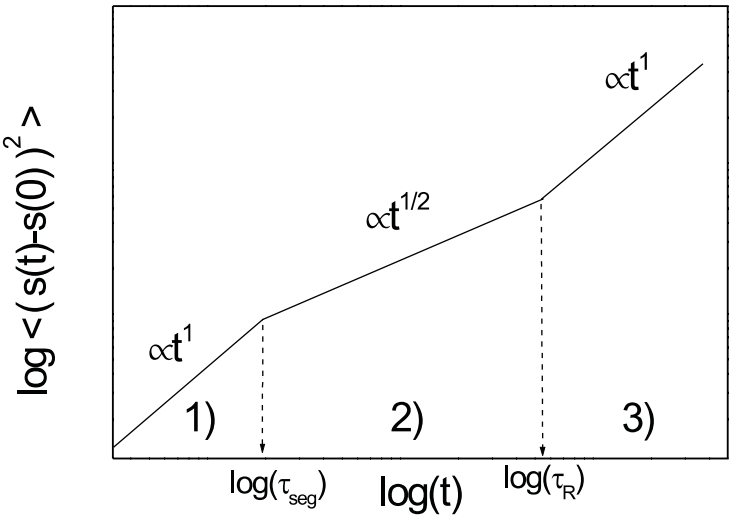

Figure 4.6: Log-log presentation of the mean-square displacement versus time. The graph shows the power law dependencies for the different time regions. The slope in the log-log plot is equal to the power.

---

where k is the spring constant, $\vec{R}_n$ is the position vector of the nth bead, and N is the number of beads. The equations of motion can be deduced, the variable n can be chosen to be continuous (i.e. $\vec{R}_n(t) \rightarrow \vec{R}(n,t)$) and the boundary conditions applied ($\frac{\partial \vec{R}(n,t)}{\partial n} = 0$ at n=0 and n=N). Introducing normalized coordinates $\vec{X}_p$ the equation of motion for a harmonic oscillator can be decomposed into p independent modes.

$$\vec{X}_p(t) = \frac{1}{N}\int_0^N dn\, cos(\frac{\pi p n}{N})\vec{R}(n,t) \tag{4.9}$$

The equation of motion with the new coordinates is the following:

$$\frac{d}{dt}(\vec{X}_p) = -\frac{k_p}{\xi_p}\vec{X}_p + g_p(t) \tag{4.10}$$

The variables in this equation are the friction coefficients $\xi_0 = N\xi$, $\xi_{p>0} = 2N\xi$ and $k_p = \frac{2p^2\pi^2 k}{N}$. The expression for the spring constant of a Gaussian coil at a certain temperature is $k = \frac{3k_BT}{b^2}$, where b is the effective bond lenth. Then the relaxation times τ_p can be expressed as:

$$\tau_p = \frac{\xi_p}{k_p} = \frac{\xi N^2 b^2}{3\pi^2 k_B T p^2} = \frac{\tau_1}{p^2} \tag{4.11}$$

The relaxation time τ_R is the free diffusion limit, at which the whole chain moves. This corresponds to the principal mode p=1 and thus

$$\tau_R = \frac{\xi N^2 b^2}{3\pi^2 k_B T} \tag{4.12}$$

Experiments showed that the Rouse model is suitable to describe polymers in solution in case there are no hydrodynamic interactions and also for polymer melts with molecular weights below the entanglement molecular weight ($M < M_e$).

The Zimm model [Zim56] is also considering hydrodynamic interactions. The theory considers the force on each bead as the sum of hydrodynamic drag forces, forces associated with Brownian motion and Hookean forces (springs) exerted by the neighboring subsections.

An extension of the Rouse model, which is valid for long chains with $M > M_e$, was suggested by de Gennes [dG81] – the reptation model. The reptation model considers interactions between the chains and the effect of entanglements.

4.2.2 Reptation Model

The reptation model (from the Latin word ”reptare” to creep), which was suggested by de Gennes, is also a concept for single chains. For long polymer chains the Rouse model fails

since the assumption of negligible excluded volume effects does not hold anymore. Long surrounding polymer chains constrain the polymer motion. De Gennes suggested in the reptation model to consider the constraints to be a tube formed by the surrounding chains. In this tube the polymer can perform restricted motions. For chains with $M > M_{\mathrm{e}}$ two additional regimes (see 4) and 5)) to the Rouse regime are necessary, which consider the entanglements. The 5 regimes for the dependence of the mean-square displacement on the time are:

1) At times smaller than the characteristic time for segmental relaxation the motion of the beads is isotropic and no interconnectivity experienced as in the Rouse model. The time dependence is linear.
2) The unrestricted Rouse regime, in which the chain performs many-body oscillations, only extends to the characteristic time for entanglements τ_{e}. The power law is $\propto t^{\frac{1}{2}}$, as stated before.
4) At times longer than τ_{e} and shorter than τ_{R} the oscillating bead-spring chain starts to feel the restricting effect of the surrounding chains. The chain performs anisotropic Rouse-like oscillations in the tube, which is formed by entanglements. In this region the power of the mean-square distance is further reduced to $\frac{1}{4}$.
5) In the time regime between τ_{R} and the characteristic time for diffusion, τ_{d}, the polymer performs curvilinear motions along its contour inside the tube. The chain creeps inside the restricting tube like a reptile. The time dependence in this regime is $\propto t^{\frac{1}{2}}$.
3) The last regime for times longer than τ_{d} is very similar to the regime 3) of the Rouse model. The entire tube reorients and at very long times it tumbles isotropically. This is the free diffusion regime of the entire chain.

The five regimes are illustrated in Fig. 4.7 and in Fig. 4.8 the log-log plot of the mean-square distance is plotted versus time to show the power law dependencies of the corresponding regimes.

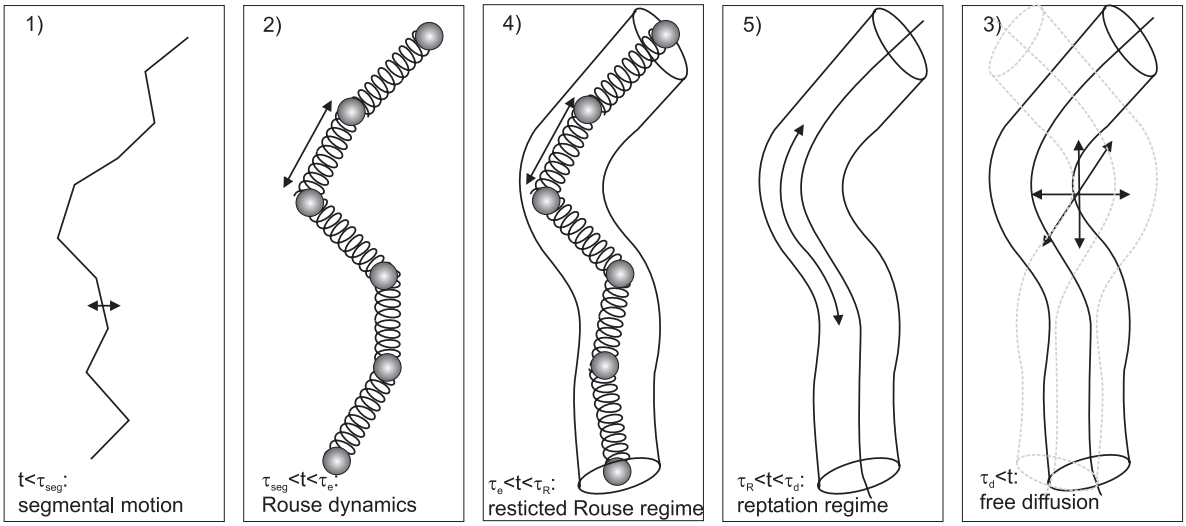

Figure 4.7: Illustration of the dynamic modes in de Gennes reptation model. The motions of chain segments or of the entire chain lead to different power laws, two additional regions appear in the reptation model in comparison to the Rouse model. These regions (4) and 5)) take entanglements into account, which are present in longer polymer chains.

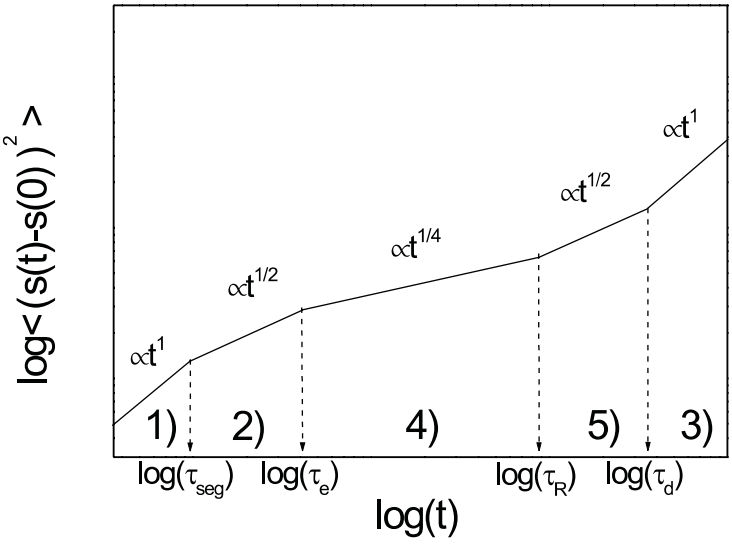

Figure 4.8: Log-log presentation of the mean-square displacement versus time. The graph shows the power law dependencies for the five different time regions of the reptation model. The power of the temperature dependencies are reflected in the slopes of the log-log plot.

The plateau in region 4) appears only if the chain length of the polymer is sufficient for entanglement. The minimum chain length for the appearance of the plateau from theoretical treatments is M_e. It varies with the type of polymer. Experiments investigating the appearance of a rubber plateau in dependence on the molecular weight revealed a critical molecular weight of $M_\mathrm{c} = 2M_\mathrm{e}$ [LM96].

The size of the restricting tube depends on the shape of the polymer. Polymer with side groups need more space thus the tube diameter is larger. The tube diameter in a melt is usually few nanometers and the distance between two entanglements, a, is approximately 150-200 monomer units.

The mean squared end-to-end distance of the polymer, which is Nb^2 in the Rouse model, can be expressed in the reptation model by the number of entanglements Z and the distance between them a.

$$< (R_N - R_0)^2 >= Za^2 = Nb^2 \tag{4.13}$$

Similar to the relaxation time τ_R the relaxation time for the entire entangled polymer, sometimes referred to as 'reptation time' τ_d can be calculated.

$$\tau_d = \frac{\xi N^3 b^4}{\pi^2 k_B T a^2} = 3Z\tau_R \tag{4.14}$$

The bead spring model is the starting point for the time-temperature superposition principle, assuming that the value mainly influenced by the temperature is the friction coefficient. The time-temperature superposition principle will be treated in the next subsection, Sec. 4.3.

4.3 Time-Temperature Superposition

The time-temperature superposition principle was originally found empirically. Starting from the bead-spring model [Rou53] for polymer melts of low molecular weight, viscoelastic functions have similar dependencies. The shear modulus G is an example of a viscoelastic function. Neglecting hydrodynamic interaction, the shear modulus in respect to time is:

$$G(t) = n_\rho k_B T \sum_{p=1}^{N} exp(-\frac{2t}{\tau_p}) = \frac{\rho RT}{M} \sum_{p=1}^{N} exp(-\frac{2tp^2}{\tau_R}) \tag{4.15}$$

In these equations $n_\rho = \frac{\rho N_\mathrm{A}}{M}$ is number of polymer molecules per unit volume, ρ the density, k_B the Boltzmann constant ($k_B = R/N_\mathrm{A} = \frac{8.315 J/molK}{6.02210^{23}\frac{1}{mol}} = 1.3810^{-23} J/K$, R is the ideal gas constant and N_A the Avogadro number), T the temperature, M the molecular weight, and τ_p the relaxation time for the pth mode (also see 4.2, 4.11). The shear modulus is a sum of exponential relaxation functions $exp(-\frac{t}{\tau_p})$. The integration of the shear modulus over the time gives the viscosity.

$$\eta = \int_0^\infty dt\, G(t) = \frac{n_\rho \xi b^2 N^2}{36} \tag{4.16}$$

where η is the long-time limit viscosity and b^2 the mean-square end-to-end distance per monomer unit. One can rewrite equation (4.16) using $n_\rho N = n_\rho \frac{M}{M_0} = \frac{\rho N_A}{M_0}$, so that the molecular weight dependence of the viscosity can be determined: $\eta \propto N \propto M$.

The relaxation times τ_p can also be expressed in terms of the viscosity.

$$\tau_p = \frac{b^2 N^2 \xi_p}{3\pi^2 p^2 k_B T} = \frac{12\eta_0}{\pi n_\rho k_B T} \frac{1}{p^2} \tag{4.17}$$

τ_p is the relaxation time of the pth mode. The relaxation time for the primary mode p=1 is τ_1.

$$\tau_1 = \frac{b^2 N^2 \xi}{3\pi^2 k_B T} = \frac{12\eta_0}{\pi n_\rho k_B T} \tag{4.18}$$

All contributions to G should be proportional to $n_\rho T \;\propto\; \rho T$ and all relaxation times should have the same temperature dependence.

Thus, the relaxation at a temperature T can be expressed in terms of a relaxation at a reference temperature T_ref and a rescaling factor. The rescaling factor for the time scale, a_T, is the ratio of the relaxation times corresponding to the temperatures T and T_ref.

$$a_\mathrm{T} = \frac{[\tau_p]_T}{[\tau_p]_{T_\mathrm{ref}}} = \frac{[\frac{b^2\xi}{T}]_T}{[\frac{b^2\xi}{T}]_{T_\mathrm{ref}}} = \frac{[b^2\xi]_T T_\mathrm{ref}}{[b^2\xi]_{T_\mathrm{ref}} T} \tag{4.19}$$

The main contribution to a_T does not come from the temperature itself, as one would first assume, but it comes from the friction coefficient. The friction coefficient is the factor, which changes strongly with temperature. The mean-squared end-to-end distance per monomer unit, b^2, changes only slightly with temperature.

The shear modulus or any other viscoelastic function changes proportional to $\frac{\rho T}{\rho_\mathrm{ref} T_\mathrm{ref}}$ changing

$$T \longrightarrow T_{\mathrm{ref}}$$
$$\omega \longrightarrow a_{\mathrm{T}}\omega$$
$$t \longrightarrow \frac{t}{a_{\mathrm{T}}}$$
$$G(t,T) \longrightarrow G(\frac{t}{a_{\mathrm{T}}}, T_{\mathrm{ref}})\ \frac{\rho T}{\rho_{\mathrm{ref}} T_{\mathrm{ref}}}$$

Table 4.1: Time-temperature superposition rules

the reference temperature from T to T_{ref}. Thus, the rescaling factor for the visco-elastic functions, with reference to a temperature T_{ref}, is the ratio of the temperature-density products at T and T_{ref}. The changes in density are usually small (very small expansion coefficients 3 to $5{\cdot}10^{-4}\frac{1}{K}$ for PMMA and PS [WSY97]), so the temperature-density ratio might also be approximated by the temperature ratio.
Concluding, the time-temperature superposition can be expressed as a transformation with the rules listed in table 4.1.

The rescaling factors a_{T} can also be expressed in terms of viscosities in the case of un-crosslinked, low molecular weight polymers with $M < M_{\mathrm{C}} \approx 2M_{\mathrm{e}}$ as

$$a_{\mathrm{T}} = \frac{[\tau_p]_T}{[\tau_p]_{T_{\mathrm{ref}}}} = \frac{[\eta]_{\mathrm{T}} \frac{\rho T}{\rho_{\mathrm{ref}} T_{\mathrm{ref}}}}{[\eta]_{T_{\mathrm{ref}}}} \tag{4.20}$$

The temperature dependence of rescaling factors a_{T} is determined by the relaxation processes contributing to the relaxation.

The same rescaling factors can be found starting from the reptation model. The expression for the shear modulus in the reptation model is more complicated. The detailed deduction can be found in [Doi96] and under the assumption that $\tau_R << \tau_d$ it results in:

$$G(t) = \frac{3Nb^2\rho RT}{5a^2} \sum_{p=1}^{N} \frac{8}{p^2\pi^2} exp(-\frac{tp^2}{\tau_d}) \tag{4.21}$$

The viscosity results in:

$$\eta = \frac{\pi^2 \rho k_B T}{20Z} \tau_d \tag{4.22}$$

τ_d is proportional to N^3 so the dependence of the viscosity on the molecular weight for long chains is proportional to M^3. Experiments show a slightly higher power [CFG87].

4.4 Relaxation Processes and Activation Energy

The activation energy is the energy necessary to activate certain relaxation processes in polymers. Relaxation processes can happen on a relatively large scale, where large segments of the polymer backbone are involved in the relaxation motion. This type of relaxation is called α-relaxation.

There are also secondary relaxation processes which occur on smaller length scales and need less energy to be activated than the α-relaxation. Secondary relaxation processes are the localized motion of small main chain segments, rotations of whole side groups about their bond link (β-relaxation) or very localized rotations within the side group (γ-relaxation). A sketch of the segments involved in each relaxation mode is presented in Fig. 4.9.

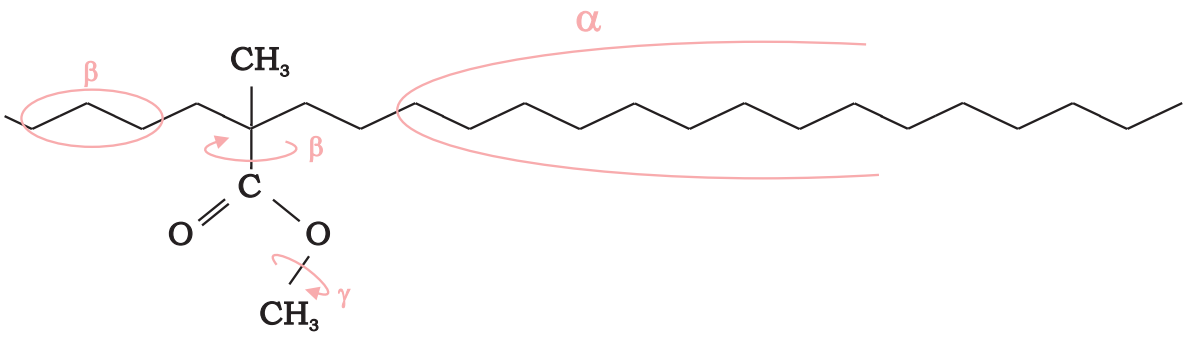

Figure 4.9: Schematic illustration of molecular relaxation modes in the case of PMMA: α-relaxation - large main chain segments, β-relaxation - small main chain segments or rotation of entire side groups (rotation of -$COOCH_3$ group), γ-relaxation - rotations within the side groups (rotation of -CH_3).

The temperature dependent behavior of a polymer depends on the different relaxation modes activated. Below the Kauzmann temperature the system is trapped in a deep energy minimum and the probability to access other minima by thermal activation is very small. The α-relaxation becomes frozen and only very localized molecular motions are activated. The re-

laxation of the system would need infinitively long. The amorphous solid is in the glass state. Above the Kauzmann temperature T_{K} and below T_{g} localized relaxation processes with low activation energies occur. The relaxation behavior can be described as the probability to overcome energy barriers on a local energy landscape. A simplified illustration of an energy landscape below T_{g} is given in Fig. 4.10. There is not only one single mechanically stable minimum of potential energy accessible but a large number of the order $exp\,(N)$ with N being the number of particles in the system. The motion of the entire chain is still frozen, but secondary relaxations like rotation of the side chains or subgroups of the chains are possible. The activation energy for the β or γ relaxations are much smaller than the main chain relaxation and they already take place at much lower temperatures. The thermally accessible potential energy landscape shows only small variations.

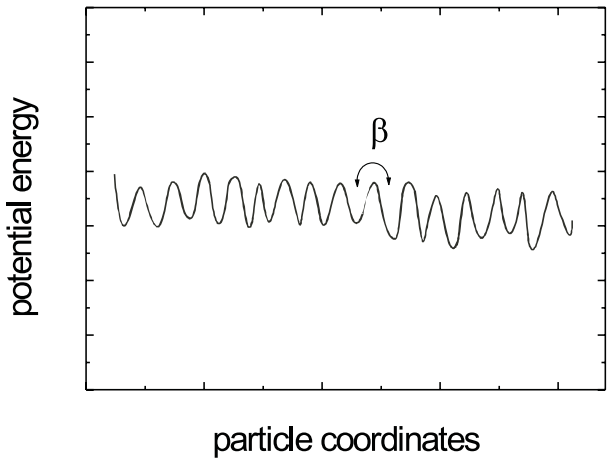

Figure 4.10: Energy landscape for the glassy state below T_{g} with its Arrhenius-like relaxation time or viscosity behavior. A side chain configuration change is possible even at low temperatures. A β-relaxation correlated with a ”hopping” from one energy minimum over a low energy barrier to another by performing small conformational changes is indicated by the double arrow.

Considering the changes in configuration as ”jumps” between adjacent energy minima of the landscape, the structure of the landscape determines the relaxation processes. The potential barriers, which have to be overcome to activate configuration changes, are finite and depend mainly on the strength of the bonding and the steric interactions. Strong bonds and steric hindrance increase the potential barriers. The probability of the system to overcome the potential

barrier and relax through different configurations is dependent on the system's energy. The thermal energy has to be greater than the potential barrier. The temperature dependent relaxation time τ is often expressed by:

$$\tau = \tau_0 \exp(\frac{\mathrm{E_a}}{\mathrm{RT}}) \tag{4.23}$$

In the case, that only a single relaxation process is activated, the activation energy for this relaxation processes can be extracted from the logarithm of the rescaling factors a_T - the so-called shift factors $\log(a_\mathrm{T})$ - via the relation:

$$\log(\mathrm{a_T}) = \frac{\ln(\mathrm{a_T})}{\ln(10)} = \frac{\mathrm{E_a}}{\ln(10)\mathrm{R}}(\frac{1}{\mathrm{T}} - \frac{1}{\mathrm{T_{ref}}}) \tag{4.24}$$

This relation shows that plotting the log(a_T) values versus the inverse temperature in Kelvin gives a straight line, as in Fig. 4.11. This plot is called Arrhenius plot.

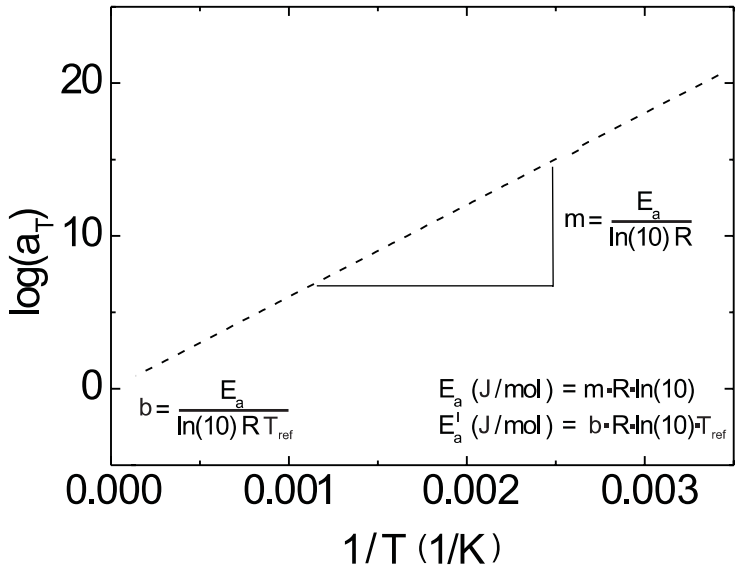

Figure 4.11: The Arrhenius plot is a straight line for Arrhenius-like liquids. The scheme shows how to extract the activation energy E_a from the slope m.

If the reference temperature for the measurements of $\log(a_\mathrm{T})$ is not infinitely large, the activation energy can be extracted from both the slope m and the intercept b of an Arrhenius-plot as equation (4.24) and (4.25) clarify.

$$\begin{aligned} m = & \quad \frac{d(\log(\mathrm{a_T}))}{d(\frac{1}{T})} \; = \; \frac{E_\mathrm{a}}{\ln(10)\mathrm{R}}, \\ b \; = & \quad \frac{E_\mathrm{a}}{\ln(10)\mathrm{RT_{ref}}} \end{aligned} \tag{4.25}$$

The expression for the intercept b does not reflect a dependence of E_a on T_ref but expresses the shifting of the $log(a_\mathrm{T})$ values on the y-scale with the choice of a different T_ref. The activation energy is the same.

Adam and Gibbs [AG65] described the kinetic motion using the concept of "cooperatively re-arranging regions" [GD58a]. The configurational changes can take place in structural units without effecting the surrounding environment. In terms of thermodynamics they described the relaxation time in dependence of the configurational entropy. The activation energy in this picture is proportional to the inverse configurational entropy:

$$\tau = \tau_0 \, \exp(\frac{\mathrm{E_a}}{\mathrm{RT}}) = \tau_0 \, \exp(\frac{\mathrm{B}}{\mathrm{TS_C}}) \tag{4.26}$$

B is a constant and the configurational entropy S_C is related to the number of minima on the potential energy landscape. Below T_g the number of accessible energy minima, the configurational entropy and the activation energy are constant. The entropy can be determined from the heat capacity.

$$S_\mathrm{C} = \int_{T_\mathrm{K}}^{T} \Delta \frac{C_\mathrm{p}}{T'} dT' \tag{4.27}$$

At temperatures above T_g not only β and γ relaxations take place but also the α relaxation of the main chain contributes. The α contribution changes the energy landscape by introducing deep "basins" into the structure as shown in Fig. 4.12.

In this temperature regime the number of accessible minima on the energy surface depends on temperature. Thus, the configurational entropy and the activation energy are not constant but show a temperature dependence. It appears in the Arrhenius plot, Fig. 4.13. The slow α relaxation, which is responsible for the glass transition, introduces a different relaxation behavior.

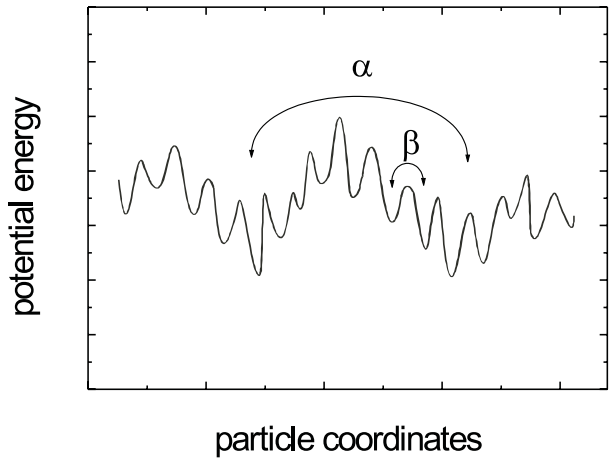

Figure 4.12: Energy landscape for a melt above T_{g}. The two experimentally most relevant relaxation processes: the α and the β relaxation. The activation of large main chain segments (α), requires more energy or higher temperatures than the activation of secondary relaxation processes (β).

The amount of non-Arrhenius-like behavior depends on the material. Some materials show almost no temperature dependence of the activation energy above T_{g} and thus deviate very slightly from Arrhenius behavior. This temperature dependence of the relaxation times can be described by the Arrhenius law. Materials with a more pronounced deviation from Arrhenius behavior, arising from a wide distribution of relaxation times once the α relaxation contributes, cannot be approximated by the Arrhenius law anymore. The activation energy becomes temperature dependent. The resulting temperature dependence of the relaxation times can be described in several ways.

Vogel-Fulcher-Tammann-Hesse (VFTH):

The viscosity or relaxation times can be described by the relation developed by Vogel [Vog21], Tammann, Hesse [TH26], and Fulcher [Ful25]. The so-called VF-, VFT, or VFTH equation (4.28) expresses the curvature by substituting the temperature T in the Arrhenius relation (4.23) by a temperature difference $(T - T_{\mathrm{inf}})$. The temperature T_{inf} is the temperature at which all motions on a larger scale are frozen in. It is very close to the Kauzmann temperature, at which the system has a minimum energy.

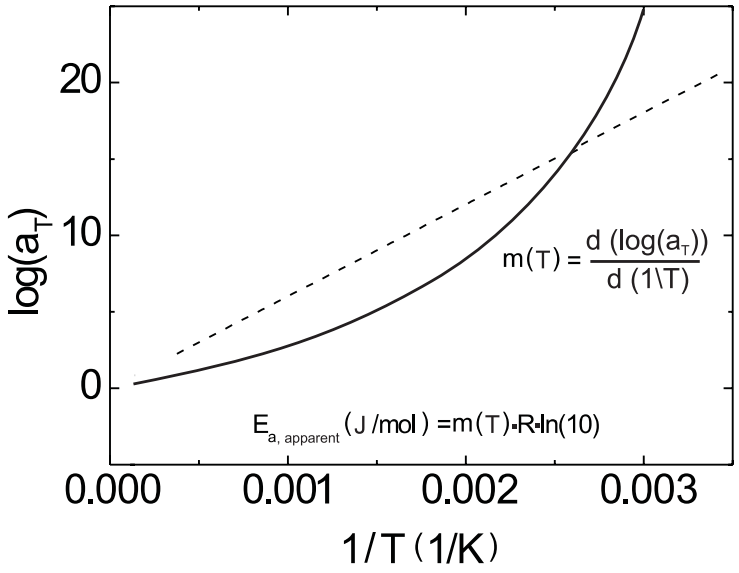

Figure 4.13: The Arrhenius plot above T_{g} is not necessarily a straight line. The additional α relaxation changes the relaxation behavior and the slope m of the Arrhenius plot becomes temperature dependent. Only an apparent activation energy $E_{\mathrm{a,apparent}}$ can be extracted.

$$\tau = \tau_0 \, exp(\frac{B}{T - T_{\mathrm{inf}}}) = \tau_0 \, exp(\frac{D}{(\frac{T}{T_{\mathrm{inf}}} - 1)}) \tag{4.28}$$

The parameter D is a measure for the strength of the material in the strong–fragile classification. Strong materials have a large D value (D(SiO)=100, [Ang88]), for fragile materials the D value is small(O-Terphenyl: D≈5 [Ang88]).

The shift factors then result in:

$$log(a_{\mathrm{T}}) \; = log(\frac{\tau(T)}{\tau(T_{\mathrm{ref}})}) = \frac{B}{\ln(10)} \, (\frac{1}{T - T_{\mathrm{inf}}} - \frac{1}{T_{\mathrm{ref}} - T_{\mathrm{inf}}}) \tag{4.29}$$

Adam–Gibbs (AG):

The same equation evolves from the thermodynamic treatment of Adam and Gibbs (equations (4.26) and (4.27)) assuming a heat capacity $\Delta C_{\mathrm{p}} = \frac{const}{T}$ and considering the temperatures T_{K} and T_{inf} the same:

$$T_{\mathrm{K}} \approx T_{\mathrm{inf}} \tag{4.30}$$

Williams–Landel–Ferry (WLF):

The Williams–Landel–Ferry equation (4.31) [WLF55] is mathematically not different from the VF equation. This dependence of $log(a_{\mathrm{T}})$ on the temperature was initially found empirically by collecting lots of data and trying to match them by shifting on the logarithmic time scale. This is where the name shift factors originates from. The WLF relation is of wide applicability.

$$log(a_{\mathrm{T}}) = \frac{-c_1(T - T_{\mathrm{ref}})}{c_2 + T - T_{\mathrm{ref}}} \tag{4.31}$$

The temperature T_{ref} is the reference temperature with respect to which the data are shifted so that the data curves match and the shift factors can be determined.

The parameters c_1 and c_2 can be expressed in terms of the parameters of equation (4.28) by comparing equation (4.41) and (4.31). With T_{ref}=T_{inf}+c_2 [Kov64], c_1 and c_2 result in:

$$\begin{aligned} c_1(T_{\mathrm{ref}}) &= \frac{B}{\ln(10)} \frac{1}{T_{\mathrm{ref}} - T_{\mathrm{inf}}} \\ c_2(T_{\mathrm{ref}}) &= T_{\mathrm{ref}} - T_{\mathrm{inf}} \end{aligned} \tag{4.32}$$

c_1 can also be expressed in terms of relaxation times:

$$c_1(T_{\mathrm{ref}}) = log(\frac{\tau(T_{\mathrm{ref}})}{\tau_0}) \tag{4.33}$$

Kohlrausch–Williams–Watts (KWW):

A third relation, which describes the relaxation behavior of polymers, is the Kohlrausch–Williams–Watts equation [Koh74], [WW70]. The temporal behavior of a response function to an applied field, stress or deformation is described as a stretched exponential function:

$$\phi(t) = exp[-(\frac{t}{\tau})^{\beta^*}] \tag{4.34}$$

τ is the characteristic relaxation time, with a possibly non-Arrhenius temperature dependence.

The stretch exponent β^* is denoted by a "*" to distinguish it from the β-relaxation. It has a value between 0 and 1. The response function $\phi(t)$ can be expressed by the time dependence of the grating amplitude $\theta(t)$, which is $u(\vec{r},t)$ normalized to the initial value $u(\vec{r},t=0) = A(\vec{r})\theta(0)$ provided that the grating constant remains the same during the decay process (4.35). The amplitude at infinity should be zero, so $\theta(\infty)$ is the square root of the background intensity.

$$\phi(t) = \frac{(u(\vec{r},t) - u(\vec{r},\infty))}{(u(\vec{r},0) - u(\vec{r},\infty))} = \frac{(\theta(t) - \theta(\infty))}{(\theta(0) - \theta(\infty))} \tag{4.35}$$

The connection between temperature dependent relaxation times, entropy, number of accessible states and energy for a fragile system above T_{g} is summarized in Fig. 4.14 taken from [ANM$^+$00].

The scheme taken from [ANM$^+$00] shows the relation between temperature dependent relaxation times, entropy and energy above T_{g}. Starting at high temperatures (point 1 in a), b) and c)) the relaxation times are short (a), the entropy high (b), the polymer's energy higher than the potential energy (c). The polymer diffuses freely and neither feels the barriers nor the traps of the energy landscape. In the vicinity of point 2 (close to the possible melting point of the glass former, indicated by the dashed line in (b)), the system starts to "sense" the energy landscape. The influence of the landscape increases as the temperature approaches T_{g} at point 5. At T_{g} the system gets trapped in a single minimum of the energy landscape with very little excess entropy and the relaxation time increases rapidly beyond the experimental measuring time. The system falls out of equilibrium and is in a non-ergodic (non-equilibrium) state below T_{g}. The excess entropy is very small, the liquid character vanishes and a glass forms. The energy per particle of a mixed Lennard–Jones system, as a function of temperature, is shown in (d) adapted from [SDS98], [DSTR99]. For the normalized temperature $T > 1$ the particles have enough energy to sample the entire energy landscape and diffuse freely. Between $T = 1$ (corresponds to point 2 in (a, b, c) and $T = 0.45$ the activation energy increases upon cooling and the mechanically stable configurations, which can be sampled, become strongly temperature dependent. In the landscape dominated regime below $T = 0.45$ the particles rarely jump. The jump distance is roughly the inter-particle distance. The crossover temperature between the landscape influenced and landscape dominated regime corresponds closely to the temperature T_{C} determined by the

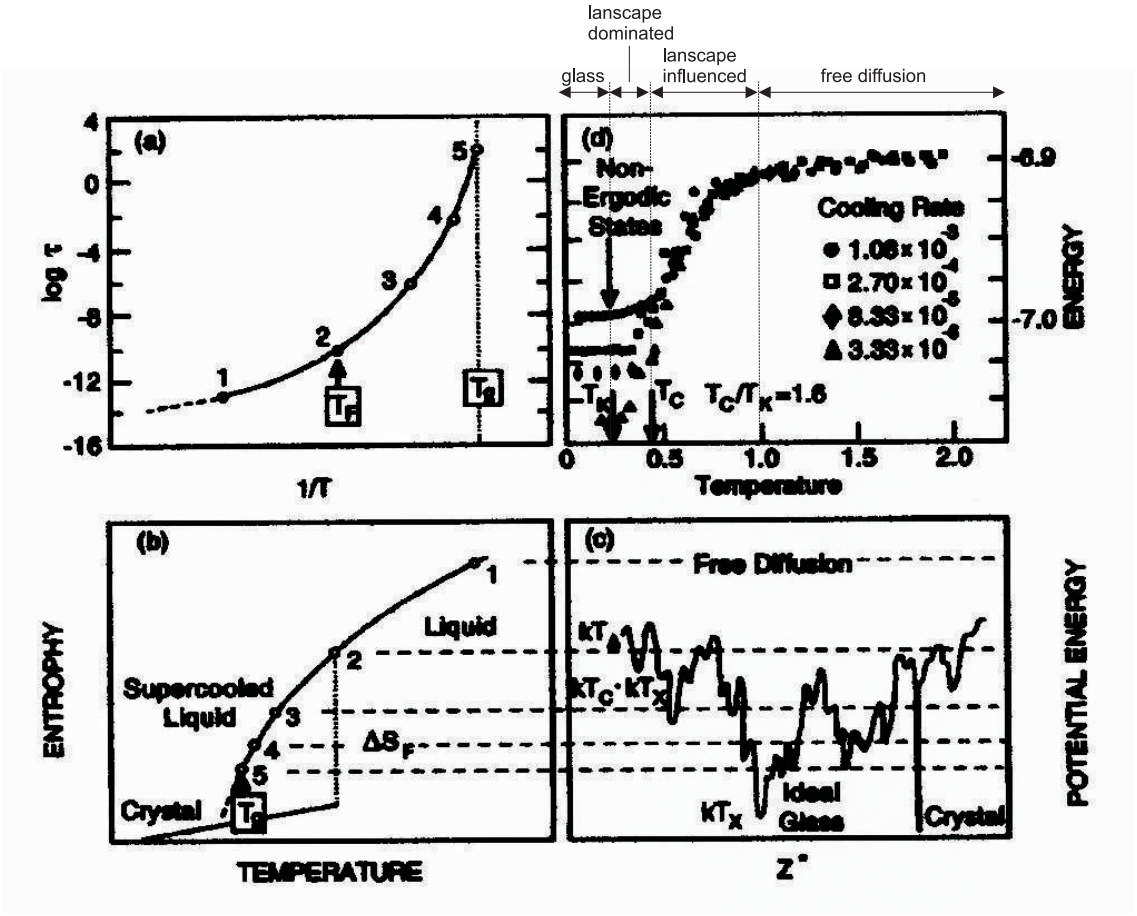

Figure 4.14: The scheme summarizes the relation between relaxation times, excess entropy, potential energy and energy per particle. Following the numbering from point 1 to 5 the relaxation times are diverging (a), the excess entropy is vanishing (b) and the potential energy of the accessible states is decreasing and the system occupies the minima on the energy landscape. (d) quantifies the energy landscape for a mixed Lennard-Jones system according to [SDS98], [DSTR99]

---

mode-coupling theory [SDS98], [KA95]. In the landscape dominated and glassy regime the dependence of the final state on the heating rate indicates the non-ergodic (non-equilibrium) state of the system in this regime. The temperature corresponding to the deepest minimum on the amorphous phase energy landscape is the Kauzmann temperature T_{K}. It characterizes the equilibrium state, which would only be accessible if infinitively small cooling rates could be performed. T_{K} is linearly extrapolated to satisfy the condition $\frac{T_{\mathrm{C}}}{T_{\mathrm{K}}} = 1.6$ according to [NSS$^+$00].

Different theories have developed to describe the property changes close to T_{g}.

The *free volume theory* describes the free volume changes of a glassy system in a simple way with adjustable parameters [CG79], [CT59], [CT61], [CT70]. It is a phenomenological approach and the definition of the free volume is not rigorous.

The *Gibbs-DiMarzio* theory describes the polymer at the glass transition as an ordinary second order transition [GD58a], [GD58b]. This theory assumes, that the configurational entropy of the polymer is zero at T_{g}. The thermodynamical approach requires equilibrium states on both sides of the transition. The equilibrium requirements are expressed in the Ehrenfest theorem (10.1), which is not fulfilled in the case of the glass transition.

A third theory is the *mode coupling theory*. This theory defines a critical temperature at which the structural relaxation diverges. The system freezes but it still keeps its amorphous character, *i.e.* the static properties are still liquid-like [BGS84], [GS95], [GS92]. The mode coupling theory describes the dynamics of glass former successfully for high temperatures, however, fails near T_{g}. The mode coupling theory is valid in the free diffusion regime at temperatures above point 2 in Fig. 4.14.

Theoretical calculation from the Binder group [BBPB00], [VBB02] using the mode coupling theory consider the possibility of the polymer chain escaping from a ”cage” formed by surrounding polymer chains. The escape relates to the α relaxation. They found a dependence of the escape probability on the molecular connectivity of the chains. The activation energy for the relaxation processes at T_{g} (α relaxation) should then be molecular weight dependent.

The concept of *cooperative motion* was first introduced by Adams and Gibbs [AG65]. They proposed that the individual particle motion close to T_{g} is frozen but collective motion of many particles is still possible. In this case, characteristic length scales are comparable to those of the cooperative particles, which are increasing with decreasing temperature. The cooperative motion concept also explains heterogeneities in the dynamics [KDP$^+$97], [DGP$^+$99], [BPBB99].

4.5 Fragility

The degree of non-Arrhenius behavior is called fragility. Liquids or melts are classified into two categories:

1) Liquids or melts with Arrhenius-like or almost Arrhenius-like temperature dependence

$\longrightarrow$ ”strong”

2) Liquids or melts which do not show Arrhenius behavior

$\longrightarrow$ ”fragile”

Different measures of fragility are suggested originating from the methods to describe the non-Arrhenius behavior.
Starting with the VFTH equation (4.28), the fragility F of a polymer can be defined as the the ratio of the Vogel-Fulcher temperature T_{inf} and the glass temperature.

$$F_{\mathrm{VF}} = \frac{T_{\mathrm{inf}}}{T_{\mathrm{g}}} \tag{4.36}$$

Using the parameters from the WLF equation 4.31 and the relation $T_{\mathrm{inf}} = T_{\mathrm{ref}} - c_2 = T_1 - c_2^1$ [Kov64], the fragility can be expressed as:

$$F_{\mathrm{WLF}} = \frac{T_{\mathrm{ref}} - c_2}{T_{\mathrm{g}}} \tag{4.37}$$

In the case of simple liquids the value for T_{inf} is very close to T_{K} resulting from the theromodynamic treatment: $T_{\mathrm{inf}} \approx T_{\mathrm{K}}$ ($0.9 < \frac{T_{\mathrm{inf}}}{T_{\mathrm{K}}} < 1.1$, [Ang98]).
Both values for F_{VF} and F_{WLF} vary between 0 and 1. The categories are:

$$\begin{aligned} F &= 0 \quad \longrightarrow \text{"}strong\text{"} \\ F &= 1 \quad \longrightarrow \text{"}fragile\text{"} \end{aligned}$$

In the case of the KWW equation (4.34) the measure for fragility is the stretch exponent β^*. Liquids with β^*=1 show Arrhenius-like behavior and are therefore strong. If the stretch exponent β^* is smaller than one, the material is fragile. The more β^* deviates from one the more fragile is the material.

A fourth way to measure fragility is to determine the slope of the T_{g} scaled Arrhenius-plot, also called an Angell-plot, at the point $\frac{T_{\mathrm{g}}}{T} = 1$. The rescaled Arrhenius-plot makes it possible to compare different materials above the glass temperature by eye and divide them into strong and fragile liquids or melts. A collection of data taken from [ANM$^+$00] shows a typical Angell-plot with strong and fragile liquids. The slope at T_{g} increases with increasing fragility.

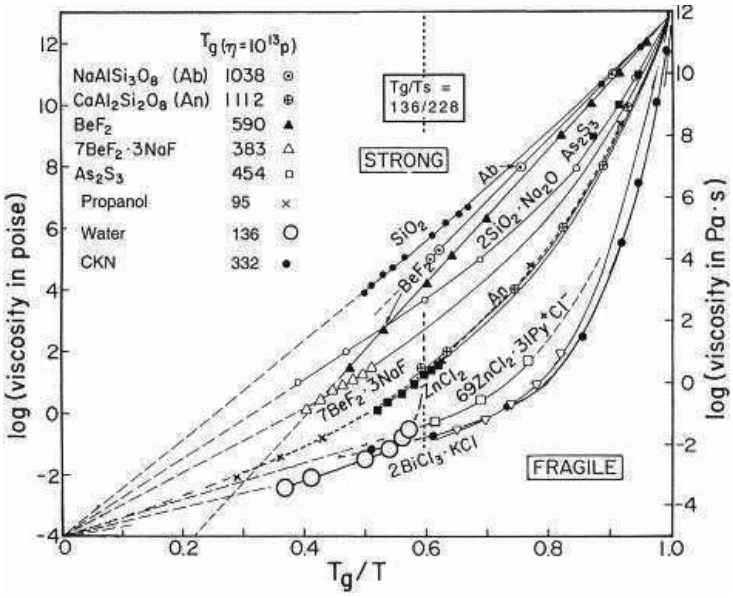

Figure 4.15: The Angell-plot from [ANM+00] shows the strong and fragile data sets. The almost straight lines for the strong liquids or melts like SiO_2 are in contrast with the curved functions of the fragile materials, such as $2BiCl_3 \cdot KCl$. It is visible that the slope at $\frac{T_g}{T} = 1$ increases from strong to fragile liquids.

The fragility depends in the simple case on the energy (bonding) and the volume (steric) interactions. The energy to activate secondary relaxation (fragility) is crucial. The stronger the bonding, the closer the time scales for relaxations, *i.e.* the smaller the fragility. The volume influences the fragility since the larger the activation volume (the volume necessary for an activation of a relaxation) the closer the time scales for the relaxations.
Information about the free volume and expansion coefficients can also extracted from the shift factors, interpreting them by means of the free volume theory [CG79], [CT59], [CT61], [CT70]. The next section covers this topic.

4.6 Free Volume and Expansion Coefficients

Following the free volume theory the values c_1 and c_2 also give information about the free volume and the expansion coefficient. The best way to extract c_1 and c_2 from $log(a_T)$ is to plot $(T - T_{ref})/log\, a_T$ versus $(T - T_{ref})$. The graph should represent a straight line with the slope m = $-\frac{1}{c_1}$ and the intercept b = $-\frac{c_2}{c_1}$ as Fig. 4.16 suggests.

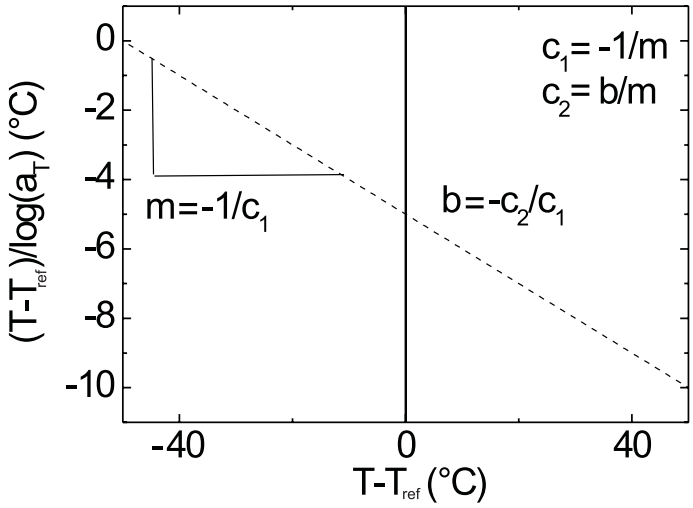

Figure 4.16: Graphical extraction of the WLF parameters c_1 and c_2 from the shift factors log(a_{T}).

The values can be transformed to a reference curve at a different temperature T_{ref1} by the equations:

$$c_2^1 = c_2 + T_{\mathrm{ref1}} - T_{\mathrm{ref}} = T_{\mathrm{ref1}} - (T_{\mathrm{ref}} - c_2) \tag{4.38}$$

$$c_1^1 = \frac{c_1 c_2}{c_2 + (T_{\mathrm{ref1}} - T_{\mathrm{ref}})} \tag{4.39}$$

The quality of the choice of c_2 can be checked by the requirement, that the data should represent a straight line going through the origin. Another way to express the time-temperature superposition is by means of the Vogel-Fulcher temperature T_{inf}.

$$T_{\mathrm{inf}} = T_{\mathrm{ref}} - c_2 = T_{\mathrm{ref1}} - c_2^1 \tag{4.40}$$

Equation 4.31 then results in:

$$log\ a_{\mathrm{T}} = \frac{-c_1(T - T_{\mathrm{ref}})}{(T - T_{\mathrm{inf}})} \tag{4.41}$$

This is also the equation from which the widespread rule of thumb originates, that T_{inf} is 50°C below the glass temperature: $T_{\mathrm{inf}} \approx T_{\mathrm{g}}$ - 50°C. It arises from the fact that c_2 is usually about 50°C using T_{g} as the reference temperature. The rule of thumb can thus be deduced from the

relation: T_{inf} = T_{ref} - c_2.

With the shifting procedure it is possible to get information about a much wider time or frequency range (up to 12 decades) than the one accessible by experiments (maximum 6 decades), which makes the method favored by many researchers even though it is empirical.

The time-temperature superposition principle can also be interpreted in terms of free volume. Reducing the temperature has the consequence that the mobility of the polymer is more and more restricted and the amount of free volume is decreased until it reaches a minimum value at T_{g}. The concept of this interpretation is that the mobility depends on the free volume v_{f}, which is chosen to be the independent variable.
The viscosity also shows an Arrhenius dependence on the free volume, which was found empirically:

$$\eta_0 = \eta_{00}\, exp\,(B\frac{v - v_{\mathrm{f}}}{v_{\mathrm{f}}}) \tag{4.42}$$

In this equation η_{00} and B are empirical constants. The free volume fraction is defined as $f = \frac{v_{\mathrm{f}}}{v}$ ($v \propto \frac{1}{\rho}$ being the reciprocal density). With equation (4.20) and further transformations ([Fer80] and references herein) the time-temperature superposition results in:

$$\log \mathrm{a_T} = \frac{\mathrm{B}}{\ln(10)}(\frac{1}{\mathrm{f}} - \frac{1}{\mathrm{f_{ref}}}) + \log(\frac{\rho_{\mathrm{ref}}\mathrm{T_{ref}}}{\rho\mathrm{T}}) \tag{4.43}$$

which, due to a small expansion coefficient, is mostly used as:

$$\log \mathrm{a_T} = \frac{\mathrm{B}}{\ln(10)}(\frac{1}{\mathrm{f}} - \frac{1}{\mathrm{f_{ref}}}) \tag{4.44}$$

Assuming a linear dependence of the free volume fraction f on the temperature:

$$f = f_{\mathrm{ref}} + \alpha_{\mathrm{f}}(T - T_{\mathrm{ref}}) \tag{4.45}$$

equation (4.44) results in:

$$log\, a_{\mathrm{T}} = \frac{-\frac{B}{ln(10) f_{\mathrm{ref}}}(T - T_{\mathrm{ref}})}{\frac{f_{\mathrm{ref}}}{\alpha_{\mathrm{f}}} + T - T_{\mathrm{ref}}} \tag{4.46}$$

Comparing equation (4.46) with equation (4.31) the parameters c_1 and c_2 can give information about free volume and expansion behavior of the material:

$$c_1 = \frac{B}{\ln(10)\, \mathrm{f_{ref}}} \tag{4.47}$$

$$c_2 = \frac{f_{\mathrm{ref}}}{\alpha_{\mathrm{f}}} \tag{4.48}$$

The free volume fraction and the expansion coefficient can be expressed in terms of c_1 and c_2 and related to the slope and intercept determined from the analysis graphs 4.50.

$$f_0 = \frac{B}{\ln(10) c_1} = -\frac{B}{\ln(10)} m \tag{4.49}$$

$$\alpha_{\mathrm{f}} = \frac{\frac{B}{\ln(10) c_1}}{c_2} = \frac{B}{\ln(10)} \frac{m^2}{b} \tag{4.50}$$

5. RESULTS

In this chapter the results for the quasi-static and dynamic measurements, introduced in Sec. 3.2, are presented.

The quasi-static temperature ramp experiments used laser diffraction to investigate the near-surface glass temperature of PMMA and PS samples of various molecular weights. Estimates of the near-surface glass temperatures, $T_{\mathrm{dec},0}$, are extracted from these data and compared to the corresponding bulk T_{g}'s obtained from DSC measurements.
The temperature ramp experiments were also performed with the use of an AFM on gratings with the same grating constant (about 650 nm) to be able to examine possible differences in the measuring techniques: laser diffraction and AFM. The knowledge of any differences in the techniques is a prerequisite for the AFM examinations of gratings with small grating constants. The investigations of gratings with a small grating constant of about 250 nm were performed with the AFM to inquire into a possible increase of the surface effect, which might occur when the probing depth is reduced.

In the second part, the results of the dynamic decay experiments using laser diffraction are presented. Mastering of constant-temperature decay curves is done for PMMA and PS at different temperatures. The mastering is done by shifting the data on the logarithmic time scale (Sec. 3.2.2). In cases where the material behaves like a strong liquid, the resulting shift factors can be used to extract an activation energy for the material. In cases where the material is fragile, the activation energy is temperature dependent. The activation energy at T_{g} is related to the "fragility." A possible influence of the molecular weight on the activation energy or fragility near the surface is investigated for PMMA and PS. The shift factors are also analyzed using the free volume interpretation to extract information about the free volume fraction and the expansion coefficient.

5.1 Temperature Ramps

5.1.1 Temperature Ramps with Diffraction

Temperature Ramps with Diffraction for PMMA

The structural changes in a hot embossed polymer grating with length scales close to the wavelength of the laser light may be detected via laser diffraction. This is discussed in more detail in Secs. 3.2.1 and 4. A decrease in the amplitude of a sinusoidal grating, caused by an increase in mobility of the polymer chains, can be measured via the decrease in diffracted intensity. As soon as the near-surface glass temperature is reached, the diffracted intensity continuously decreases until it can no longer be distinguished from the background. The background intensity is determined prior to the diffraction measurements.

Figure 5.1 displays a compilation of data sets for PMMA of four different molecular weights. The data sets for each molecular weight are measured at six different ramping rates. The data are normalized to the initial intensity and each ramping rate is shifted on the y-axis for clarity.

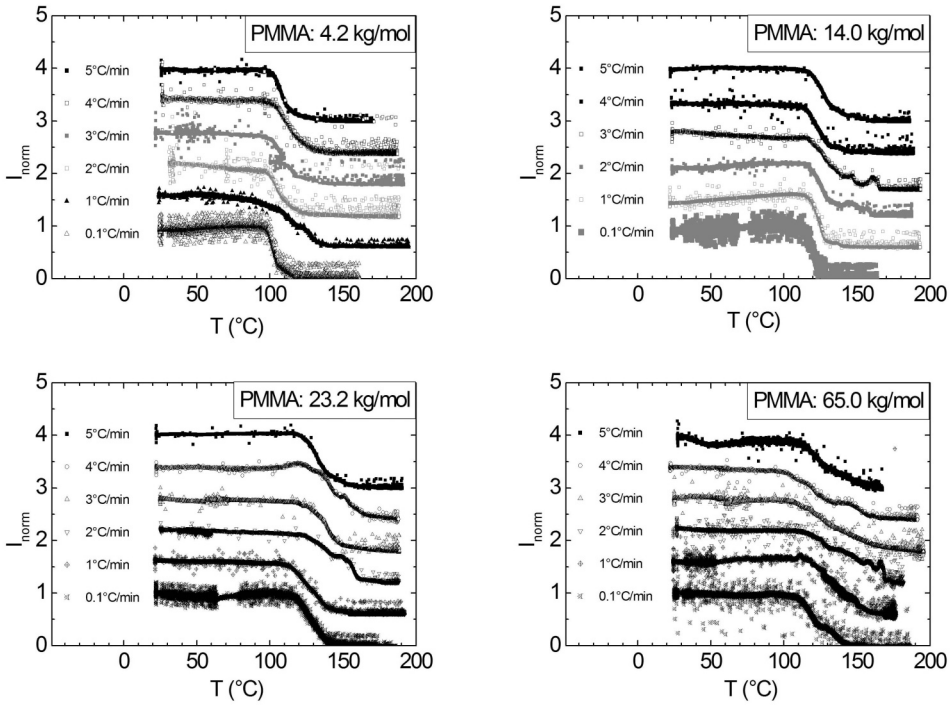

Figure 5.1: Diffracted intensity detected at different heating rates for PMMA of M_w = 4.2, 14.0, 23.2, and 65.0 kg/mol. The intensities are normalized to the initial intensity and offset on the y-axis.

From each data set with a different ramping rate the temperature T_{dec} is determined. The first kink in the diffracted intensity indicates T_{dec}. The temperature T_{dec}, at which the amplitude of the grating starts to decrease, is extracted as described in Fig. 3.11 in Sec. 3.2.1. The data are then extrapolated linearly to determine a T_{dec} at a zero heating rate, referred to as $T_{\mathrm{dec},0}$. The extrapolation is depicted in the following graphs (Fig. 5.2). The T_{dec}'s do not show a dependence on the heating rate, either through the logarithm or a dependence as stated in [Bas98]. The scatter of the data points seems larger for high molecular weights and may be caused by entanglement. The straight lines indicate the linear extrapolation of the data. Both the surface $T_{\mathrm{dec},0}$ and the bulk T_{g} for a zero heating rate were determined by linear extrapolation.

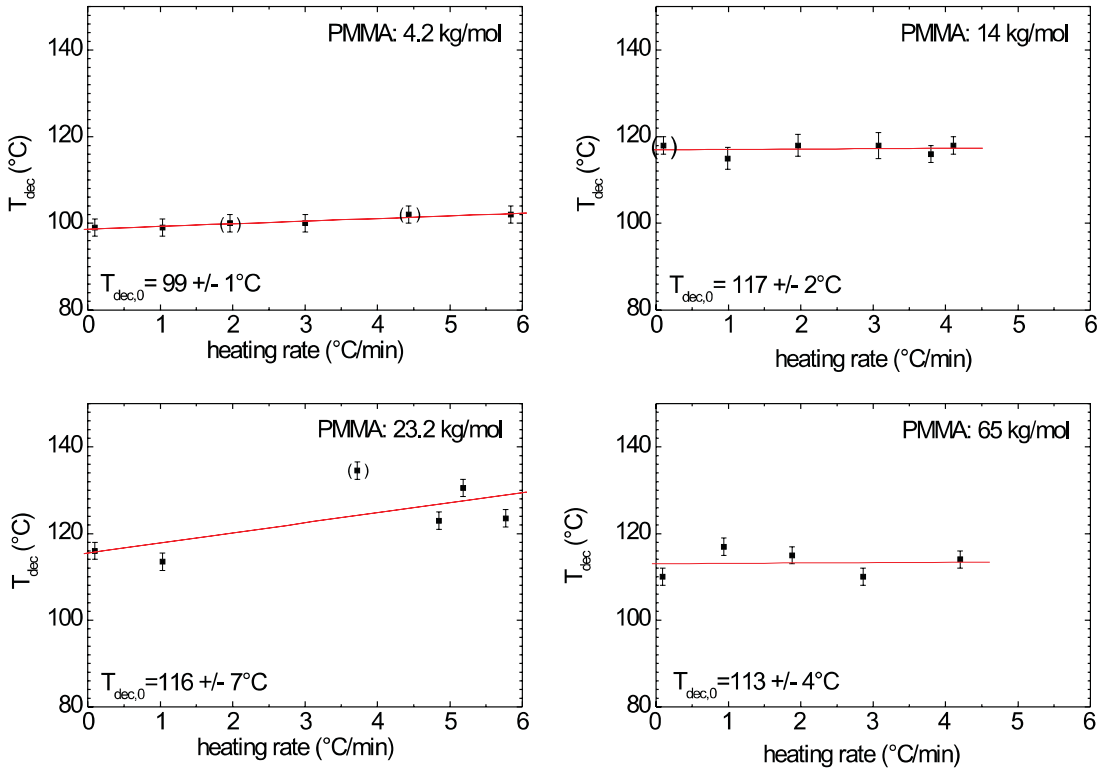

Figure 5.2: Decay temperatures determined for PMMA of M_{w} = 4.2, 14.0, 23.2, and 65.0 kg/mol at different heating rates with linear fit to extrapolate data to a 0 °C/min heating rate.

The temperatures $T_{\mathrm{dec},0}$ for PMMA can now be compared with bulk glass temperatures $T_{\mathrm{g,bulk}}$ at a 0 °C/min heating rate. The absolute temperature values for $T_{\mathrm{dec},0}$ and $T_{\mathrm{g,bulk}}$ are listed in table 5.1 and plotted in Fig. 5.3.

M_{w}(kg/mol)	4.2	14.0	23.2	65.0
$T_{\mathrm{dec},0}$(K)	372±1	390±2	389±7	386±4
$T_{\mathrm{g,bulk}}$(K)	370±2	390±2	391±2	396±2

Table 5.1: Temperatures $T_{\mathrm{dec},0}$ and $T_{\mathrm{g,bulk}}$, both extrapolated to a 0 K/min heating rate.

The glass temperatures determined near the surface and in the bulk show a different dependence on the molecular weight. This is evident in Fig. 5.3.

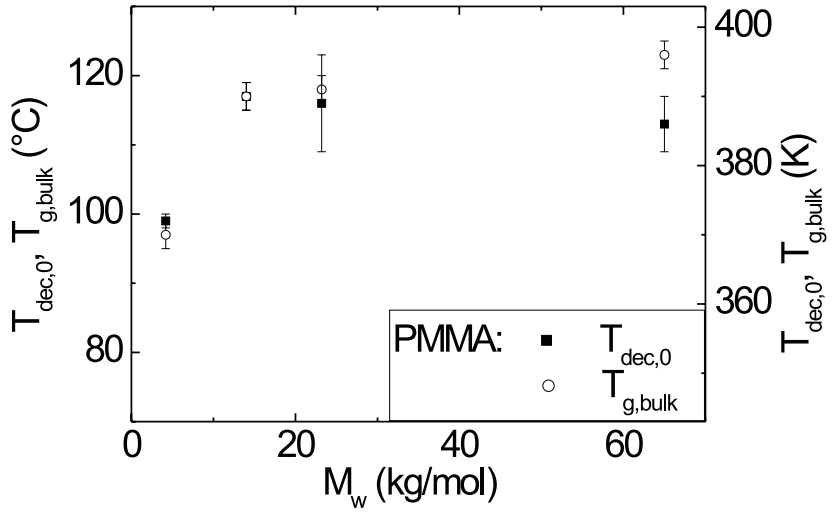

Figure 5.3: Comparison of the near-surface glass temperatures $T_{\mathrm{dec},0}$ (solid squares) with the bulk values $T_{\mathrm{g,bulk}}$ (open circles) for PMMA with M_{w} = 4.2, 14.0, 23.2, and 65.0 kg/mol. A reduced surface value for 65.0 kg/mol is apparent.

For molecular weights below M_{c} (between 20 and 22 kg/mol), the bulk values of the glass temperature are equal, within the errors, to the near-surface values. Above M_{c}, however, a reduction of T_{g} near the surface is apparent. For 65.0 kg/mol the difference between $T_{\mathrm{dec},0}$ and $T_{\mathrm{g,bulk}}$ is definitely larger than the error.

Another method to analyze the data is to fit the transition to a hyperbolic tangent function, as described in Sec. 3.2.1. The value T_1 is the temperature at the inflection point and T_2 represents the half-width of the transition. Values slightly higher than, but still comparable to, T_{dec} are the values $T_{\mathrm{dec,fit}} = T_1 - T_2$. $T_{\mathrm{dec,fit}}$ is a second estimation of the glass temperature

near the surface. This method enables one to extract not only the temperature $T_{\mathrm{dec,fit}}$, but also to get an impression about the width of the transition. The width of the transition represents the temperature difference necessary for the total decay of the grating. The fits of the normalized intensities for the four molecular weights are put together in Fig. 5.4. The data for each heating rate are shifted on the y-scale for clarity.

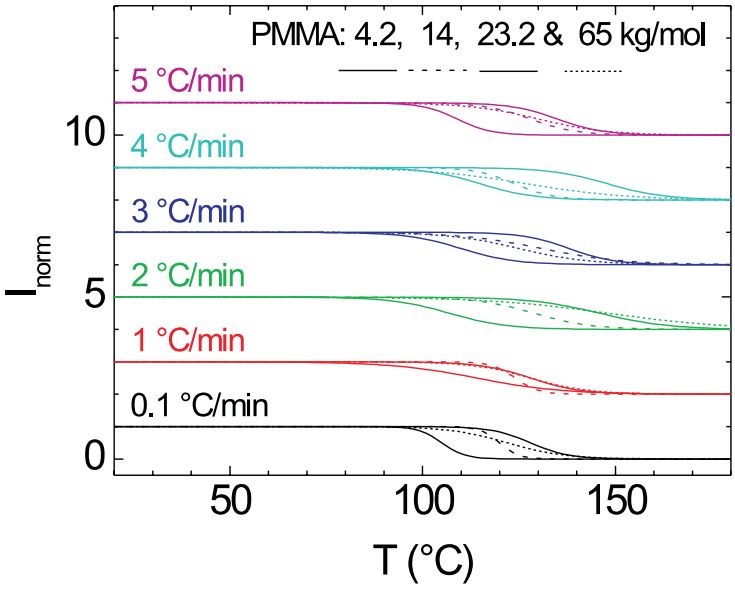

Figure 5.4: Comparison of fits to the ramping data for PMMA with M_{w} = 4.2, 14.0, 23.2, and 65.0 kg/mol. Each family of curves with data measured for four different molecular weights is shifted on the y-scale (equally spaced) for the six different heating rates; from bottom to top, 0.1, 1, 2, 3, 4, and 5 °C/min.

Here, we see the same behavior as seen before: the transition zone shifts to higher temperatures with increasing molecular weight up to 23.2 kg/mol, which is close to the critical molecular weight M_{C}, and shifts back again to lower temperatures for 65.0 kg/mol. The largest difference between the curves measured for different molecular weights is apparent at a heating rate of 2 °C/min.

The temperatures $T_{\mathrm{dec,fit}}$ and the linear extrapolations to a 0 °C/min heating rate are shown in Fig. 5.5. The temperatures at which the grating is completely erased is referred to as $T_{\mathrm{erase,fit}}$=T_1 + T_2. The $T_{\mathrm{erase,fit}}$'s are plotted together with the temperatures $T_{\mathrm{dec,fit}}$ to get an impression about the width of the transition. The data indicate an increasing transition width with increasing molecular weight. The decay of the grating might be hindered by entanglements, which are effective for molecular weights above $M_{\mathrm{C}} = 2M_{\mathrm{e}}$ [Mar96] and provoke the existence of cooperative units. If the surface effect is caused by confined cooperative units, it

should be more pronounced for larger cooperative units, *i.e.*, for longer chains.

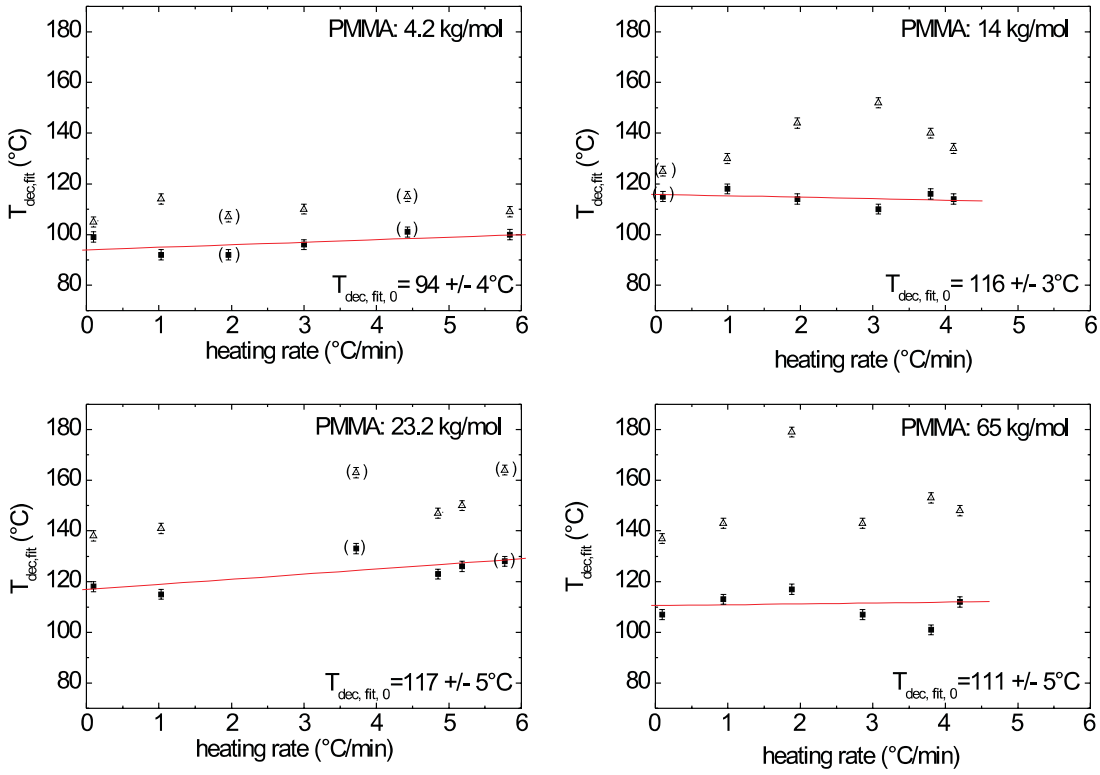

Figure 5.5: The temperatures $T_{\mathrm{dec,fit}} = T_1 - T_2$ (solid squares) and $T_{\mathrm{erase,fit}}$=$T_1 + T_2$ (open triangles) are plotted for molecular weights of PMMA: M_{w} = 4.2, 14.0, 23.2, and 65.0 kg/mol. The straight lines are the linear fits to the $T_{\mathrm{dec,fit}}$ values to determine the temperature $T_{\mathrm{dec,fit},0}$ at a 0 °C/min heating rate.

Figure 5.6 shows the temperatures $T_{\mathrm{dec,fit},0}$ determined from the graphs in Fig. 5.5. They are plotted, along with the bulk glass temperatures, versus molecular weight. Similar results are obtained for $T_{\mathrm{dec,fit},0}$ and $T_{\mathrm{dec},0}$; however, the current analysis has the advantage of the additional information about the transition width. The transition width is smallest for 14.0 kg/mol and then shows a slight trend toward increasing transition width with increasing molecular weight, as seen in the difference of the values $T_{\mathrm{dec,fit},0}$ and $T_{\mathrm{erase,fit},0}$.

The dependences of $T_{\mathrm{dec},0}$ and $T_{\mathrm{dec,fit},0}$ on molecular weight are very similar. However, the errors are large since the whole data set was fit with the tanh-function and not only the kink. Nevertheless, the results show that the behavior is independent of the analysis, which gives us reason to believe that surface confinement leads to a decrease of the glass temperature for molecular weights above M_{C}, certainly for PMMA of 65.0 kg/mol.

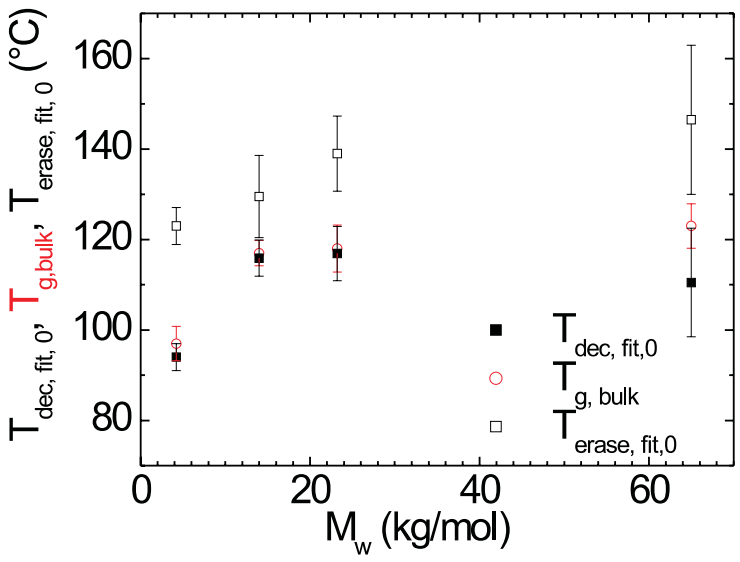

Figure 5.6: Comparison of extrapolated decay temperatures $T_{\mathrm{dec,fit,0}}$ (solid squares) with bulk values $T_{\mathrm{g,bulk}}$ (open circles) for PMMA of M_{w} = 4.2, 14.0, 23.2, and 65.0 kg/mol. The width of the transition is the temperature range between the values of $T_{\mathrm{dec,fit,0}}$ and $T_{\mathrm{erase,fit}}$ (open squares).

Temperature Ramps with Diffraction for PS

The effect of the polymer side chains is investigated using polymers with almost the same chain length but side chains with different chemical structure. The choice was PS, which unlike PMMA, has a bulky, non-polar phenyl ring as a side group. The molecular weight range – and thus the range of radii of gyration – are chosen to be the same for PS as they were for PMMA. Thus, a direct comparison of the two materials is possible.

In Fig. 5.7 the ramping data sets – each with normalized diffraction intensities and each vertically offset for the different heating rates – are displayed for PS's of five different molecular weights: 3.47, 10.3, 18.0, 34.0, and 65.0 kg/mol. Comparing the graph for 10.3 kg/mol with the other four graphs, it becomes obvious that further improvement of the embossing technique (better statistics due to larger grating areas with better imprint quality) increases the diffracted intensity, and thus the overall quality of the normalized data. The time interval over which the data are averaged is also increased.

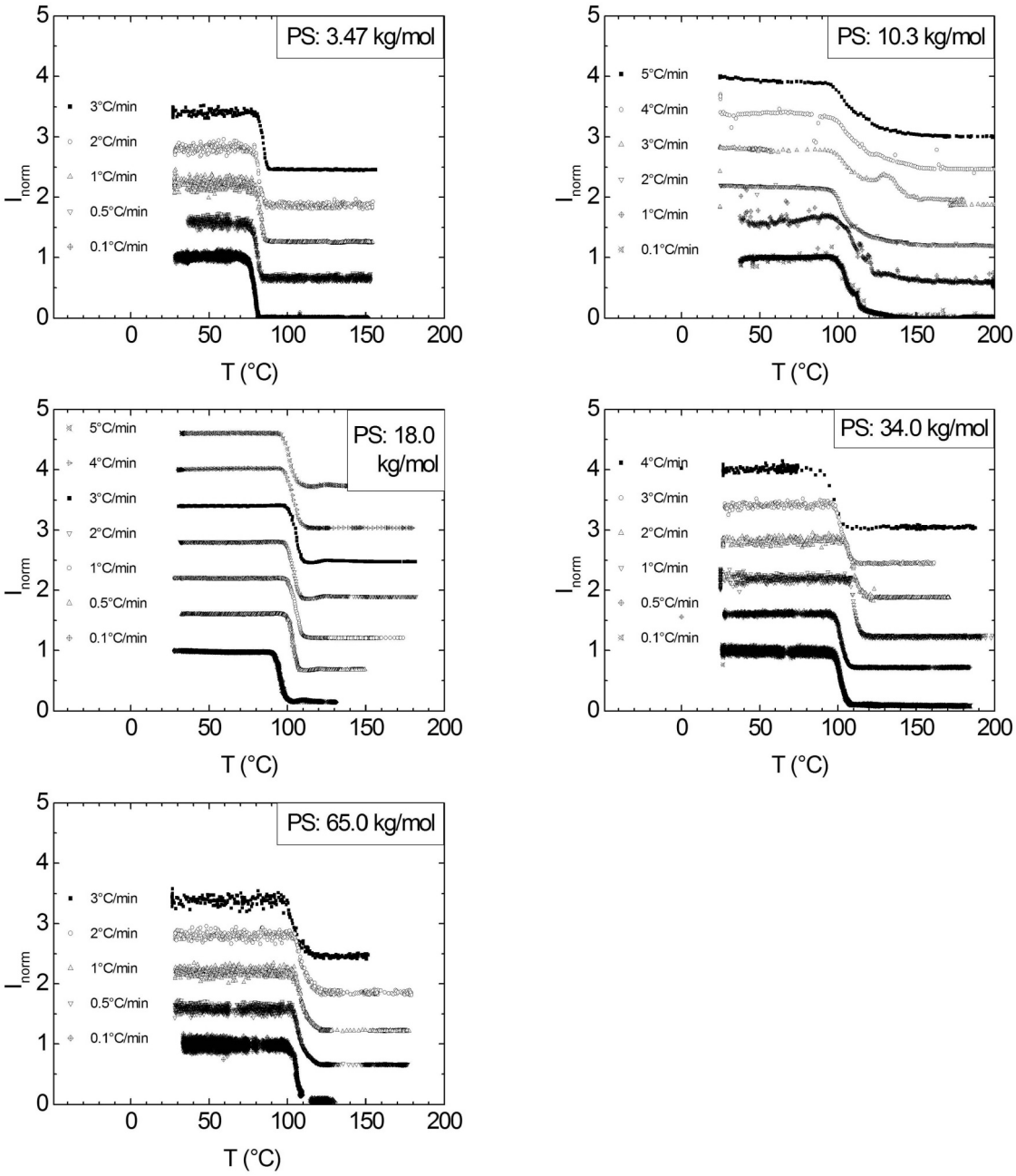

Figure 5.7: Temperature ramps at different heating rate for PS of M_w = 3.47, 10.3, 18.0, 34.0, and 65.0 kg/mol. The normalized intensities are shifted on the y-scale.

As was done before, the T_dec temperatures are determined by finding the intersection points of the lines fit to the constant initial intensities and the (approximately linear) transition zones. Both the resulting T_dec's and the linear extrapolations to determine the $T_{\mathrm{dec},0}$ temperatures at zero heating rate are plotted in Fig. 5.8.

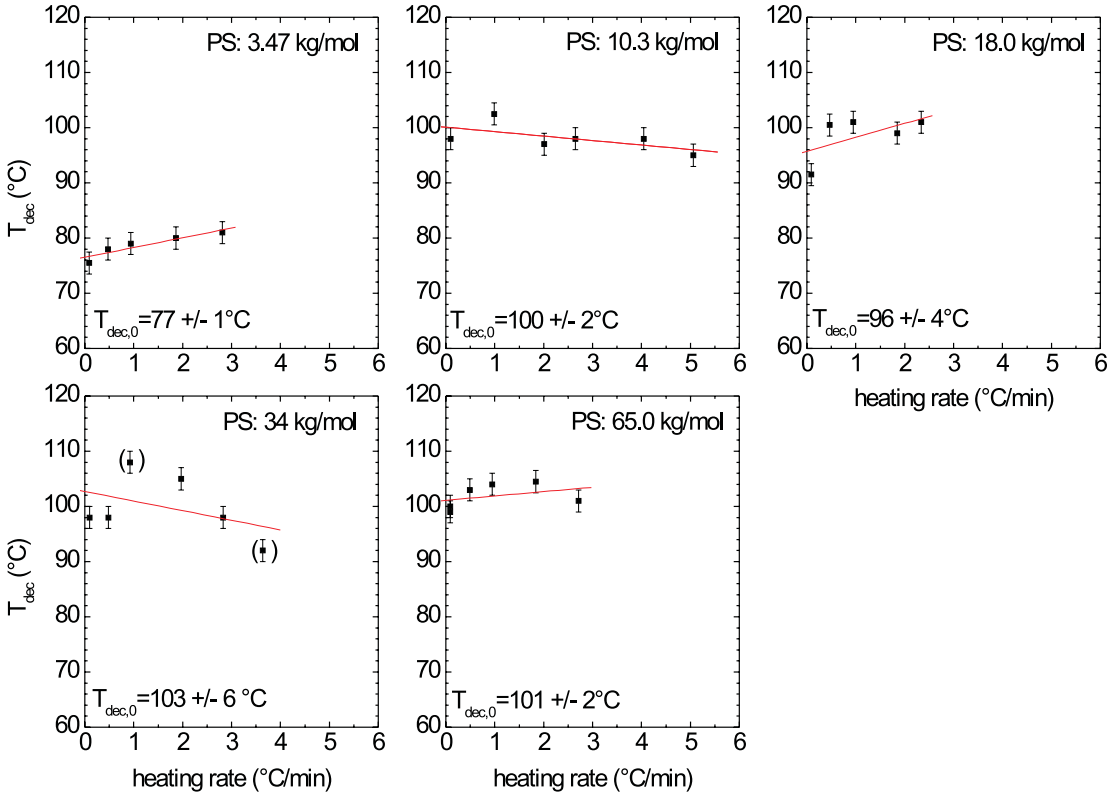

Figure 5.8: Decay temperatures determined for PS of M_{w} = 3.47, 10.3, 18.0, 34.0, and 65.0 kg/mol at different heating rates (solid squares) with linear fits to extrapolate data to a 0 °C/min heating rate. The data points in parentheses are dubious since these temperatures deviated from those expected during the temperature ramp.

Table 5.2 lists the absolute temperature values for $T_{\mathrm{dec},0}$ determined from the temperature ramping experiments for PS, along with the bulk values, determined by DSC. Both are the extrapolated values to a zero heating rate.

M_{w}(kg/mol)	3.47	10.3	18.0	34.0	65.0
$T_{\mathrm{dec},0}$(K)	350±1	373±2	369±4	376±6	374±2
$T_{\mathrm{g,bulk}}$(K)	346±2	367±2	370±2	373±2	376±2

Table 5.2: $T_{\mathrm{dec},0}$ and $T_{\mathrm{g,bulk}}$ for PS extrapolated to a 0 /min heating rate.

Figure 5.9, comparing the temperatures $T_{\mathrm{dec},0}$ and $T_{\mathrm{g,bulk}}$ as functions of the molecular weight, does not show such a pronounced difference between surface and bulk values as in the case of PMMA. The $T_{\mathrm{dec},0}$ values for PS with M_{w} values of 3.47 and 10.3 kg/mol are higher than the corresponding bulk values. The values for molecular weights larger than 10.3 kg/mol do not reveal a difference between $T_{\mathrm{dec},0}$ and $T_{\mathrm{g,bulk}}$, within the errors. A reduction in $T_{\mathrm{dec},0}$ at the surface with respect to $T_{\mathrm{g,bulk}}$ for $M_{\mathrm{w}} > M_{\mathrm{C}}$, as seen in case of PMMA, is not detectable in the case of PS. If there is any reduction, it is much smaller than for PMMA, probably within the range of the experimental error.

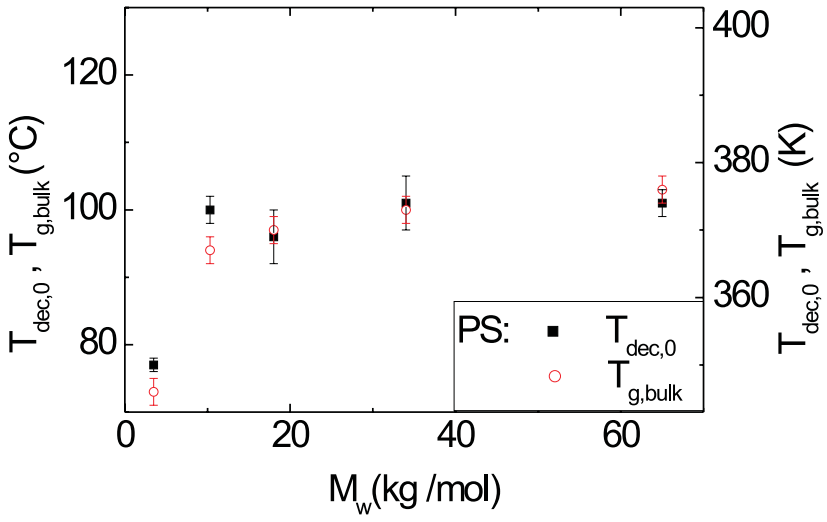

Figure 5.9: Comparison of the extrapolated decay temperatures $T_{\mathrm{dec},0}$ (solid squares) with the bulk values $T_{\mathrm{g,bulk}}$ (open circles) for PS of M_{w} = 3.47, 10.3, 18.0, 34.0, and 65.0 kg/mol

The similarities and differences between PMMA and PS are discussed in Ch. 6.

The second way to analyze the temperature ramp data is to fit the data to a tanh-function. The fit to the PS data is performed the same way as previously done for PMMA. Figure 5.10 shows the fits for the variable molecular weights at certain heating rates.

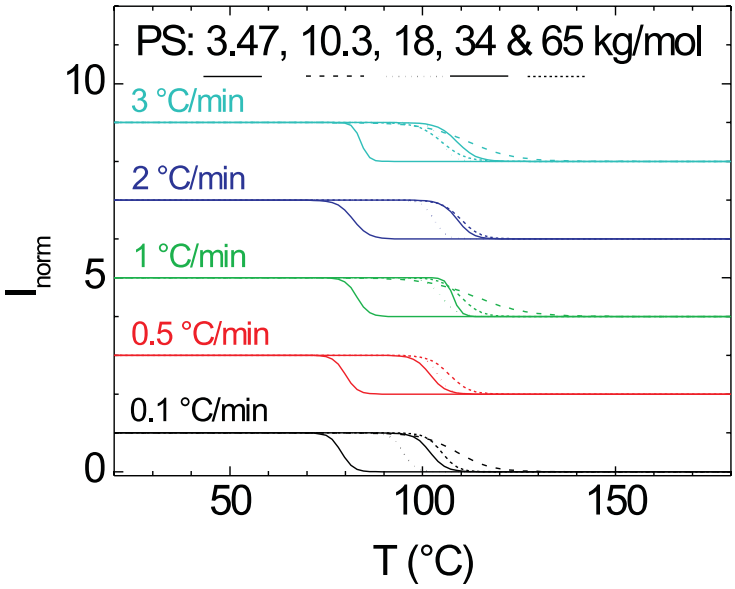

Figure 5.10: Comparison of fit ramping data of PS with M_w = 3.47, 10.3, 18.0, 34.0, and 65.0 kg/mol. The fit intensities are vertically offset equally spaced for the different heating rates, from the bottom to the top: 0.1, 0.5, 1, 2, 3 °C/min

The fit intensities for the normalized temperature ramp data of PS obviously show a more narrow transition than in the case of PMMA. The largest width is observed for M_w=10.3 kg/mol, however, this should be viewed with caution. The experimental circumstances here were different (this run was performed before improvement of the embossing technique), which also might have caused the effect. Therefore, the width at this molecular weight could be misleading in comparison with the other M_w's and we refrain from interpreting it.

From T_1 and T_2, which are extracted from the tanh-fit diffracted intensity (Sec. 3.2.1), the temperatures $T_{dec,fit}$ and $T_{erase,fit}$ are calculated. The resulting $T_{dec,fit}$ and $T_{erase,fit}$ values are plotted in Fig. 5.11. The linear extrapolations to a 0 °C/min heating rate yield $T_{dec,fit,0}$ and $T_{erase,fit,0}$.

The $T_{dec,fit,0}$ and $T_{erase,fit,0}$ were extracted from the y-intercepts of the plots in Fig. 5.11 and their molecular weight dependences are presented in Fig. 5.12.

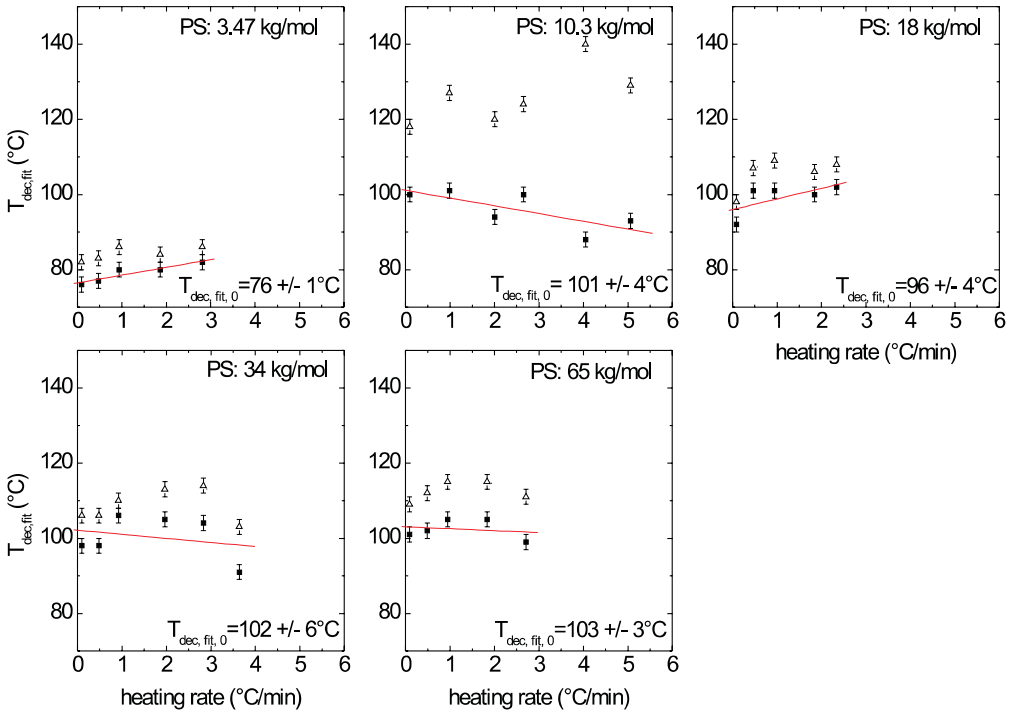

Figure 5.11: The temperatures $T_{\mathrm{dec,fit}} = T_1 - T_2$ (solid squares) and $T_{\mathrm{erase,fit}} = T_1 + T_2$ (open triangles) are plotted for each molecular weight of PS investigated (M_{w} = 3.47, 10.3, 18.0, 34.0, and 65.0 kg/mol). The straight lines are the linear extrapolations of the fit values to determine the temperature $T_{\mathrm{dec,fit,0}}$ and $T_{\mathrm{erase,fit,0}}$ at a 0 °C/min heating rate.

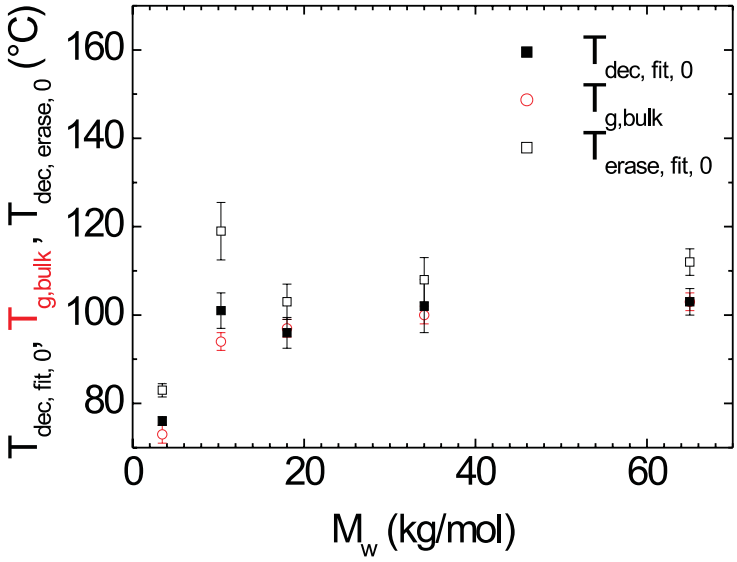

Figure 5.12: Comparison of $T_{\mathrm{dec,fit,0}}$ (solid squares) with bulk values $T_{\mathrm{g,bulk}}$ (open circles) for PS of M_{w} = 3.47, 10.3, 18.0, 34.0 and 65.0 kg/mol. The temperatures $T_{\mathrm{erase,fit,0}}$ are also plotted for the different molecular weights (open squares) to get an impression about the width of the transition.

Judging from these measurements, we expect almost the same trend for the glass temperature near the surface as we do in the bulk. Assuming there is also a surface anomaly in the case of PS, it seems to be rather for the small molecular weights, 3.47 and 10.3 kg/mol. It seems like the crossover point for PS is M_e and not M_c=2M_e. For the two molecular weights with $M_w < M_e$, the values for the surface are higher than the ones for the bulk. In the event there is an anomaly for M_ws higher than 10.3 kg/mol, the sensitivity of our measurement is not sufficient to detect it. The sensitivity of the technique can be increased by using gratings with a smaller grating constant. In this case a thinner surface layer is probed and the contribution of the anomalous surface layer is larger. The relation between grating constant and probing depth is described in Sec. 4.1.

5.1.2 Temperature Ramps with Atomic Force Microscopy (AFM)

The results from the temperature ramp experiments with diffraction show an effect of the surface on the glass temperature, at least in the case of PMMA. The aim of the following measurements is to investigate if there is a detectable increase of sensitivity by probing a thinner surface region. An increase of surface sensitivity can be achieved by using gratings with smaller grating constants, as explained in the Sec. 4.1. Appropriate masters with a small grating constant, which can still be produced by a photo-lithographic process, may have a grating constant of about 250 nm. The hot-embossed polymer gratings with a small grating constant, however, require a different technique, other than diffraction, to be able to detect the changes in amplitude: since the diffraction limit for small structures is half the incident wavelength, the wave vectors cannot be matched anymore. The alternative technique chosen is AFM.

It is essential to compare the different measuring techniques with gratings of the same size and material before turning to gratings with small grating constants, which cannot be measured with diffraction. Possible differences caused by the type of measurement can thus be revealed and thus be taken into consideration when analyzing further experiments.

Unfortunately, using AFM as the technique of investigation, continuous data acquisition during the ramping of the temperature was not possible due to the wide drift of the system. Thus, the AFM images are acquired after stepwise increases of the temperature by 5 °C with consecutive annealing for 5 min. The temperature is increased until there is no observable structural anisotropy. The images corresponding to each 5 min annealing step are taken after quenching the sample to room temperature. The AFM height measurements are performed in

contact mode on an area of $10\ \mu m \times 10\ \mu m$. A large scanning area is necessary to ensure good statistics. The PSD analysis option of the Nanoscope III software is used to determine the 1D power spectral densities of the images. We repeat the AFM analysis of a 641 nm PS grating to confirm the reliability of the measurements. The PSD data extracted from the AFM images, measured after each annealing step, are offset to make it possible to see the decrease of the peak of the gratings' PSD. The PSD series for independent measurements look similar, as shown in Fig. 5.13 (top graphs: measurement a, bottom graphs: measurement b). On the left-hand side the graphs are displayed with the whole spectrum from λ= 0 to 10 μm, on the right-hand side a zoom into the peak region shows more details of the peak behavior.

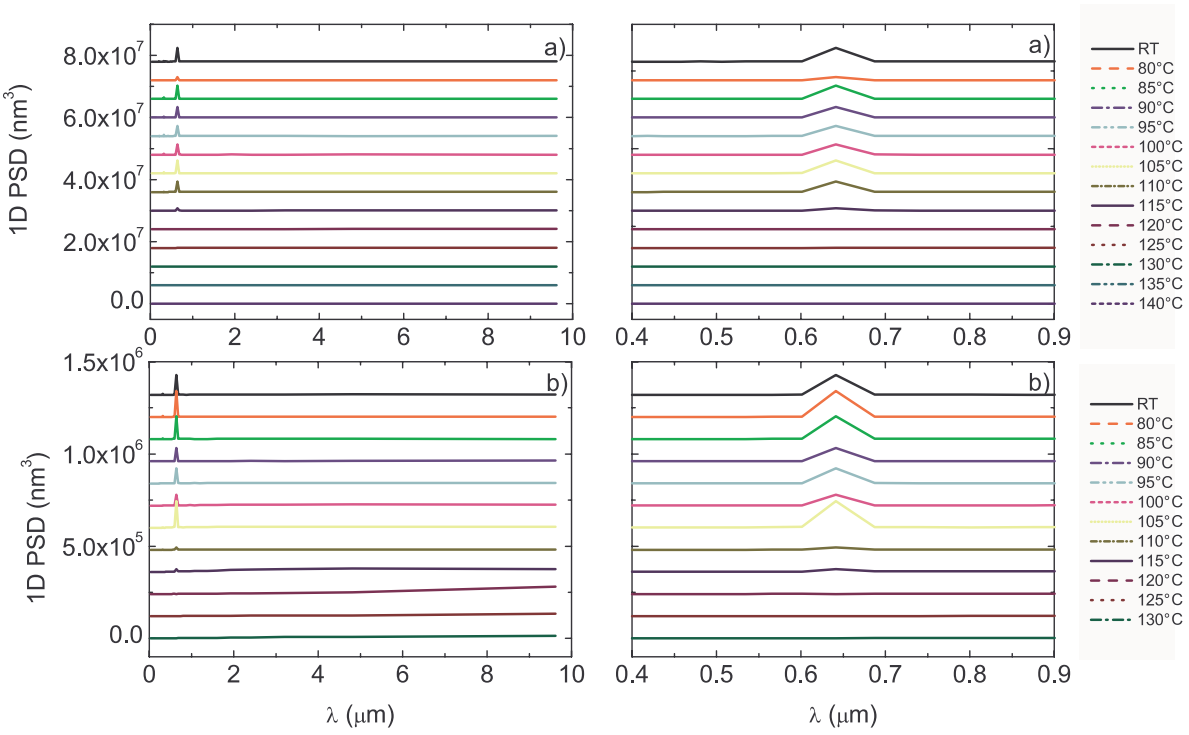

Figure 5.13: PSDs of two measurements (a and b) extracted from AFM height images of 641 nm PS gratings. The PSDs measured after each temperature are vertically offset for clarity. The graphs on the left-hand side show the whole spectrum, the graphs on the right-hand side are zooms into the wavelength range with the peak resulting from the sinusoidal grating.

The PSDs corresponding to different temperatures only show one peak. This only peak in the PSDs is at a wavelength which is equal to the grating constant of λ = 641 nm. The fact that there is only one peak is evidence of a good sinusoidal grating. The gratings do not appear to deviate from the sinusoidal shape during the heating process. The difference in peak height (max. PSD values) for the two independent measurements at room temperature is caused by

local inhomogeneities of the embossed gratings' amplitudes.

A comparison of the normalized diffracted intensities and maximum PSD values obtained from PS samples with M_w=65.0 kg/mol, investigated at the same effective heating rate of 1 °C/min, shows astonishingly good agreement. The comparison is presented in Fig. 5.14.

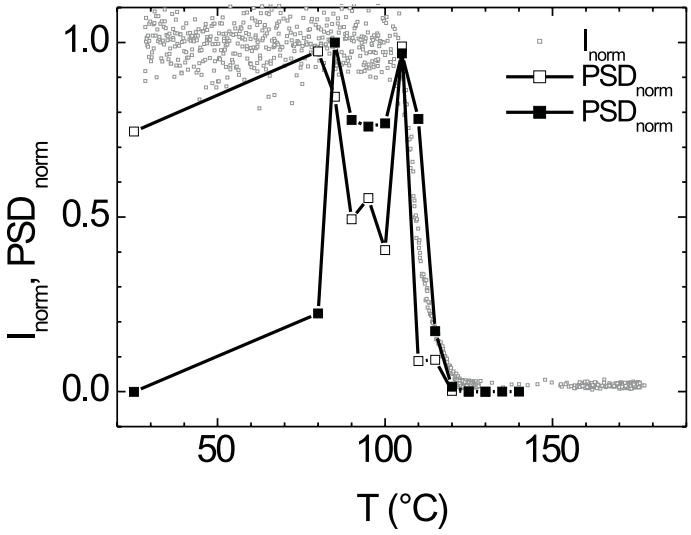

Figure 5.14: Comparison of diffracted intensities (small open squares, high density) and PSDs for the peak values (measurement a solid and measurement b open squares), which represent the grating amplitude. Both measurements are performed at effective temperature ramps of 1 K/min using PS gratings with M_w=65 kg/mol and λ=641 nm.

Using AFM as an investigation technique, the kink in the PSD temperature data cannot be determined as precisely as in the diffraction experiments since the temperature steps are much larger (5 °C in comparison to $\frac{1}{60}$ °C). Also, the scatter in the PSD data is higher. Alignment is definitely critical, but utmost care has been taken to keep the scanning area the same. The peak-like structure in the PSD data could also be due to a higher sensitivity of AFM to small changes in amplitudes. During the cooling after the embossing process or even during the quenching step, there may be an incomplete relaxation of the film. This may also be a reason for the initial increase of the PSD, which is apparent in Fig. 5.14. The peaks are at 80 °C and 105 °C in measurement (a), at 85 °C and 105 °C in measurement (b).

The results from the AFM and laser-diffraction analysis are quite comparable. It seems that the detection technique does not have a recognizable effect on the main features of the tem-

perature ramp data. Thus, we do not expect, *a priori*, any systematic effects when investigating gratings with smaller grating constants with AFM.

The gratings with a grating constant of about 250 nm are also sinusoidal. This becomes obvious when one looks at the PSD data extracted from AFM height images. The scanning area is $10\mu\mathrm{m}\times10\mu\mathrm{m}$ and the AFM measurements are performed in contact mode. The PSDs are extracted from the height images taken after each temperature step and are vertically offset for clarity. The PSD data for the whole spectral wavelength range and a zoom into the wavelength range of the peak are shown in Fig. 5.15.

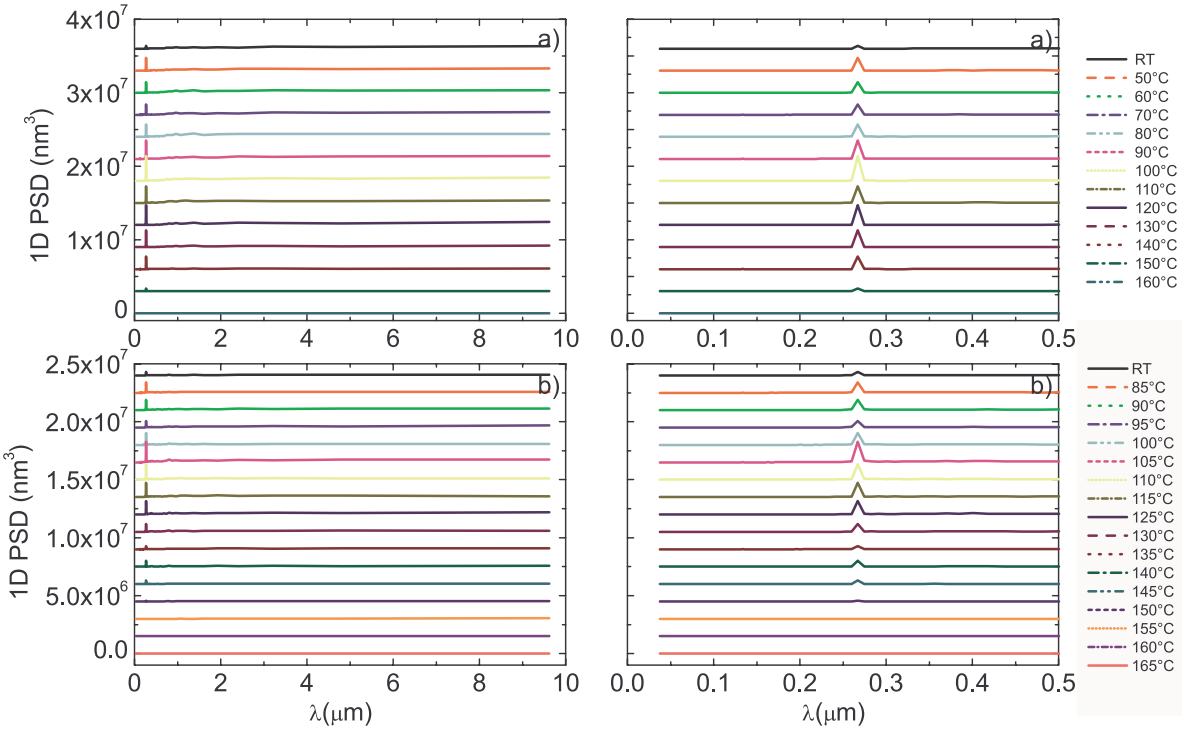

Figure 5.15: The PSDs are extracted from AFM height images of 267 nm PMMA gratings and each PSD corresponding to a different temperature is shifted vertically for better display. The whole spectrum of the PSD data, obtained from two independent experiments, (a) and (b), is shown on the left-hand side and a zoom into the range of the gratings' wavelength on the right-hand side. The PMMA gratings with M_w=65.0 kg/mol are investigated at a effective heating rate of 1 °C/min.

From the test with 641 nm gratings, we know that the diffraction intensities and the peaks of the PSDs show the same behavior. So it should be possible to find out if there is an enhancement of the sensitivity when the probing depth ζ ($\zeta=\frac{\lambda}{2\pi}$, see Sec. 4.1) is reduced from about 100 nm to 40 nm. The diffracted intensities of a 641 nm grating and the peaks of the PSD extracted from the height images of 267 nm gratings need to be compared. Figure 5.16 shows the

diffracted intensities and peaks of the PSDs for PMMA gratings with λ = 641nm and 267 nm, respectively.

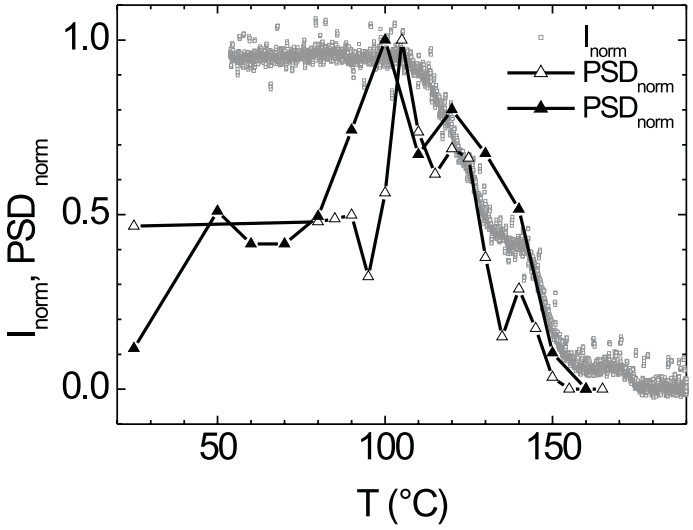

Figure 5.16: Comparison of diffracted intensities (small open squares, high density) and PSD peak values (bold squares), representing the grating amplitude, measured at temperature ramps of 1 °C/min. Both measurements are performed using PMMA with a molecular weight of 65.0 kg/mol. The grating constants for diffraction (λ = 641 nm) and AFM (λ = 267 nm) analysis are different. The second confirmation data for AFM has less data points, taken at a rate of 10 °C/10min.

The AFM measurements with less than half the probing depth do not show substantial differences when compared with the results from the laser diffraction investigations. One possible explanation is that the surface effect is confined to a very small surface region, but is so strong that it influences the glass temperature measurements even when probing a much larger region. Assuming a surface region of 1 or 2 nm, as often done in the three layer model [FM00b], this is only 1 and 3 percent of the probing depth for the 267 nm and 641 nm gratings, respectively. Therefore, this may be the reason why no difference can be detected. Indirectly, this supports the model of a very thin liquid surface layer, as suggested by the three layer model. To be able to sense glass temperatures of the first few surface nanometers, very small grating constants are necessary. Gratings with a 40 nm grating constant (ζ=6 nm) made from reconstructed silicon surfaces [RWH$^+$01] are used to perform the AFM analysis. However, there are experimental difficulties, which are quite difficult to be overcome: the grating amplitude of the reconstructed surfaces decreases with decreasing grating constant and is about 1 nm for

the 40 nm gratings. Hot embossing the nano-gratings works, which is verified by AFM contact mode imaging. However, contact imaging of the surface and performing stepwise temperature ramps does not lead to a reasonable result. The inconvenience is that the gratings are triangular, not sinusoidal, and the periodicity is not perfect; there is a distribution of possible grating constants. Together with the local inhomogeneities causing variations in the PSDs comparable to the variations induced by the decrease of the amplitude, this experiment seems impossible with the current setup. Possibly, integration of the spectra, automated feature tracking, and high temperature stability will improve the data acquisition significantly. Another strategy would be to develop a technique to produce masters with small grating constant, high periodicity, and aspect ratios so that both AFM PSD analysis and hot embossing are possible. One example would be the progressing technique of e-beam writing to create the master.

Another explanation for the lack of a difference when using different probing depths could be a dominating cooperative process such as the ”cage” effect from the mode coupling theory. In the case of extended cooperative motion, a reduction of the probing depth from 100 to 40 nm would not have a strong effect since the surface polymer chains are pinned by the cage. The dominant contribution to the diminishing T_{g} would rise from the motion of clusters. The movement of clusters, however, should be noticeable when one considers the activation energies for the alpha relaxation process. A chain-length or molecular-weight dependence of the activation energy could indicate cooperative motion.

The structure of the PMMA temperature ramp data presents interesting features. Both the diffracted intensity and the peak values of the PSDs from the AFM measurements show maxima around 120 and 140 °C. These could be caused by surface dynamics like a rotation of methyl side chains or the development of capillary or density waves.

The question now is, whether the reduction in glass temperature is connected with different dynamics at the surface. This question will be treated in the next section.

5.2 Decay Experiments with Diffraction: Surface Dynamics

5.2.1 Mastering

Having in mind the results of the previous section, one wonders whether the anomalous T_{g} at the surface is connected with an increased segment mobility or cooperative motion close

to the surface. The energies necessary to activate the α relaxation and the value of the Kauzmann temperature provide information about the state of the polymer at a given temperature. One way to investigate dynamic properties of the polymer is to perform decay experiments, which record the changes of the surface grating amplitude with time at different, but constant, temperatures close to T_{g}. The trend of the decrease in intensity with time is dependent upon the chosen temperature. The experimental temperatures are chosen close to T_{g} to be able to observe at least a partial decay of the grating in the experimentally measurable times. If time-temperature superposition (see Sec. 4.3) holds, it is possible to accelerate relaxation processes by increasing the temperature. A much wider time range can therefore be accessed by creating a master curve. Starting from the intensity data measured at a reference temperature, T_{ref}, the mastering is accomplished by dialating times scales for measurements at temperatures higher than T_{ref} and compressing the time scales for temperatures below T_{ref}. It is advantageous to choose a reference temperature at which the intensity shows a pronounced decay behavior with time. The best possible mastering is achieved by choosing different reference temperatures and transforming the gained parameters from one reference temperature to another (equation (4.39)).

Sets of intensity curves measured at various decay temperatures were collected for PMMA and PS of different molecular weight.

Mastering for PMMA

The log-log plots of the normalized intensities with the original time scales (left-hand graphs), as well as the same intensity data with a rescaled time using the shift factors $\log(a_{\mathrm{T}})$ (right-hand graphs), are presented in Fig. 5.17. The right-hand graphs demonstrate that it is possible to create master plots.

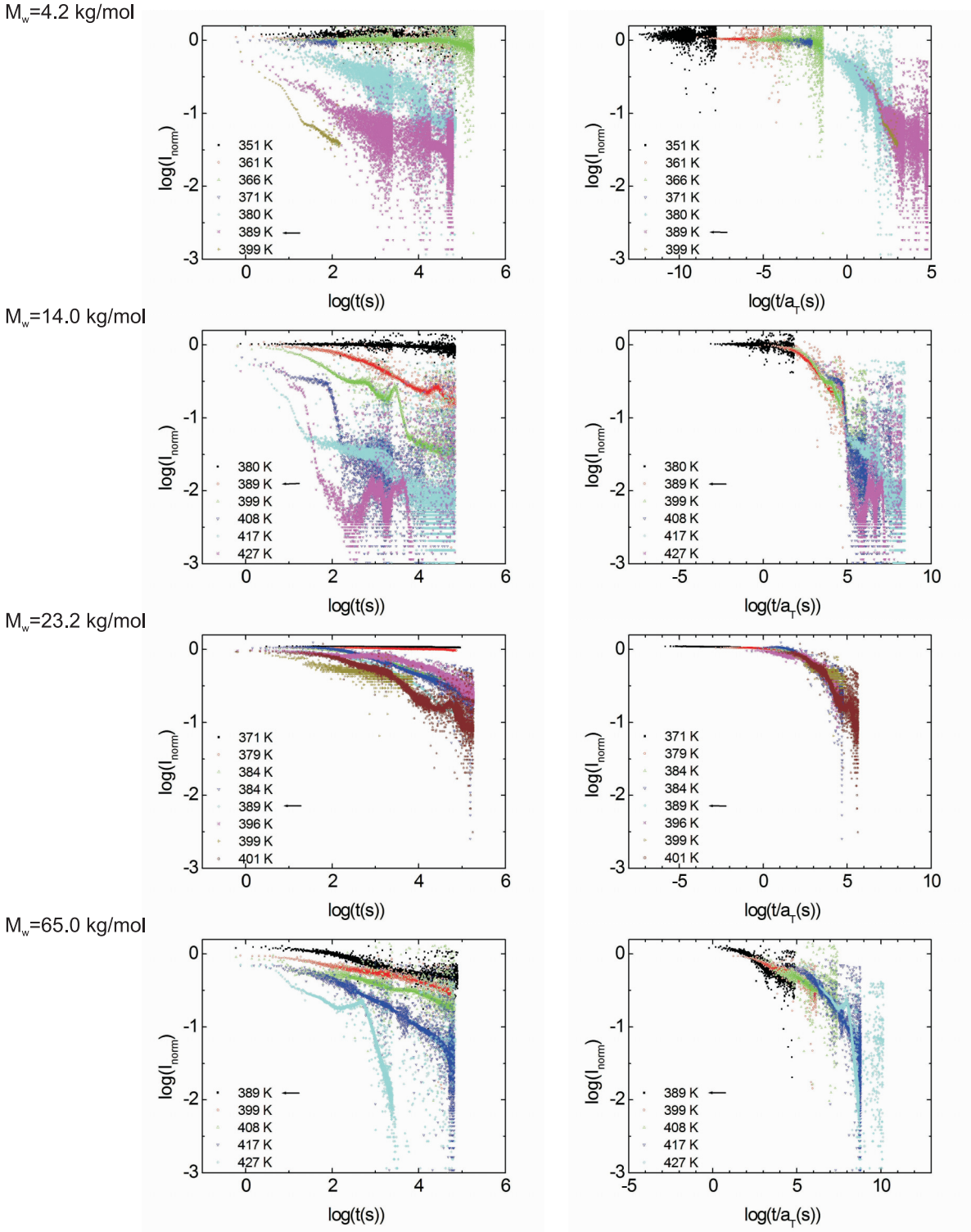

Figure 5.17: Log-log plot of the normalized intensities from dynamic measurements of PMMA with M_w=4.2, 14.0, 23.2, and 65.0 kg/mol versus the raw and shifted time. The log-log graphs on the left-hand side show the normalized intensities from the measurements at different temperatures. A temperature prefactor, which considers the changes of the visco-elastic functions (see table 4.1), was applied to the normalized intensity. On the right-hand side, the same data are plotted, but the single data curves are shifted on the logarithmic time scale so that features match. The data are shifted in respect to the data measured at T_{ref}, indicated by an arrow.

The information gained from mastering spans time scales much larger than the experimental ones ($t_{\mathrm{exp}} \approx 10^6$s, $t_{\mathrm{tot}} \approx 10^{12}$ s). The deviations of the single data sets from a common curve for long experimental times may be caused by capillary waves or density gratings. The data are deliberately mastered to match the first part and the general trend of the data, rather than to make the long-time intensities overlap. Consequently, a spread in the master curves is seen for long times.

The dialation and compression factors for the time scale a_{T} are obtained from the matching of these data curves. The logarithm (base-10) of the values a_{T} is plotted versus the respective temperatures in Fig. 5.18.

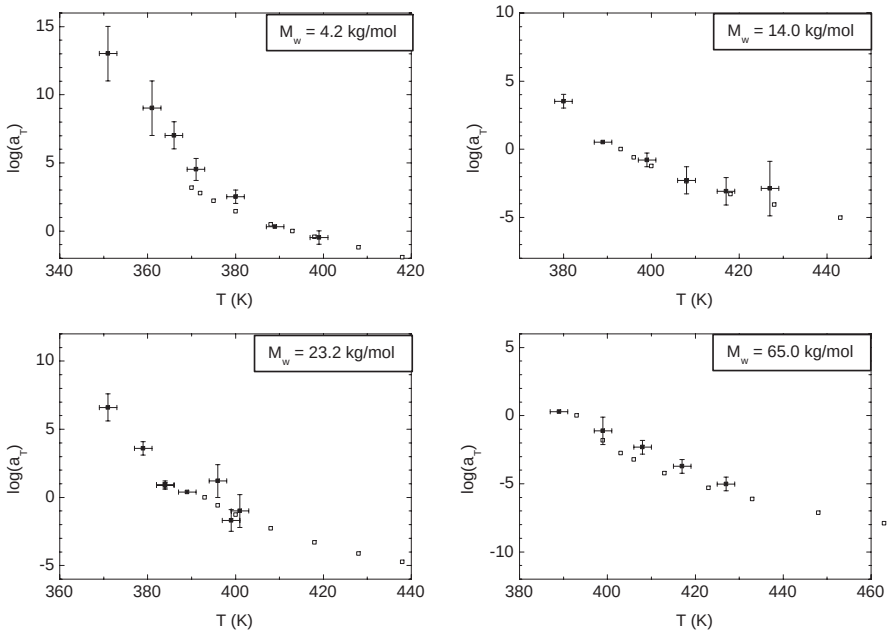

Figure 5.18: The shift factors obtained from the mastering of the PMMA data (Fig. 5.17) are plotted versus the respective temperatures. At T_{ref} the shift value is zero, $\log(a_{\mathrm{T}})|_{T=T_{\mathrm{ref}}} = 0$. The shift factors, determined with bulk rheology measurements, are represented by the open squares.

Mastering for PS

The matching of intensity-time data measured at different temperatures, the mastering, is also performed for PS. The temperatures are chosen to be lower than in the corresponding PMMA measurements since PS has a lower T_{g}. The normalized intensities for PS versus the raw and the rescaled time values are depicted in Fig. (5.19).

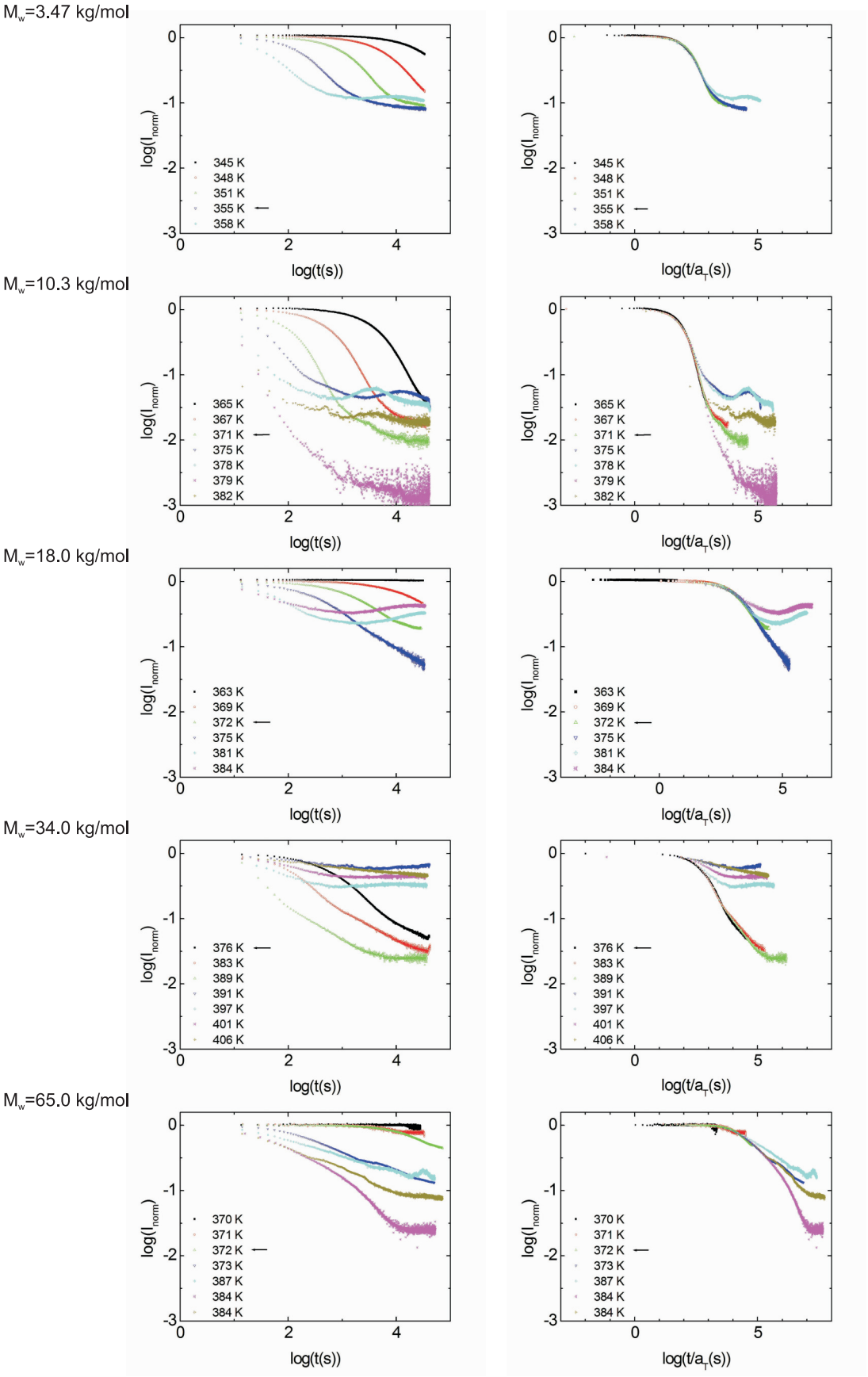

Figure 5.19: Normalized intensities from dynamic measurements of PS with M_w=3.47, 10.3, 18.0, 34.0, and 65.0 kg/mol plotted versus raw time (left-hand side graphs) and rescaled time scale (right-hand graphs). A temperature prefactor, which considers the changes of the visco-elastic functions (see table 4.1), was applied to the normalized intensity. T_{ref}'s are indicated by the arrows.

The corresponding shift factors, $\log(a_{\mathrm{T}})$, for PS are extracted from the mastering procedure using the data measured at T_{ref} as the reference. The values are plotted versus the corresponding temperatures in Fig. 5.20.

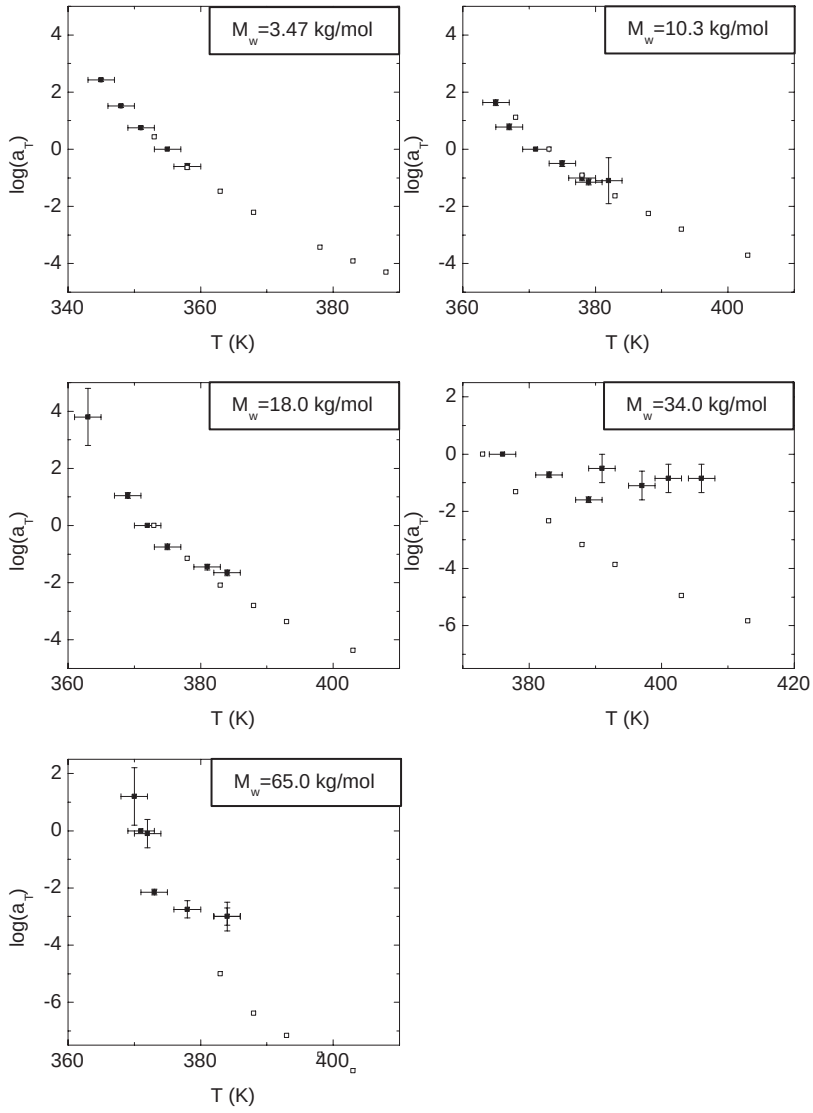

Figure 5.20: The shift factors obtained from the mastering of the PS surface data (Fig. 5.19) are plotted versus the respective temperatures. The shift factors at T_{ref} are zero, $\log(a_{\mathrm{T}})|_{T=T_{\mathrm{ref}}} = 0$. The bulk shift factors were transformed to the same reference temperature as for the surface values using equation (4.39) (open squares).

The shift factors, $\log(a_{\mathrm{T}})$, may be analyzed in different ways, as described in the Sec. 4.

5.2.2 Activation Energies

Arrhenius Analysis and Activation Energies for PMMA

The exponential dependence of the shift factors, a_{T}, on the inverse temperature (4.23) may be checked by plotting the shift factors $\log(a_{\mathrm{T}})$ versus the inverse temperature. Figure 5.21 shows this plot, referred to as the Arrhenius plot.

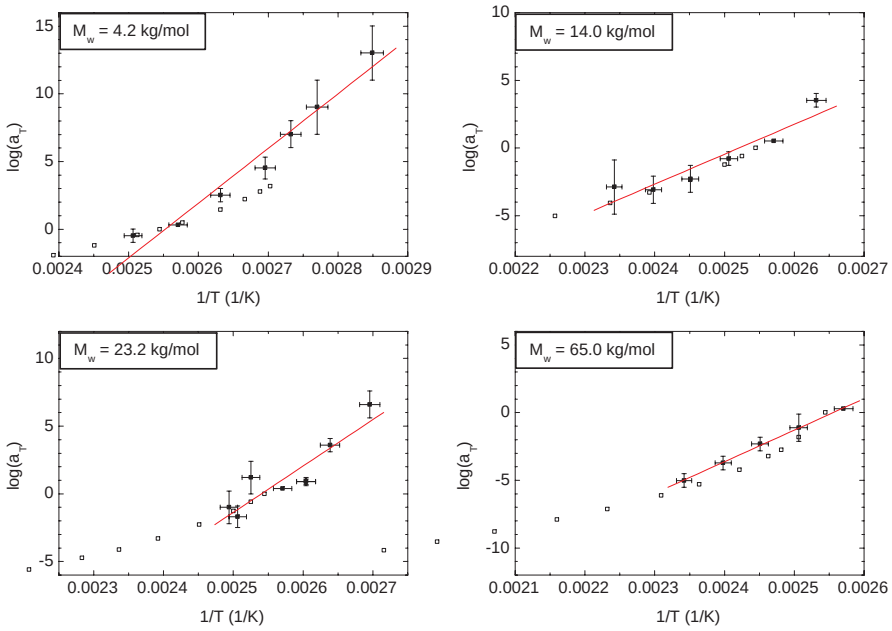

Figure 5.21: Arrhenius plots of the surface shift factors (solid squares), $\log(a_{\mathrm{T}})$, for PMMA of 4.2, 14.0, 23.2, and 65.0 kg/mol. The straight lines are best fits to the surface data, the Arrhenius law. The open squares represent the bulk values.

If the activation energy is not temperature dependent, one can extract a single activation energy for a certain relaxation process (Arrhenius behavior, Sec. 4.4). In this case the Arrhenius plot gives a straight line and the activation energy can be calculated from the slope of the best fit to the data. In other words, the shift factors have an Arrhenius-like dependence on the temperature when the Arrhenius plot is a straight line, as described in Sec. 4.4. The deviation from Arrhenius behavior is most pronounced for 4.2 kg/mol and decreases with molecular weight. PMMA with 65.0 kg/mol shows Arrhenius behavior.

However, except for 65.0 kg/mol, the shift factors in graph 5.21 do not show a clear Arrhenius-like dependence on the temperature. The curved trend of the $\log(a_{\mathrm{T}}) - \frac{1}{T}$ data rather points to a temperature-dependent activation energy. The material is rather fragile than strong.

In the bulk, linear-chain polymers, like PMMA and PS, are known to be fragile. As the Arrhenius plot for PMMA shows, this is also the case for 4.2 to 23.2 kg/mol in the first 100 nm from the surface, which these measurements probe. Apparent activation energies can be calculated for different temperatures using the equation in Fig. 4.13. To get an estimate of the magnitude of the activation energies, an average activation energy can be extracted by fitting the data with a straight line. This is done even though the dependence of the data in Fig. 5.21 deviates from the Arrhenius behavior. The obtained values for PMMA with T_{ref} =393 K are plotted against the molecular weight in Fig. 5.22 and are listed in Table 5.3.

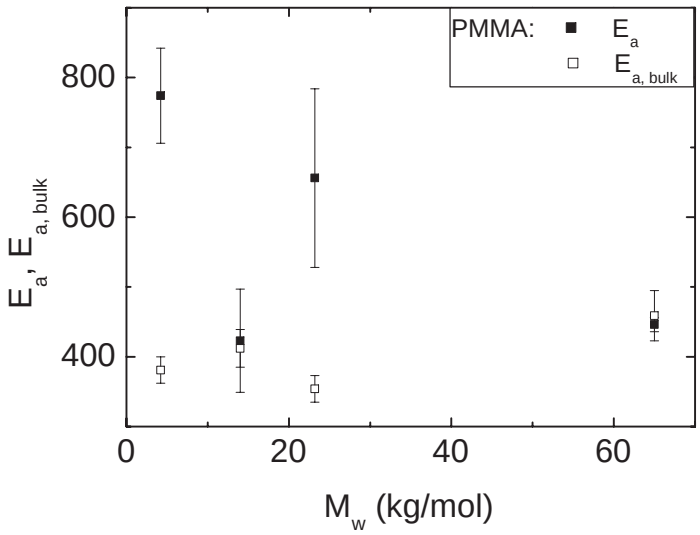

Figure 5.22: Average activation energies E_{a} of PMMA, extracted from the best fit of the Arrhenius plots (Fig. 5.21) to a line, as a function of molecular weight. The solid squares represent the values extracted from the slope of the fit to the Arrhenius law. The open circles represent the average bulk values, extracted the same way as for the surface.

M_{w}(kg/mol)	4.2	14.0	23.2	65.0
E_{a}(kJ/mol) from slope	774±68	423±74	656±128	446±10
$E_{\mathrm{a,bulk}}$(kJ/mol) from slope	381±19	412±27	354±19	459±36

Table 5.3: Average activation energies near the surface for PMMA determined from the linear fits of the Arrhenius plots in Fig. 5.21. The values E_{a} are determined from the slope. The values $E_{\mathrm{a,bulk}}$ are extracted from the slope of the bulk values in the same temperature range.

Even though a precise analysis is not possible with only four points, the near surface data can be compared to the bulk data. The average activation energies for both near surface and bulk values are extracted from the same temperature range. In the range of the errors the average activation energies for 14.0 and 65.0 kg/mol are the same for the surface and the bulk. The range of the molecular weights entanglements should occur close to M_C (M_C=2M_e, M_e=10-11 kg/mol [Mar96]). The PMMA with M_w=4.2 and 23.2 kg/mol, however, show a higher average activation energy than the one found for the bulk.

There is a discrepancy between the values of the average surface activation energy for the α relaxation processes stated here and the values for bulk measurements stated in the literature. This is not surprising since the material show rather fragile behavior, which means that the activation energy depends on the chosen temperature range. The average activation energies seem to be within the range of values quoted in the literature. Ferry [Fer80] states activation energies of E_a=259 kJ/mol for bulk polymers with a T_g=473 K and E_a=1046 kJ/mol with T_g=673 K. The bulk activation energies published by Hodge [Hod87] and Tribone *et al.* [TOG86] for a-tactic PMMA of 1147 kJ/mol and 1247 kJ/mol, respectively, are higher than the values the surface measurements revealed.

Hammerschmidt et al. [HGH99] measured an activation energy for relaxation processes at a PMMA surface of M_w=60 kg/mol with friction force microscopy. The value they found is quite small, $E_a \approx$50 kJ/mol, but they consider it to be the activation energy for the hindered rotation of the -$COOCH_3$ group. The rotation of the -$COOCH_3$ group means the activation of a β relaxation.

Smaller or larger activation energies for a certain relaxation process mean that the relaxation occurs at lower or higher temperatures, respectively. The comparison with the bulk values presents a reason to assume that the relaxation and mobility in surface confinement are reduced for 4.2 and 23.2 kg/mol.

The graph in Fig. 5.22 does not seem to show a clear dependence of the average activation energies, for the α relaxation processes, on the molecular weight. It may be that E_a depends on the molecular weight. Plotting the average activation energies, E_a, in a log-log plot versus the molecular weight would give a straight line in case of a power-law dependence.

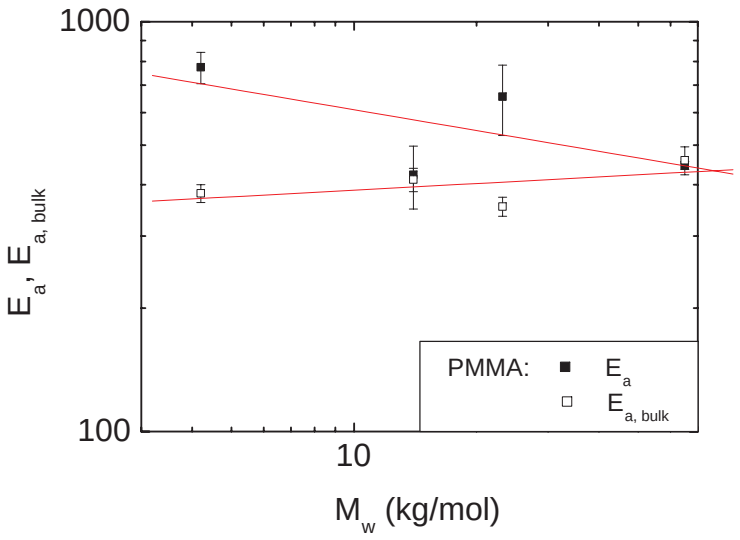

Figure 5.23: Log-log plot of the activation energies versus molecular weight for PMMA. The activation energies are extracted from the slope (black solid squares) of graph 5.21. The open circles are the corresponding bulk values. The straight lines represent the best fit to a power law.

One should be cautious about judging general dependencies of the average activation energy on the molecular weight, but if there is a power-law dependence on M_w can be estimated. Within the scope of our dynamic measurements and using the presented analysis, it might be assumed that in the molecular weight range of 4.2 to 65.0 kg/mol for the surface the power is -0.17 ± 0.14 and for the bulk 0.05 ± 0.06: $E_\mathrm{a} \propto M_\mathrm{w}^{-0.17}$ and $E_\mathrm{a,bulk} \propto M_\mathrm{w}^{0.05}$. This means the surface values slightly decrease with molecular weight, while the bulk values might slightly increase between 4.2 and 65.0 kg/mol. It has to be considered that the average activation energy depends critically on the temperature range, if the material does not show an Arrhenius-like temperature dependence.

Arrhenius Analysis and Activation Energies for PS

The average activation energies for PS are determined in the same way as for PMMA. The same molecular weight range is used. The shift factors $\log(a_\mathrm{T})$ are plotted versus the reciprocal temperature and fit by a straight line (Fig. 5.24). The reference temperature is chosen to be 373 K. A longer time for equilibration of the system, before lifting the master off the sample, is chosen in the case of PS. This may be the reason why mastering works better, but it might also cause aging of the polymer film, resulting in a slightly increased density. This could have an influence on the activation energy.

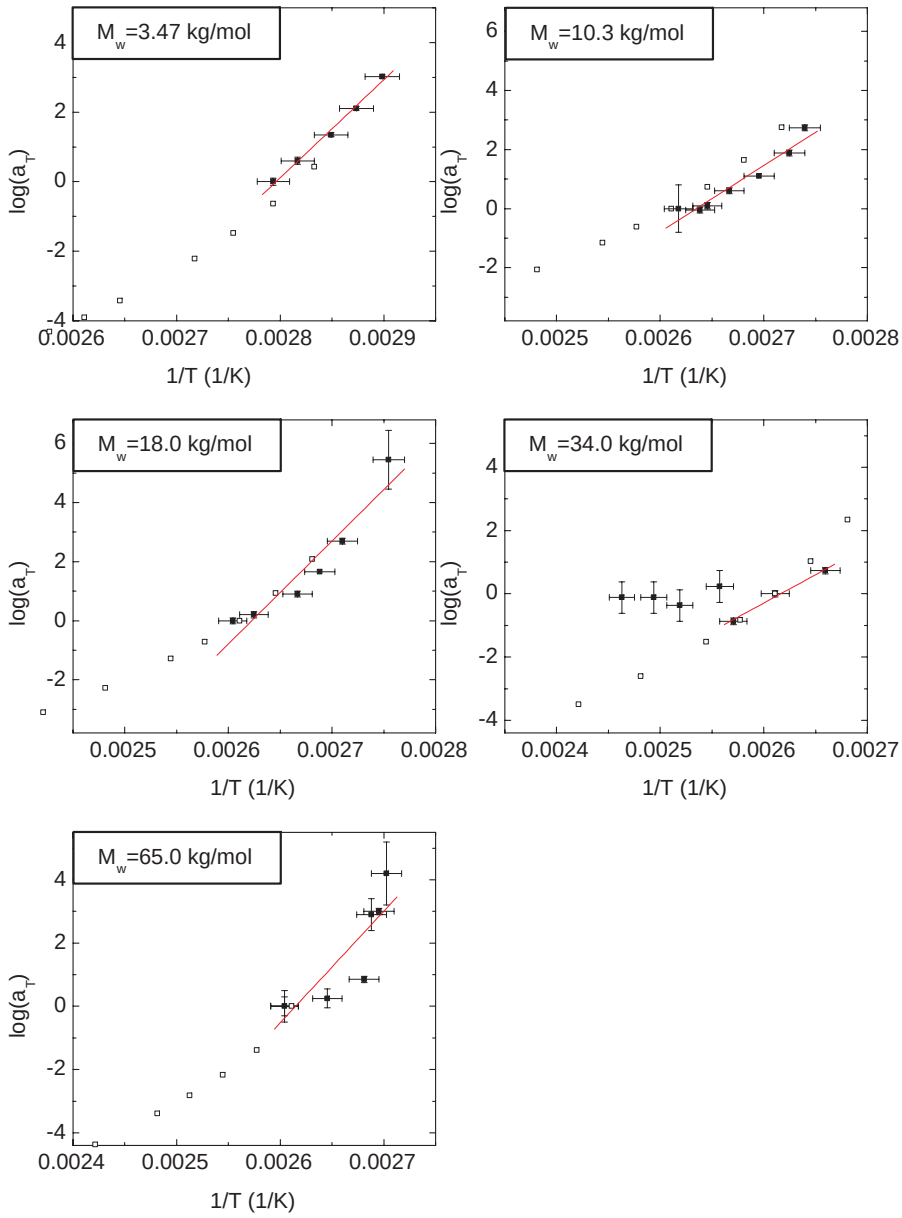

Figure 5.24: Arrhenius plots for the shift factors near the surface (solid squares), log(a_T), for PS with M_w=3.47, 10.3, 18.0, 34.0, and 65.0 kg/mol. The straight lines are linear fits to determine the average activation energy near the surface. The open squares represent the bulk data.

The average activation energy, E_a, is extracted from the slope of each Arrhenius plot (Fig. 5.24). Since the data for M_w=34.0 kg/mol do not show the same trend as for the other molecular weights and the resulting average activation energy does not seem reasonable, only the three values for the lowest temperatures are taken to determine the activation energy. The other points are considered in the error. This is the reason for the large error in the case of M_w=34.0 kg/mol.

The resulting E_{a} values for PS with M_{w} between 3.47 and 65.0 kg/mol are plotted in Fig. 5.25 and listed in Table 5.4.

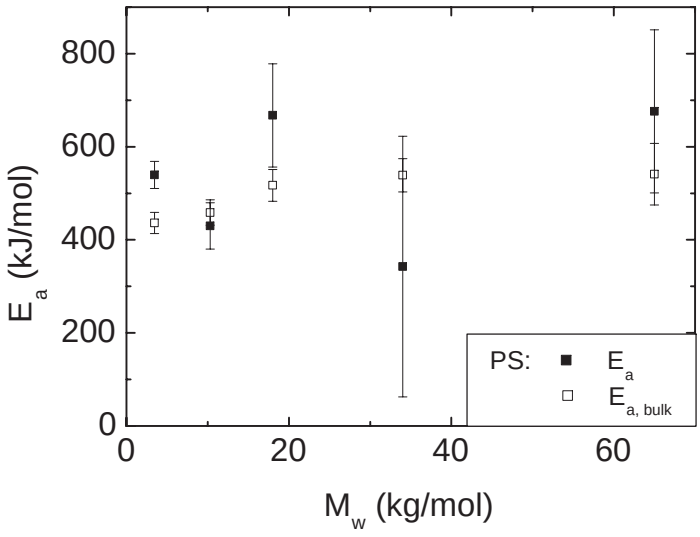

Figure 5.25: Average activation energies for PS, extracted from the linear fit of the Arrhenius plots (Fig. 5.24), as a function of molecular weight. The solid squares represent the values extracted from the slope, the open circles are the values extracted from the slope of the bulk data.

M_{w}(kg/mol)	3.47	10.3	18.0	34.0	65.0
E_{a}(kJ/mol) from slope	540 ± 29	430 ± 50	667 ± 111	343 ± 280	676 ± 175
$E_{\mathrm{a,bulk}}$(kJ/mol) from slope	436 ± 23	459 ± 27	571 ± 34	539 ± 36	54 ± 66

Table 5.4: Average Activation energies for PS determined from the linear fits of the Arrhenius plots in Fig. 5.24. The values E_{a} are determined from the slope and $E_{\mathrm{a,bulk}}$ are the corresponding bulk values.

The average activation energies for 3.47 and 18.0 kg/mol are higher than the bulk values. The other molecular weights do not show a difference to the bulk in the range of the error.

When compared with literature values, the average activation energies of PS are rather bulk- than surface-like. Bulk values for PS found in the literature are in the range of 360-880 kJ/mol [MR67], [SR98]. Surface activation energies for PS determined by Kajiyama *et al.* using lateral force microscopy are E_{a}=230$\pm$10 kJ/mol [KTST98], [TTK00], independent of molecular weight (4.9 kg/mol and 140 kg/mol).

During longer equilibration times a condensation of the polymer material may be caused

by physical aging [TSI99], but also the $T_{\mathrm{dec},0}$ values of PS do not show a difference from the bulk values between 18.0 and 65.0 kg/mol. Interpreting the average activation energy in terms of mobility at the surface, the α relaxation of PS with 3.47 and 18.0 kg/mol might happen at temperatures higher than the ones expected for the bulk. The mobility of polymers might be reduced for these molecular weights under confinement near the surface of PS.

The log-log plot of the average activation energies versus molecular weight (Fig. 5.26) does not show a specific dependence on the molecular weight.

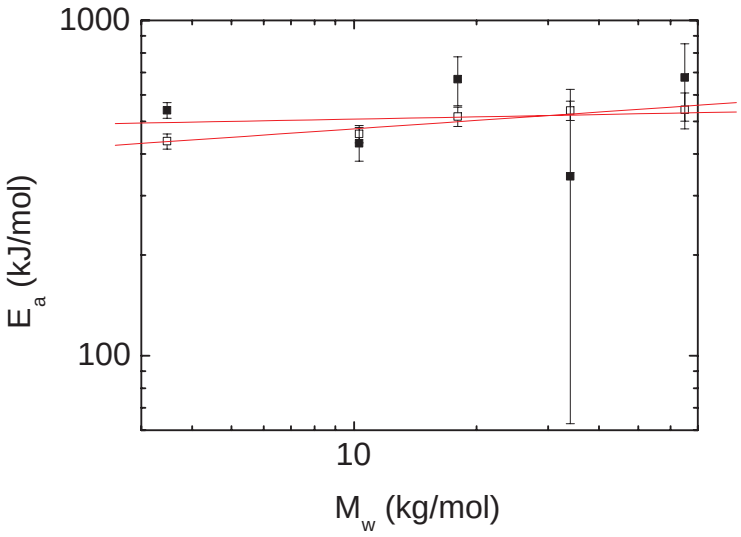

Figure 5.26: Log-log plot of the average activation energies near the surface (solid squares) versus molecular weight for PS. The average activation energies were extracted from the slope of the linear fits in Fig. 5.24. The corresponding values from the slope of the bulk values are represented by the open circles. The straight lines represent the best fits to a power law.

For a rough estimate of a possible power-law dependence of PS activation energies on M_{w}, linear fits to the data in Fig. 5.26 are performed. The scatter of the E_{a}, however, is much larger than for PMMA. If there is any power law dependence, the power for the molecular weight range between 3.47 and 65 kg/mol near the surface is 0.02 ± 0.14 and for the bulk 0.08 ± 0.02: $E_{\mathrm{a}} \propto M_{\mathrm{w}}^{0.02}$ and $E_{\mathrm{a,bulk}} \propto M_{\mathrm{w}}^{0.08}$. There is no difference between the bulk and near the surface within the error.

5.2.3 Determination of Fragility

Due to the Arrhenius analysis in the previous section, it is known that the linear polymers in the range of the probing depth (first 100 nm from the surface) do not show Arrhenius-like behavior, except for PMMA with M_{w}=65.0 kg/mol and maybe the lowest molecular weight samples of PS. The deviation from Arrhenius-like behavior, referred to as fragility, is often analyzed graphically by presenting the data in an Angell plot (see Sec. 4.5).

Angell Analysis for PMMA

The Angell presentation of the shift factors makes it possible to draw conclusions about the fragility. The Angell plots of the near-surface shift factors are scaled with the near-surface $T_{\mathrm{dec},0}$ determined in Sec. 5.1.1, instead of the bulk T_{g}. These plots for PMMA are presented in Fig. 5.27.

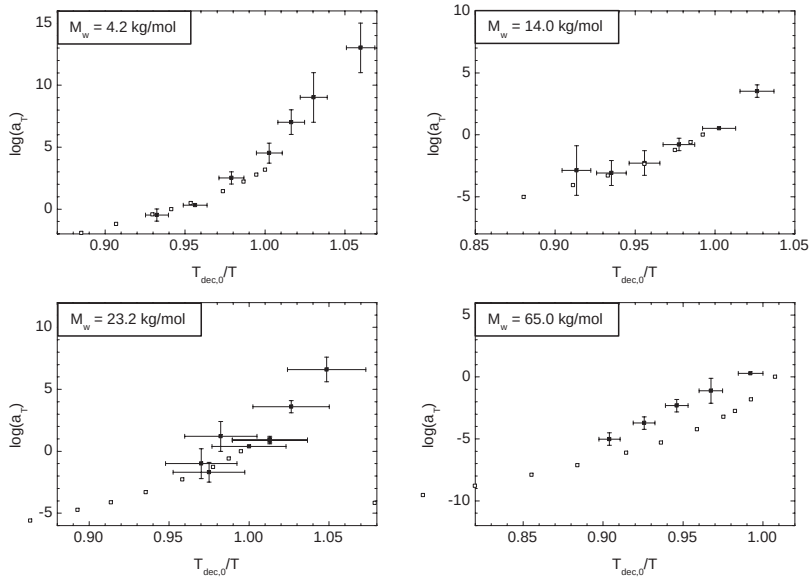

Figure 5.27: Angell presentation of the PMMA shift factors determined from the mastering in Sec. 5.2.1. The more the trend of the data deviates from linear, the higher is the fragility. A measure of the fragility is the slope at T_{g}. For the surface data (solid squares), the fragility is the slope at $T_{\mathrm{dec},0}$, where $\frac{T_{\mathrm{dec},0}}{T} = 1$. The corresponding $\log(a_{\mathrm{T}})$ - $\frac{T_{\mathrm{g}}}{T}$ data for the bulk are represented by the open squares.

One measure for the fragility of the polymer is the slope of the Angell plot. In the near-surface measurements it is the slope at $T_{\mathrm{dec},0}$, or $\frac{T_{\mathrm{dec},0}}{T} = 1$. The determination of the slope at $T_{\mathrm{dec},0}$ is subjective and not so precise since the number of data points is small and the statis-

tical deviation of the slope is quite large. However, it is possible to get an impression about the changes in fragility. For the measured range of PMMA molecular weights we might infer from the Angell plots that the fragility decreases with increasing molecular weight. There is a pronounced difference in surface and bulk fragility for 65.0 kg/mol.

Angell Analysis for PS

The same as for the PMMA shift factors, the data for PS are plotted in Angell plots in Fig. 5.28.

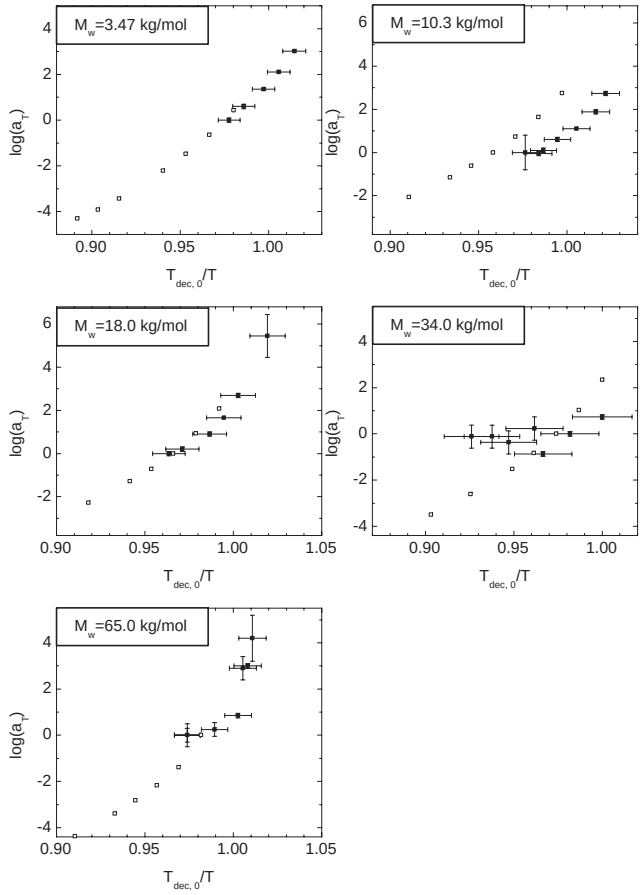

Figure 5.28: Angell presentation of the PS shift factors determined from the mastering in Sec. 5.2.1. The more the trend of the data deviates from linear, the higher is the fragility. A measure for the fragility is the slope at T_g. For the surface data (solid squares), the fragility is the slope at $\frac{T_{dec,0}}{T} = 1$. The open squares represent the bulk data.

Again, the slope at $\frac{T_{dec,0}}{T} = 1$ is a measure for the fragility. For PS, there is not such an obvious trend as for PMMA. From the Angell plot (Fig. 5.28), it may be assumed that the fragility is the smallest for PS of M_w=34.0 kg/mol.

A precise conclusion cannot be drawn from the Angell plots. A better way to analyze the data is to fit it to the KWW equation (4.34), VF equation (4.29), or WLF equation (4.31). The next section covers the analysis of the shift data by means of the WLF equation.

WLF Analysis for PMMA

The different ways to analyze the $\log(a_{\mathrm{T}})$ data with respect to the fragility are described in Sec. 4.5. Analyzing the $\log(a_{\mathrm{T}})$ data using the WLF equation gives a more quantitative result for the fragility than the Angell plot. The WLF method is chosen since it is also possible to determine T_{inf} and make assumptions about free volume and expansion coefficients.
In the theory chapter (Sec. 4.6) it was mentioned that it is more accurate to extract the WLF-values, c_1 and c_2, from the linear extrapolation of the $\frac{(T-T_{\mathrm{ref}})}{log(a_{\mathrm{T}})}$ versus $T - T_{\mathrm{ref}}$ plot. This plot is presented in Fig. 5.29.

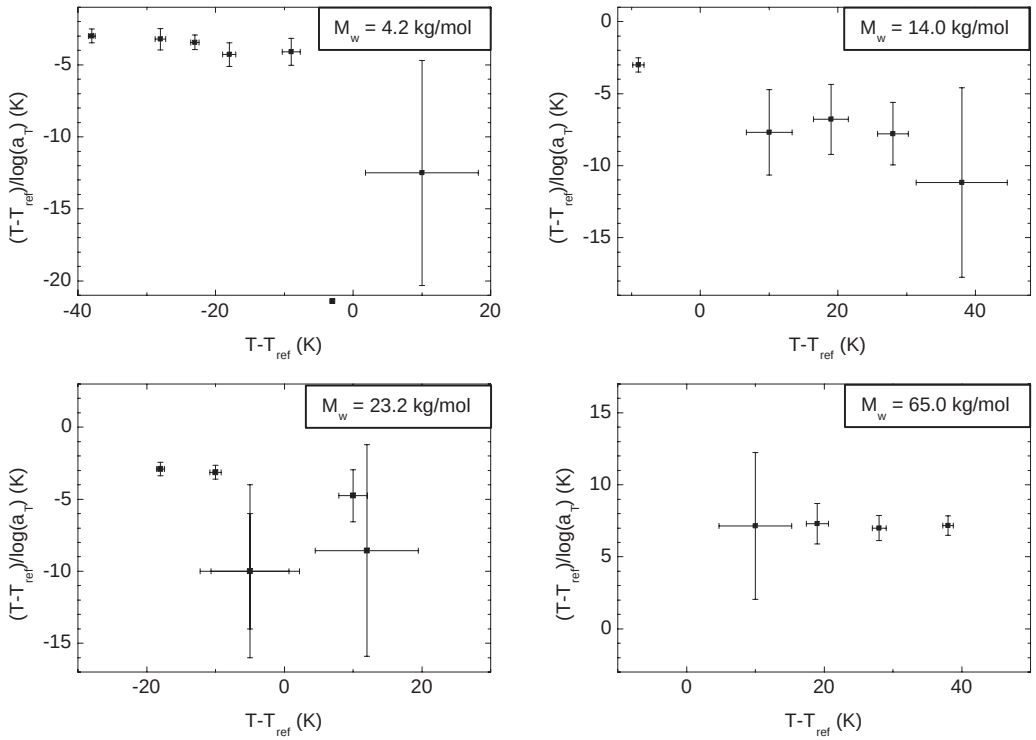

Figure 5.29: $\frac{(T-T_{\mathrm{ref}})}{log(a_{\mathrm{T}})}$ versus $(T - T_{\mathrm{ref}})$ data (solid squares) of PMMA of 4.2, 14.0, 23.2, and 65.0 kg/mol.

The ratio $\frac{(T-T_{\mathrm{ref}})}{log(a_{\mathrm{T}})}$ diverges for values close to the reference temperature and the errors are quite large. Using several different reference temperatures to optimize the fits would improve the results. However, we prefer to perform fits to the $\log(a_{\mathrm{T}})$ versus T graphs. The number of

data points is quite small and thus the accuracy is reduced.

The shift factors versus temperature are fit to equation (4.31). The data and the best fits (solid lines) are shown in Fig. 5.30. The trend of the bulk shift factors, determined by T. Pakula from bulk rheology measurements, is indicated by the dashed lines. With equation (4.39) the bulk values were converted to the same T_{ref} as used for the surface.

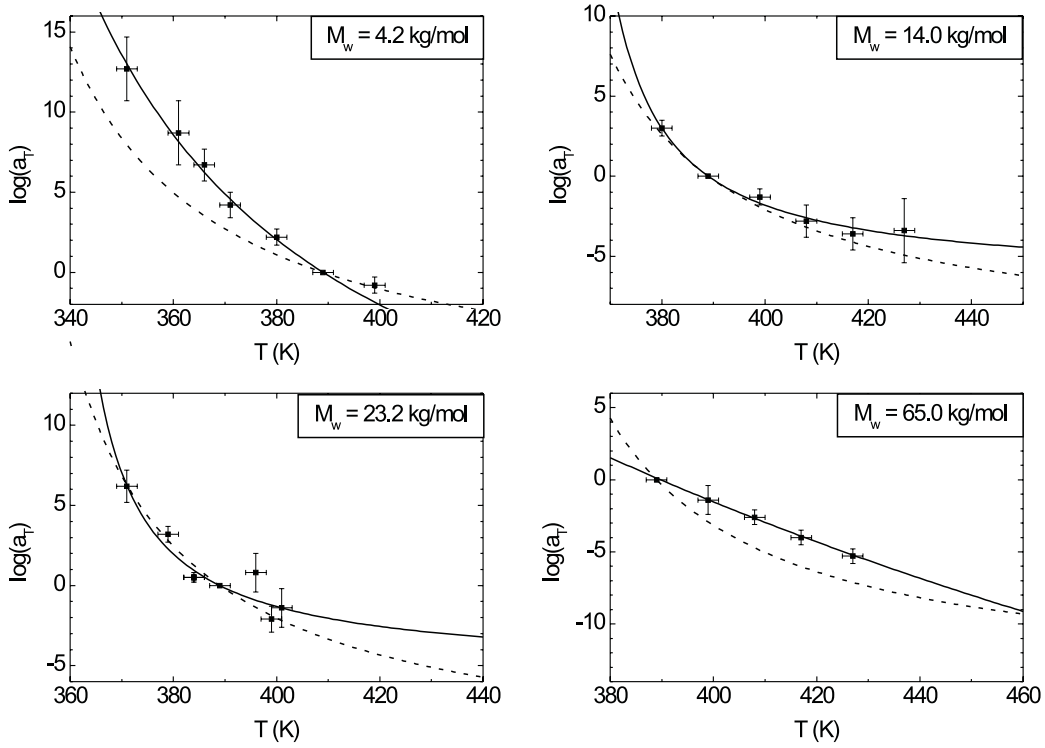

Figure 5.30: The shift factors determined from the mastering of the PMMA data in Sec. 5.2.1 are plotted versus the respective temperatures. The solid lines are the best fits to the WLF equation near the surface and the dashed lines indicate the trend of the bulk shift factors determined by T. Pakula with a bulk rheometer.

The c_1 and c_2 values are extracted from the best fits to the WLF equation. A forced fit, as suggested by Angell [Ang97], did not give reasonable results. The forced fit fixes c_1 at T_{g} to the value $c_1^g = 16 \pm 2$ so that the relaxation time at T_{g} is $\tau_{\mathrm{Tg}} = 100\ s$. Expressing $\tau_{\mathrm{Tg}} = 100\ s$ in phonon relaxation times, $\tau_{\mathrm{phonon}} = 10^{-14}\ s$, the value for c_1 should be around 16 at T_{g}. If the reference temperature is not equal to T_{g} the forced fit might give unreasonable results or even fail. The results from a normal fit to the WLF equation are plotted versus the molecular weight in Fig. 5.31. To be able to compare the surface values with the ones for the bulk, the latter are added to the graph.

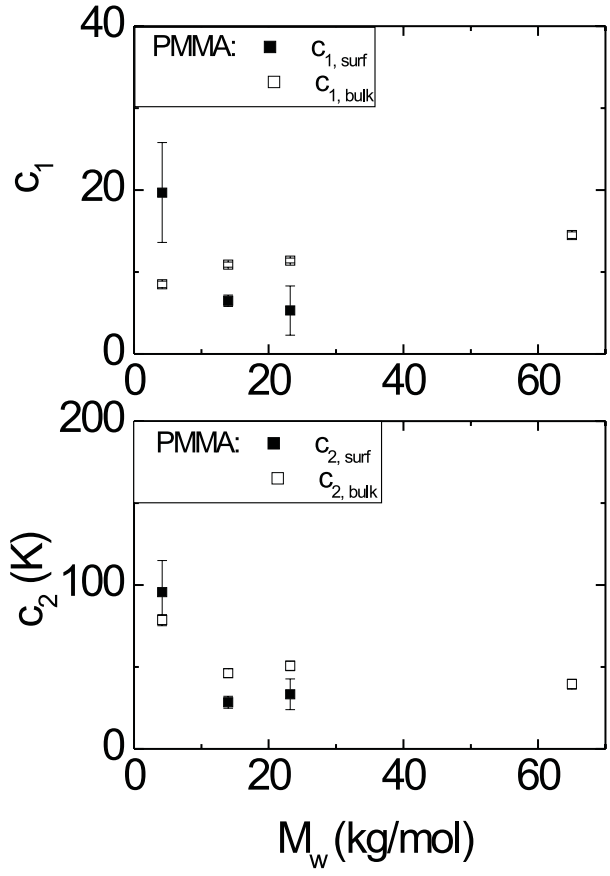

Figure 5.31: WLF parameters resulting from fitting the surface shift factors (solid squares) and the bulk shift factors (open square) to the WLF equation (4.31). The values for the Arrhenius-like PMMA with 65.0 kg/mol could not be determined since the WLF-fit of the strong material failed. The reference temperature for the PMMA measurements is 389 K.

Interpreting Fig. 5.31, the upper graph shows that the surface relaxation times decrease with molecular weight between 4.2 and 23.2 kg/mol while the bulk values are increasing. The c_1 value for 4.2 kg/mol is higher than in the bulk, the ones for 14.0 and 23.2 are lower than the bulk values. The WLF temperatures c_2 are the same for 4.2 and 23.2 kg/mol near the surface and in the bulk, for 14.0 kg/mol the surface value is slightly lower.

T_{inf} may be obtained from the WLF parameter c_2 and a reference temperature T_{ref} close to T_{g}; $T_{\mathrm{inf}} = T_{\mathrm{ref}} - c_2$. The Kauzmann temperature [Kau48] is assumed to be close to T_{inf}, $T_{\mathrm{K}} \approx T_{\mathrm{inf}}$, as stated in Sec. 4.6 of the theory chapter. Consequently, T_{inf} and thus also T_{K} can be determined from c_2 and T_{ref}. T_{inf} as a function of molecular weight between 4.2 kg/mol and 65.0 kg/mol is depicted in Fig. 5.32.

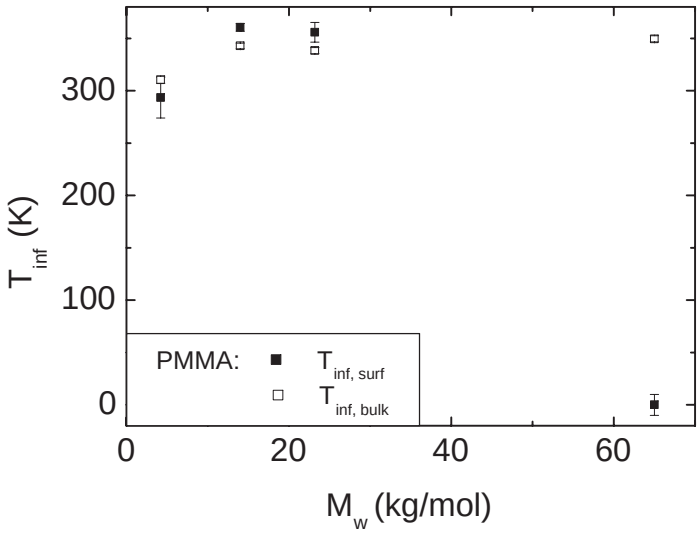

Figure 5.32: $T_{\rm inf}$ determined from the WLF temperature c_2 and $T_{\rm ref}$ is plotted versus molecular weight. The solid squares represent the values $T_{\rm inf}$ for the surface, the open squares show the values for the bulk.

$M_{\rm w}$(kg/mol)	4.2	14.0	23.2	65.0
$c_{1,\rm surf}$	19.7±6.1	6.5±0.7	5.3±3	59.8±1.2
$c_{2,\rm surf}$(K)	95.6±19.4	28.5±3.7	33.3±9.4	389.0±10.0
$T_{\rm inf,surf}$(K)	293.4±19.4	360.5±3.7	355.7±9.4	0.0±10.0
$c_{1,\rm bulk}$	8.5±0.4	10.9±0.3	11.4±0.3	14.5±0.4
$c_{2,\rm bulk}$(K)	78.6±3.4	46.2±2.7	50.7±2.9	39.5±3.0
$T_{\rm inf,bulk}$(K)	310.4±3.4	342.8±2.7	338.3±2.9	349.5±3.0

Table 5.5: c_1 and c_2 determined by fitting both the surface data from dynamic measurements ($T_{\rm ref}$ indicated in Fig. 5.17) and the bulk data from bulk rheology experiments [PH] ($T_{\rm ref}$=393K) to the WLF equation (4.31). The $T_{\rm inf}$ are calculated from the c_2 values, for the surface and the bulk, using equation (4.32).

In Table 5.5, the WLF parameters and the $T_{\rm inf}$ for PMMA are listed; there are both surface and bulk values. The $T_{\rm inf}$ values near the surface are close to the bulk values. $T_{\rm inf}$ near the surface are higher than the bulk values for 14.0 and 23.2 kg/mol. The strong behavior of 65.0 kg/mol is represented by $T_{\rm inf}$=0. Another reference bulk value is the Kauzmann temperature for atactic PMMA of 335 K from [OBK82]. Assuming that the Kauzmann temperature and $T_{\rm inf}$ are very close, this confirms the bulk values.

As Angell [Ang97] reasoned c_1^g should be 16 ± 2, if there is no additional phenomena.

Since the c_1 values for the surface and the bulk differ from 16 ± 2, it might be assumed that this difference results from a T_{ref} higher or lower than the actual T_{g}. In the case of a T_{ref} higher than T_{g} the c_1 values would be smaller than 16 and vice versa. Using the equations (4.39) and setting the new c_1^g value to 16, a $T_{\mathrm{g}}(c_1 = 16)$ can be calculated from the WLF parameters of the dynamic measurements: $T_{\mathrm{ref}}^g = T_{\mathrm{g}}(c_1 = 16) = c_2^g + T_{\mathrm{inf}}$. These calculations were performed for the surface and the bulk values of the varying molecular weights. Figure 5.33 shows the $T_{\mathrm{g,surf}}(c_1 = 16)$ in comparison with the bulk values $T_{\mathrm{g,bulk}}(c_1 = 16)$ versus molecular weight in the upper plot. Both were calculated from the WLF parameters. The lower plot shows the comparison of the $T_{\mathrm{dec},0}$ values with the $T_{\mathrm{g,bulk}}$ from Sec.5.1.

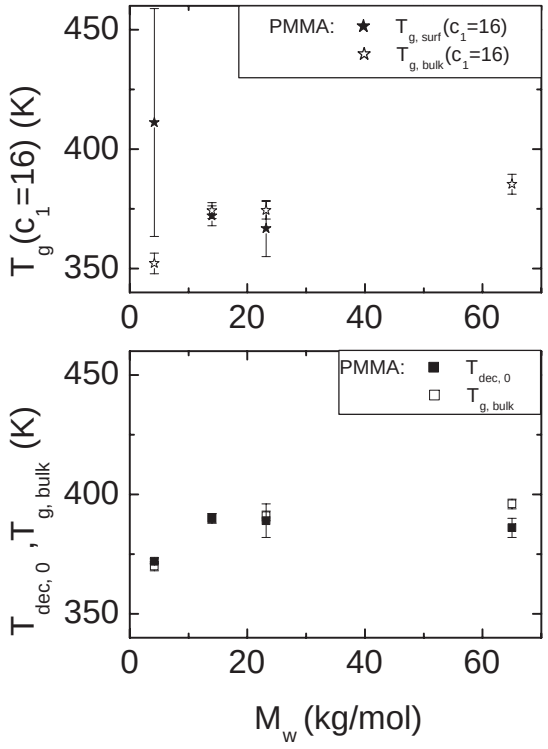

Figure 5.33: The upper plot shows the $T_{\mathrm{g,surf}}(c_1 = 16)$ values (solid stars) in comparison with the $T_{\mathrm{g,bulk}}(c_1 = 16)$ values (open stars) versus molecular weight. $T_{\mathrm{g,surf}}(c_1 = 16)$ and $T_{\mathrm{g,bulk}}(c_1 = 16)$ were calculated (with equations (4.39)) from the WLF parameters listed in Table 5.5 assuming c_1^g is 16±2.The lower plot represents the $T_{\mathrm{dec},0}$ values from Sec. 5.1 (solid square)and the $T_{\mathrm{g,bulk}}$ values from the DSC measurements (open squares).

Except for the surface value of PMMA with 4.2 kg/mol, the glass temperatures calculated from the WLF-parameters, assuming c_1=16±2, are lower than the values measured in Sec. 5.1 both near the surface and in the bulk. As found for $T_{\mathrm{dec},0}$ and $T_{\mathrm{g,bulk}}$ from Sec. 5.1,

there is no difference between $T_{\mathrm{g,surf}}(c_1 = 16)$ and the $T_{\mathrm{g,bulk}}(c_1 = 16)$ value for 14.0 and 23.2 kg/mol. The $T_{\mathrm{g,surf}}(c_1 = 16)$ for 4.2 kg/mol was larger near the surface than in the bulk and the $T_{\mathrm{g,surf}}(c_1 = 16)$ for 65.0 kg/mol could not be determined this way, since the material behaved strong.

The T_{g} values from the near surface and bulk measurements ($T_{\mathrm{dec,0}}$ and $T_{\mathrm{g,bulk}}$ from static T-ramp and DSC measurements, as well as $T_{\mathrm{g,surf}}(c_1 = 16)$ and $T_{\mathrm{g,bulk}}(c_1 = 16)$ from dynamic measurements, assuming c_1=16±2) were used to determine the fragility. The fragility is defined as the ratio $T_{\mathrm{inf}}/T_{\mathrm{g}}$ (see Sec. 4.5). Thus, the ratios $F_{\mathrm{surf}} = \frac{T_{\mathrm{inf,surf}}}{T_{\mathrm{dec,0}}}$ and $F_{\mathrm{bulk}} = \frac{T_{\mathrm{inf,bulk}}}{T_{\mathrm{g,bulk}}}$ express the fragilities near the surface and in the bulk, respectively. The fragilities calculated, assuming c_1=16±2, are $F_{\mathrm{surf}}(c_1 = 16)$ and $F_{\mathrm{bulk}}(c_1 = 16)$. The temperatures in these ratios need to be absolute temperatures; *i.e.*, they must be expressed in Kelvin. The resulting dependence of the PMMA fragilities upon the molecular weight is plotted in Fig. 5.34.

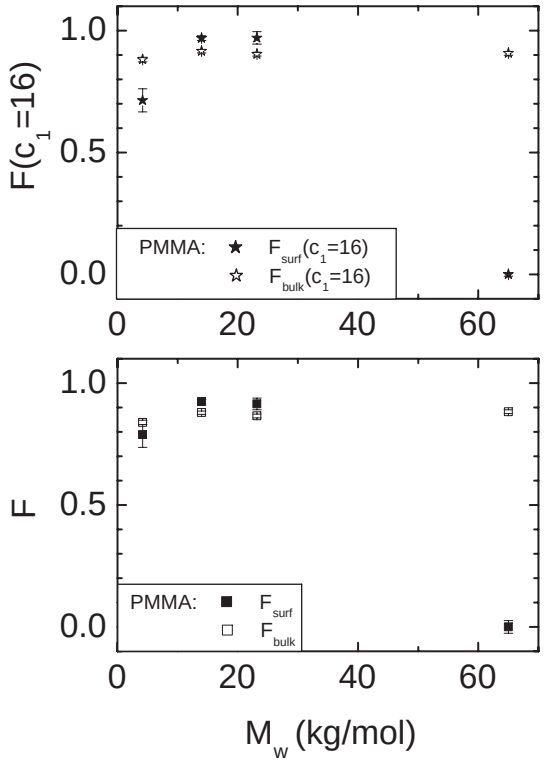

Figure 5.34: Top: Fragilities calculated from the $T_{\mathrm{g,surf}}(c_1 = 16)$ and $T_{\mathrm{g,bulk}}(c_1 = 16)$ values, assuming c_1=16±2 (solid stars - near the surface; open stars - bulk). Bottom: Fragilities determined from the T_{inf}'s listed in Table 5.5 and the corresponding $T_{\mathrm{dec,0}}$ and $T_{\mathrm{g,bulk}}$ from Table 5.1 versus molecular weight (solid squares represent the surface values, the open squares the bulk values).

The fragility is a value between 0 and 1. If a material has a fragility of 1, this means that T_{inf} (defining the state of minimum configurational entropy) and the glass temperature are the same. In this case, the material responds drastically to temperature changes close to T_{g}. The more the fragility approaches 0, the less fragile is the system and the more the system's properties follow the inverse temperature. If the value is close to 0, the difference between T_{inf} and T_{g} is large and the shift factors for the material behave Arrhenius-like. Materials with very small fragility values are called strong; materials with F close to 1 are called fragile (see Sec. 4.5). The bulk fragility does not seem to change much with molecular weight (F≈0.88) only the value for M_{w}=4.2 kg/mol appears to be smaller, thus stronger. The situation is different for the surface. The comparison of the fragilities determined from the quasi-static and dynamic measurements and the bulk values, gives a very similar result. For the smallest molecular weights (4.2 kg/mol), the fragility near the surface is smaller than in the bulk. The surface for 14.0 and 23.2 kg/mol are higher than the bulk ones. The strong near surface behavior of 65.0 kg/mol is represented by a fragility close to 0, again much smaller than in the bulk.

WLF Analysis for PS

Now, the question arises whether the fragility of PS also decreases with increasing molecular weight. To find the fragility for PS, the same analysis as that for PMMA is performed.

The linear extrapolation of the $\frac{(T-T_{\mathrm{ref}})}{log(a_{\mathrm{T}})}$ versus $T - T_{\mathrm{ref}}$ graph is shown here, but it is not analyzed in more detail for the same reasons as mentioned in the previous section. Figure 5.35 displays the linear extrapolation of the WLF data from the PS samples.

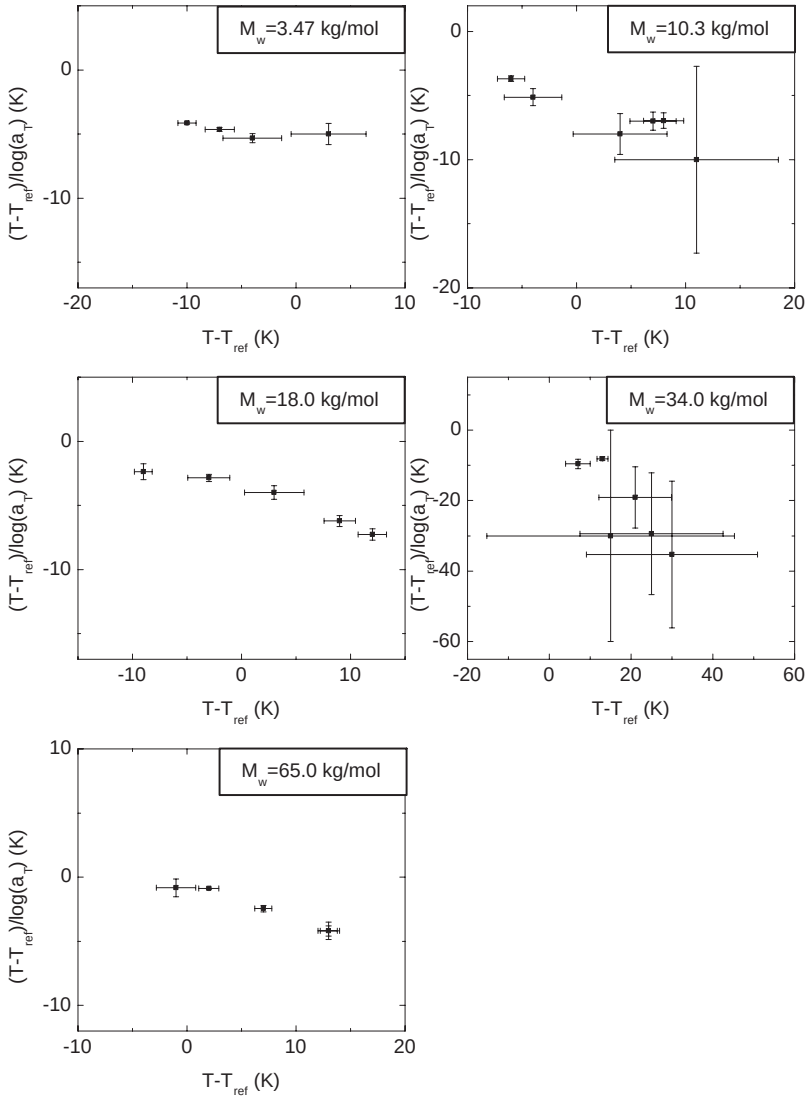

Figure 5.35: $\frac{(T-T_{\mathrm{ref}})}{log(a_{\mathrm{T}})}$ versus $(T - T_{\mathrm{ref}})$ data (solid squares) for PS of 3.47, 10.3, 18.0, 34.0, and 65.0 kg/mol.

For PS, the WLF plot is again given priority over the linearized version. The shift factors are plotted versus T and fit to the WLF equation in Fig. 5.36. The fits of the bulk shift factors (converted to the same T_{ref} as for the surface value with equation (4.39)) are added to the plots for each molecular weight.

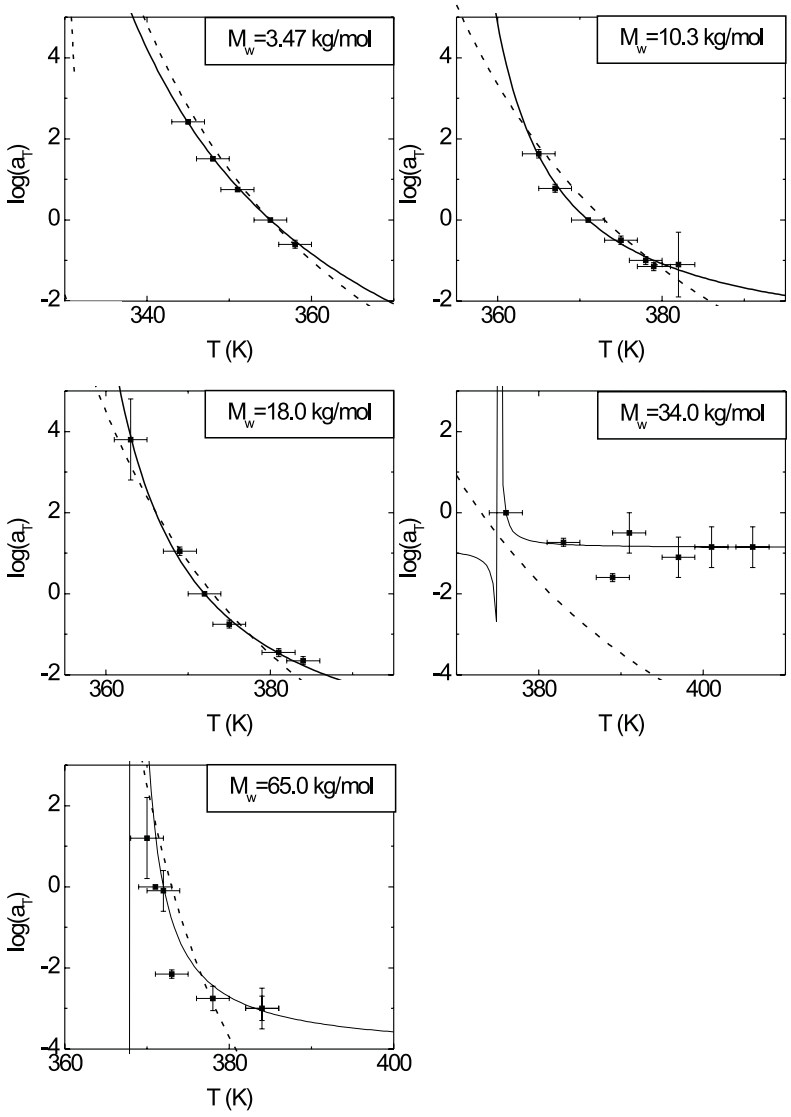

Figure 5.36: The shift factors determined from the mastering of the PS data in section 5.2.1 are plotted versus the respective temperatures. The solid lines are the best fit to the WLF equation and the dashed lines indicate the bulk shift factors determined by T. Pakula with a bulk rheometer.

The c_1 and c_2 values resulting from the best fits of the surface and bulk shift factors to the WLF equation are presented in Fig. 5.37. Except for PS of 3.47 kg/mol, c_1 and c_2 are smaller near the surface than in the bulk. The deviation of the c_1 values for PS from $c_1^g = 16 \pm 2$ might be caused by the choice of the reference temperature. c_1 deviates from 16±2 if the reference temperature does not coincide with T_g, as discussed in more detail for PMMA.

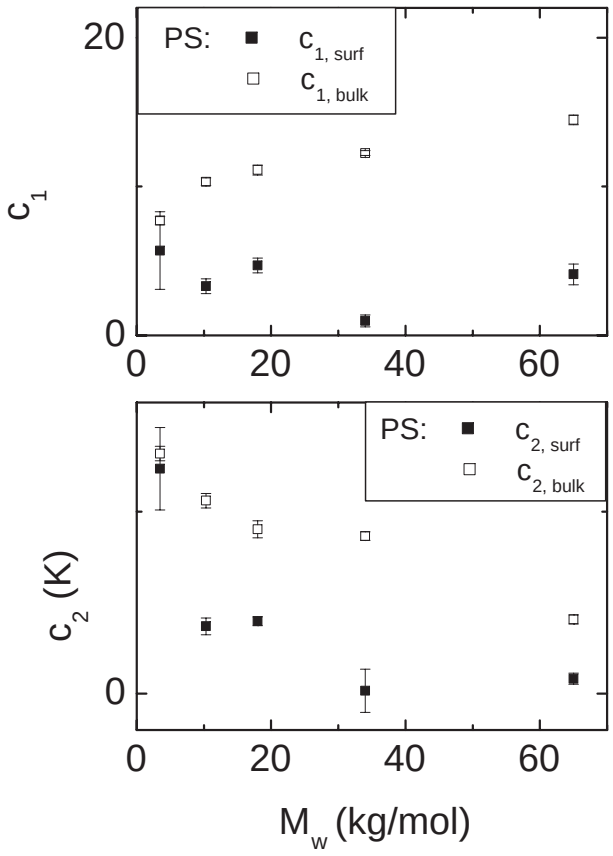

Figure 5.37: WLF parameters resulting from fitting the surface shift factors (solid squares) and the bulk shift factors (open square) to the WLF equation (4.31). T_{ref} for the PS measurements was 373 K.

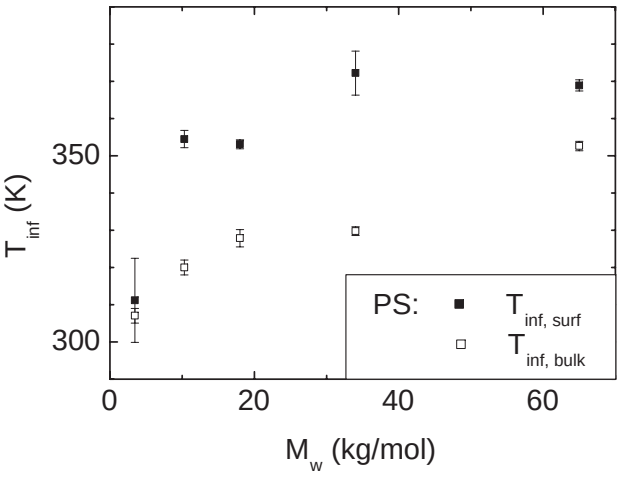

Figure 5.38: The Vogel–Fulcher temperatures, T_{inf}, determined from the WLF temperature c_2 and T_{ref} (equation (4.40)), are plotted versus molecular weight. The solid squares represent the values T_{inf} for the surface; the open squares are the values for the bulk.

M_w(kg/mol)	3.47	10.3	18.0	34.0	65.0
$c_{1,\mathrm{surf}}$	5.7±2.6	3.3±0.5	4.7±0.5	1.0±0.4	4.1±0.7
$c_{2,\mathrm{surf}}$(K)	61.8±11.3	18.5±2.3	19.9±1.2	0.8±5.9	4.1±1.5
$T_{\mathrm{inf,surf}}$(K)	311.2±11.3	354.5±2.3	353.1±1.2	372.2±5.9	368.9±1.5
$c_{1,\mathrm{bulk}}$	7.7±0.3	10.3±0.3	11.1±0.3	12.3±0.2	14.5±0.3
$c_{2,\mathrm{bulk}}$(K)	66.0±2.0	53.0±2.0	45.1±2.3	43.3±1.2	20.4±1.3
$T_{\mathrm{inf,bulk}}$(K)	307.0±2.0	320.0±2.0	327.9±2.3	329.8±1.2	352.6±1.3

Table 5.6: c_1 and c_2 determined by fitting both the surface data (T_{ref} as indicated in Fig. 5.19) from dynamic measurements and the bulk data from bulk rheology experiments [PH] (T_{ref}=373 K) to the WLF equation (4.31). The T_{inf}'s are calculated from the c_2 values for the surface and the bulk using equation (4.32).

T_{inf}, the Vogel temperature should be close to the Kauzmann temperatures. The T_{inf}'s for each molecular weight are calculated from the c_2 values and the reference temperature using equation (4.32). The trend of T_{inf} with molecular weight is presented in Fig. 5.38. Fig. 5.38 shows higher T_{inf} near the surface for PS of all molecular weights but 3.47 kg/mol where surface and bulk values are the same.

The surface and bulk values of c_1, c_2 and the T_{inf} for PS are listed in Table 5.6. The reference temperatures for the near-surface values are indicated in Fig. 5.19, the reference temperature for the bulk values is 373 K.

Again, as it was performed for PMMA, the $T_{\mathrm{g,surf}}(c_1 = 16)$ and $T_{\mathrm{g,bulk}}(c_1 = 16)$ values can be calculated using equations (4.39). Figure 5.39 shows two plots. The molecular weight dependence of $T_{\mathrm{g,surf}}(c_1 = 16)$ and $T_{\mathrm{g,bulk}}(c_1 = 16)$ calculated from the WLF parameters in dependence on molecular weight is depicted in the top plot. $T_{\mathrm{dec},0}$, determined with T-ramps and $T_{\mathrm{g,bulk}}$ values from DSC (Sec.5.1) are shown in the bottom plot.

The glass temperatures determined by the dynamic measurements are slightly lower than the quasi-static ones from Sec. 5.1. The dependence on the molecular weight of the two different data sets (from decay and T-ramp experiments) is very similar and for both data sets there is no difference between near surface an bulk values with one exception. The exception is 34.0kg/mol for the dynamic, 3.47 and 10.3 kg/mol for the quasi-static results.

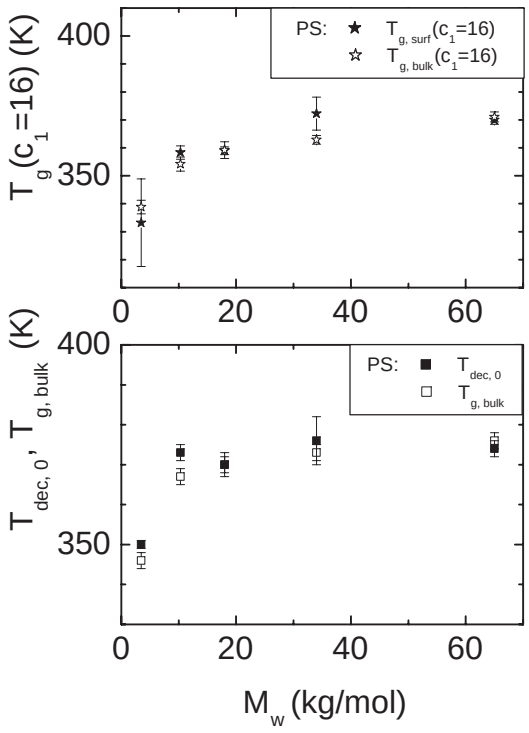

Figure 5.39: The top plot shows the $T_{\mathrm{g,surf}}(c_1 = 16)$ (solid stars) and $T_{\mathrm{g,bulk}}(c_1 = 16)$ (open stars) calculated from the WLF parameters (see Table 5.6) in dependence on molecular weight. The $T_{\mathrm{dec},0}$ (solid square), measured with the quasi-static temperature ramps and the $T_{\mathrm{g,bulk}}$ (open squares) from the DSC measurements (Sec. 5.1) are plotted in the bottom graph.

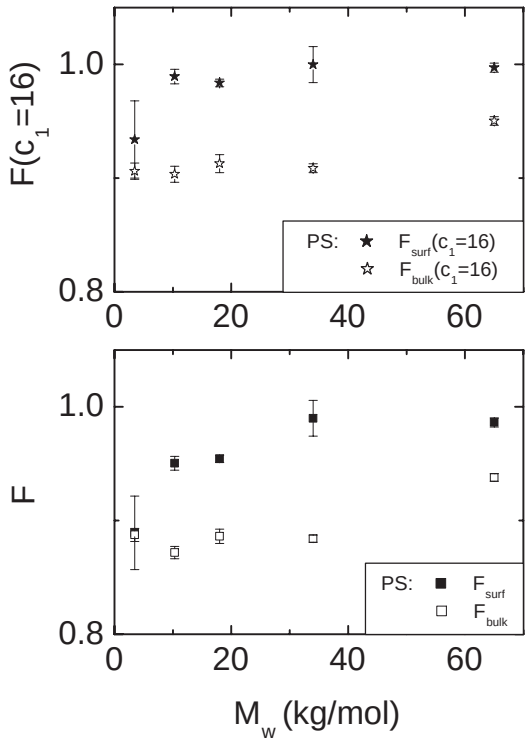

Figure 5.40: The fragilities calculated from the T_{inf}'s listed in Table 5.5 and the corresponding glass temperatures for the surface and the bulk ($T_{\mathrm{dec},0}$ and $T_{\mathrm{g,bulk}}$ from Table 5.2) are plotted versus molecular weight. The fragilities for the surface are represented by the solid stars and squares; the open stars and squares represent the bulk values.

The fragilities for PS are also values between 0 and 1. Except for PS with 3.47 kg/mol the fragility is higher near the surface than in the bulk. This is true for both the comparison of $F_{\mathrm{surf}}(c_1 = 16)$ and $F_{\mathrm{bulk}}(c_1 = 16)$ and of the fragilities determined from $T_{\mathrm{dec},0}$ and $T_{\mathrm{g,bulk}}$.

5.2.4 Free Volume and Expansion Coefficients

Free Volume Fraction and Expansion Coefficients for PMMA

We may speculate about the molecular-weight dependence of both the free volume and the expansion coefficient. How the values of c_1 and c_2 behave with respect to the free volume and the thermal expansion is described in Sec. 4.6. $\frac{1}{c_1}$ is proportional to the free-volume fraction f, and the ratio $\frac{1}{c_1 c_2}$ is proportional to the expansion coefficient α. Plotting $\frac{1}{c_1}$ ($\propto f$) and $\frac{1}{c_1 c_2}$ ($\propto \alpha$) versus molecular weight at a reference temperature T_{ref} may give some insight into the behavior of the free-volume fraction and the thermal expansion at T_{ref}. The molecular-weight dependence of f and α is presented in Fig. 5.41. The error bars for the ratio are determined with error propagation and they show that the possible variations of the values are quite large.

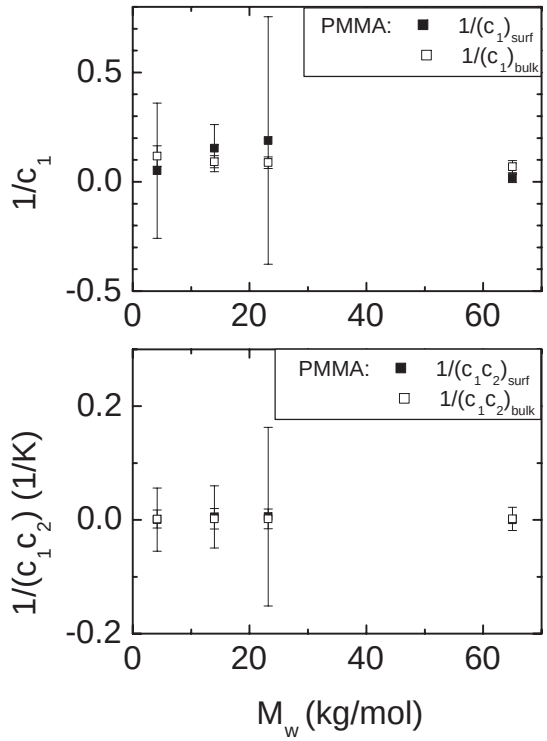

Figure 5.41: $\frac{1}{c_1}$ and $\frac{1}{c_1 c_2}$ for the surface (solid squares) and the bulk (open squares), determined from the best fits of the shift factors of PMMA to the WLF equation (Fig. 5.30), versus the molecular weight.

The experimental results reveal that near the surface and the bulk free-volume fraction are the same within the error of the measurements. In the range of molecular weights investigated in the experiments with PMMA, the expansion coefficients also do not show a difference between the near surface region and the bulk.

Free-Volume Fraction and Expansion Coefficients for PS

To find out whether the side group of the polymer has an influence on the free-volume fraction and the expansion coefficient, the same analysis is done for PS. The ratios $\frac{1}{c_1}$ ($\propto f$) and $\frac{1}{c_1 c_2}$ ($\propto \alpha$) for PS are presented in Fig. 5.42.

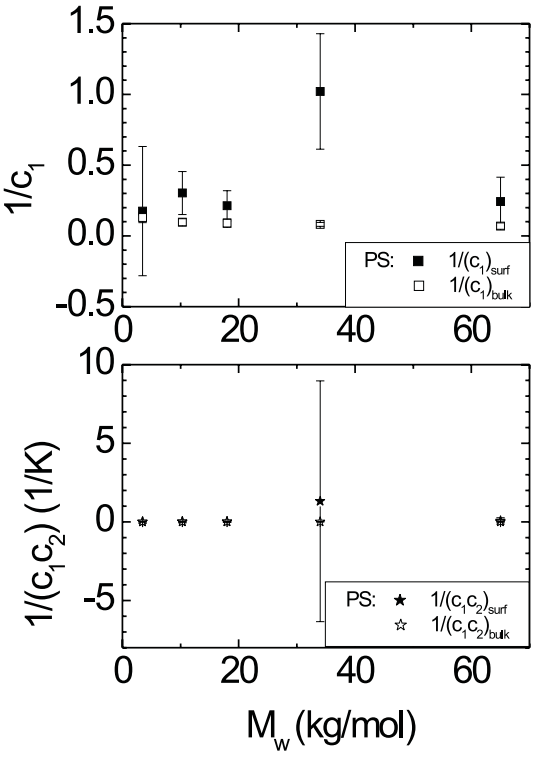

Figure 5.42: $\frac{1}{c_1}$ and $\frac{1}{c_1 c_2}$ for the surface (solid squares) and the bulk (open squares), determined from the best fit of the shift factors for PS to the WLF equation (Fig. 5.36), versus the molecular weight.

For PS, the trend of the free volume fraction is different from PMMA: for 10.3 and 34.0 kg/mol there is definitely a higher free volume fraction near the surface than in the bulk. For the other molecular weights no difference is found between the near surface region and the bulk.

The surface expansion coefficients for PS are not different from the bulk one for all molecular weights, which were investigated.

All in all, the dynamic measurements for both PMMA and PS reinforce the hypothesis that there are anomalies, invoked by confinement, which influence the glass temperature and the dynamic properties of the polymer at the surface. The relative values for $T_{\mathrm{dec},0}$, c_1, c_2, T_{inf}, the fragility, free volume and expansion coefficients indicate a different behavior near the surface than in the bulk. Molecular entanglements may also influence the material properties. The different interaction between the polymer chains determines the different character of the two polymers (difference of the glass temperature near the surface and in the bulk, fragility, free volume etc.).

6. DISCUSSION

6.1 Discussion of the PMMA Results

The results obtained from the quasi-static temperature ramp experiments performed in this work with PMMA reveal a reduction of T_{g} near the surface for the samples with molecular weights 65.0 kg/mol (Sec. 5.1.1). Explaining this via cooperation between the polymer chains, the coupling should become more effective for the larger molecular weights. The model describing differences at the surface via free volume fraction or chain end density would support a decreasing $T_{\mathrm{dec},0}$ with increasing molecular weight. A higher free volume with increasing molecular weight would go along with an increased fragility. The reduced average activation energy (Fig. 5.22) for the higher molecular weights thus implies that near the surface less energy is necessary to perform conformation changes than in the bulk. If the strong cooperation between the chains is the factor which determines whether the near-surface glass temperature is reduced or not, the fragility for the material with a reduced $T_{\mathrm{dec},0}$ should be small: *i.e.*, the material should be strong. Networks and strong cooperation lead to strong materials, just as in some of the strongest materials, SiO and GeO glasses. The mastering (Sec. 5.2.1) of the data obtained from the dynamic measurements provides the shift values. The Arrhenius plot of the shift values shows a decreasing temperature dependent activation energy with increasing molecular weight. This means the material for the low M_{w} is rather fragile than strong. PMMA with 65.0 kg/mol behaves strong near the surface. The fragility of the material was also analyzed fitting the shift values to the WLF equation. From the resulting WLF parameters a glass temperature can be determined, assuming that $c_1^g = 16 \pm 2$ ([Ang97]). Within the error the glass temperatures from the dynamic measurements the increased cooperation of the chains is also supported by a corresponding increase in the fragility. The surface value of $T_{\mathrm{dec},0}$ also decreases with respect to the bulk value during the crossover to a strong material at higher molecular weights. The free-volume fraction, as well as the expansion coefficient, shows no difference between the bulk and near the surface for PMMA. It appears that there is a strong

network with a low free-volume fraction and a high degree of cooperation near the surface of the 65.0 kg/mol PMMA samples.

6.2 Discussion of the PS Results

The laser-diffraction temperature-ramping experiments for PS (Sec. 5.1.1) only show a deviation of the near-surface $T_{\mathrm{dec},0}$ from the bulk T_{g} towards higher values for 3.47 and 10.3 kg/mol. The average activation energy for PS (Fig. 5.25) displays virtually neither a difference between the bulk and near the surface nor a molecular-weight dependence. For PS, the surface fragility follows almost the same trend as that of the bulk values; however, it is shifted to values closer to 1, implying a higher surface fragility. The surface values increase with molecular weight, up to 34.0 kg/mol. This could explain the lack of a near-surface effect, when measuring $T_{\mathrm{dec},0}$. The cooperation and interaction between the PS chains in the bulk is not as strong as in the case for PMMA. The free volume at the surface is even higher than in the bulk value at least for 10.3 and 34.0 kg/mol. Thus, an effect of the surface on the material properties as in the case of PMMA cannot be detected.

It is helpful to compare the results for PMMA and PS with values in the literature and also directly with each other to draw conclusions about the effects due to different materials.

6.3 Comparison PMMA and PS

The comparison of the near surface T_{g} with surface values taken from the literature for PMMA [GBL$^+$98], [Ham99], [FNdP00], [FPK$^+$01] and PS [STK99], [GPZ$^+$00], [Ham99], [GBL$^+$98] is presented in Fig. **??**. The error bars are not added to the graph for more clarity.

This graphical composition shows that the measured values are in the right temperature range. While a large number of publications deal with PS surface T_{g}, the literature values for

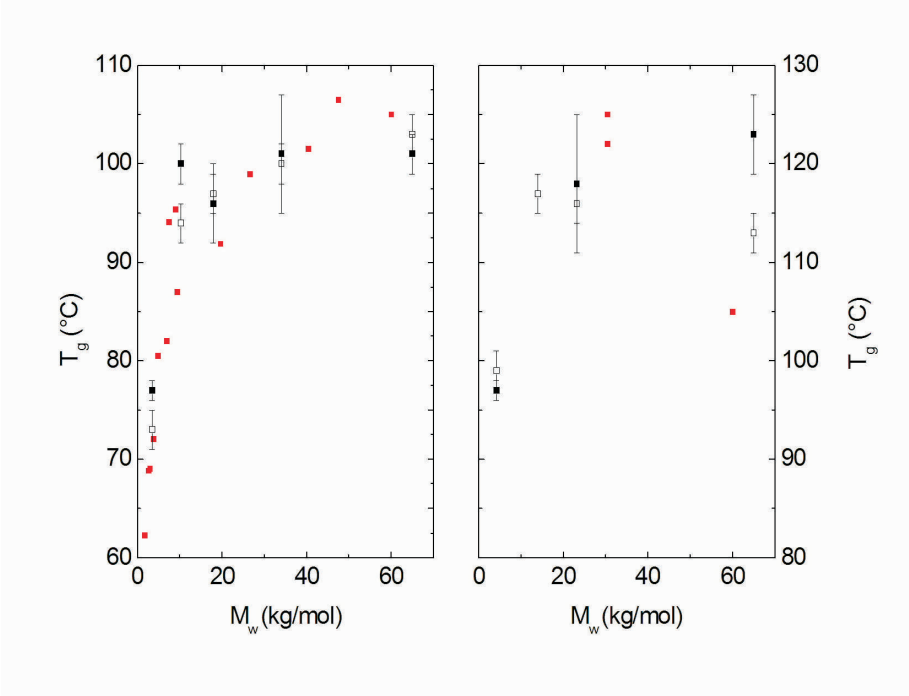

Figure 6.1: The near surface (solid squares with error bars) and bulk (open squares) data is plotted together with the literature values for PS [STK99], [GPZ+00], [Ham99], [GBL+98] (scattered squares) in the left graph. The same is done for the surface (solid squares) and bulk (open squares) data of PMMA [GBL+98], [Ham99], [FNdP00], [FPK+01] (scattered squares) in the right plot.

PMMA are very limited . The graphs also show, that the values for PS are all very close to the bulk values, while the low number of literature values for PMMA are scattered widely.

The reduction of the probing depth by a factor of 2.5 did not show a change in the T_{dec} at a rate of 1°C/min (5.1.2). A possible influence of the different probing technique, AFM instead of laser diffraction, could be excluded comparing the results of the investigation of larger gratings with both techniques.

The mastering of the dynamic data worked reasonably well for both PMMA and PS (5.2.1). The data for PS looks nicer since the imprinting technique was improved, which resulted in an increased diffracted intensity, and the data was averaged over a longer time interval. Both the PMMA and PS data showed additional peaks. They could be caused by capillary waves forming on the liquid surface of the polymer samples. An attempt to prove the formation of capillary waves by imprinting with a flat silicon master without corrugation was not successful, even though the same procedure was followed as done with the corrugated master.

The peaks could also come from density gratings, which develop after the decay of the corrugation gratings. This would be in analogy with the density gratings found by U. Pietsch *et al.* [PRN00]. They produced corrugation gratings by exposing dye-doped polymer films above T_g to laser-interference patterns and stabilizing the patterns which developed in the polymer by cooling them below T_g. After the thermally induced decay of these gratings they found density gratings.

The comparison of the average activation energies (5.2.2) with the bulk values published in literature is shown in Fig. 6.2. The range of the bulk values is indicated by the two dashed lines. The near surface PMMA values are much smaller than the corresponding bulk values. In the case of PS the range for the average activation energy near the surface and the bulk values from literature agree quite good in the range of the error.

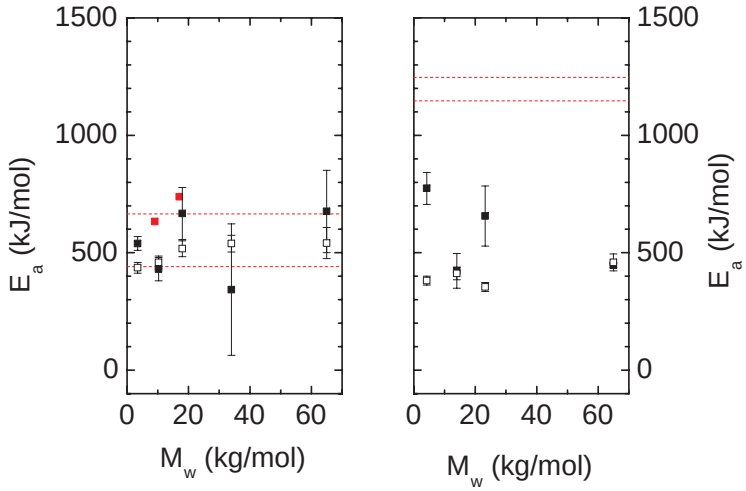

Figure 6.2: Comparison of average activation energies for PS (solid squares with error bars in the left hand graph) and PS (solid squares with error bars in the right hand graph) near the surface with bulk values (open squares and indicated by the range between the two dashed lines from literature [Hod94] and references therein). The two scattered points are for monodisperse PS from [PDL86]. The right plot shows the comparison of PMMA with the literature range indicated between the two dashed lines [Hod94].

The values of PMMA and PS are in the same energy range. The average activation energy for PMMA is smaller (stronger) than the literature values and rather decreases with molecular weight.

The resulting fragilities (5.2.3) for PMMA and PS are different for the smallest molecular weights (4.2 or 3.47 kg/mol, respectively) and the largest molecular weight (65.0 kg/mol). The fragility of PMMA is lower than the one of PS. The fragilities F (squares) and F(c(1)=16) (stars) are plotted for PMMA (black) and PS in Fig. 6.3.

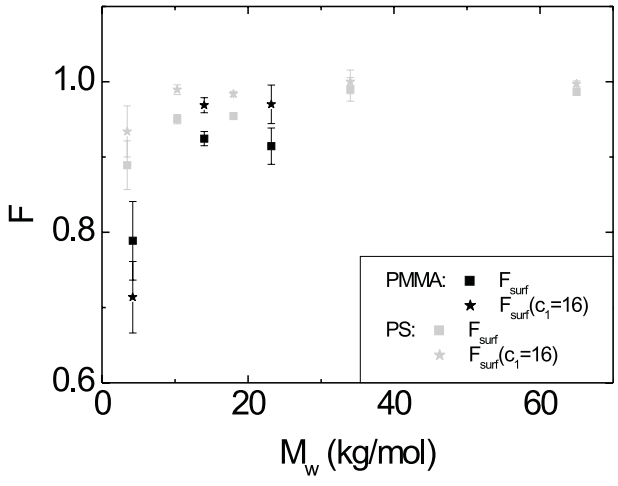

Figure 6.3: Fragilities F and F(c(1)=16) in dependence on molecular weight at the near surface for PMMA (solid dark squares and stars) and PS (solid grey squares and stars).

The values $\frac{1}{c_1}$ and $\frac{1}{c_1 c_1}$ of PMMA and PS, which are proportional to the free volume fraction and the expansion coefficient (5.2.4) show only a difference between the bulk and near the surface for PS of 10.3 and 34.0 kg/mol. The free volume near the surface is higher for these molecular weights.

Considering the reduced T_{g} for PMMA of 65.0 kg/mol near the surface, which does not occur for PS together with an decreased fragility and an increased free volume, one can conclude, that the strong cooperation, which is enhanced by a reduced free volume, is responsible for the surface effect. A small free volume constricts the spectrum of relaxation times and reduces the non-exponential behavior. The consequence is that the material is stronger. The surface effect does not occur for PS since the interaction between the chains is smaller than in the case of PMMA, and the free volume is larger due to the bulky side group. Strong means that network of cooperative units are formed and this property is more pronounced for PMMA near

the surface than for PS. The near surface region of 65.0 kg PMMA is stronger than the bulk. This points to a dense surface region. The anomaly for the high molecular weight PMMA value is seen in the T-ramping as well as in the decay measurements, which makes us confident in excluding it as an artifact.

7. CONCLUSIONS

The focus of this work was the investigation of anomalies in T_{g} and dynamics at polymer surfaces. The thermally induced decay of hot-embossed polymer gratings is studied using laser-diffraction and atomic force microscopy (AFM). Monodisperse PMMA and PS are selected in the M_{w} ranges of 4.2 to 65.0 kg/mol and 3.47 to 65.0 kg/mol, respectively. Two different modes of measurement were used: the one mode uses temperature ramps (Sec. 3.2.1) to obtain an estimate of the near-surface glass temperature, $T_{\mathrm{dec},0}$; the other mode investigates the dynamics (Sec. 3.2.2) at a constant temperature above T_{g}.

The temperature-ramp experiments (Sec. 5.1) reveal $T_{\mathrm{dec},0}$ values very close to the $T_{\mathrm{g,bulk}}$ values, as determined by differential scanning calorimetry (DSC). The PMMA of 65.0 kg/mol shows a decreased value of T_{g}, while the PS samples of 3.47 and 10.3 kg/mol ($M_{\mathrm{w}} < M_{\mathrm{e}}$) show a slightly increased near-surface T_{g}. The transition width between the onset of an amplitude reduction and a final state is smaller in the case of PS than in the case of PMMA. This suggests a higher degree of cooperation between the polymer chains for PMMA than for PS chains even near the surface.

A reduction of the investigated near-surface region (5.1.2) by using smaller grating constants and AFM did not show a change in the near-surface $T_{\mathrm{dec},0}$.

Decay experiments (Sec. 5.2) were performed at a variety of constant temperatures. Master plots are produced by shifting the decay curves, on the logarithmic time scale, with respect to a reference curve at T_{ref}. From this procedure shift factors were extracted.

An Arrhenius analysis of the shift factors reveals a decreasing non-Arrhenius (fragile) behavior with molecular weight for PMMA. PS is fragile for all M_{w} as expected for linear polymers. Non-Arrhenius behavior allows one to fit the shift factors to the William–Landel–Ferry (WLF) equation.

The WLF parameters for the varying molecular weights of PMMA and PS were extracted and compared to the values from bulk rheology measurements [PH]. Assuming $c_1^g = 16 \pm 2$

at T_{g}, as suggested by Angell [Ang97], the glass temperature was determined from the dynamic decay experiments. Within the experimental errors, the values for $T_{\mathrm{g,surf}}(c_1 = 16)$ and $T_{\mathrm{g,bulk}}(c_1 = 16)$ tend to be smaller than $T_{\mathrm{dec},0}$ and $T_{\mathrm{g,bulk}}$ from temperature-ramp and DSC measurements, but confirm the course of the values with increasing M_{w}.

The comparison of the fragilities (temperature dependence of the polymer properties at T_{g}) near the surface and in the bulk shows a higher fragility for PS near the surface, a lower one for PMMA with molecular weights of 4.2 and 65.0 kg/mol. The different surface behavior of PS is traced back to a lower degree of cooperation and a larger free volume fraction.

8. ZUSAMMENFASSUNG

Thema dieser Arbeit ist die Untersuchung von Anomalien nahe der Oberfläche eines Polymers. Der thermisch induzierte Zerfall von heiss gestempelten Polymergittern ist mit Hilfe von Beugungsexperimenten und Rasterkraftmikroskopie (AFM) beobachtet worden. Mit diesen Experimenten kann sowohl die Glastemperatur (T_{g}) als auch das dynamischen Verhalten nahe der Oberfläche bestimmt werden. Der Vergleich der Ergebnisse mit Volumenwerten gibt Hinweis auf den Einfluss der Oberfläche. Als Polymermaterial sind monodisperses PMMA mit Molekulargewichten (M_{w}) zwischen 4.2 und 65.0 kg/mol und monodisperses PS mit M_{w} zwischen 3.47 und 65.0 kg/mol ausgewählt worden. Zwei unterschiedliche Messmodi wurden verwendet: Der Messmodus zur Bestimmung der Glastemperatur nahe der Oberfläche, $T_{\mathrm{dec},0}$, verwendet Temperaturrampen (Abschnitt 3.2.1). Der zweite Messmodus dient zur Untersuchung des dynamischen Verhaltens nahe der Oberfläche (Abschnitt 3.2.2) bei konstanten Temperaturen oberhalb von T_{g}.

Aus den Experimenten mit Temperaturrampen (Abschnitt 5.1) ergeben sich Glastemperaturen $T_{\mathrm{dec},0}$ sehr ähnlich den Glastemperaturen des Volumens, $T_{\mathrm{g,bulk}}$, welche kalorimetrisch (DSC) bestimmt wurden. PMMA mit 65.0 kg/mol zeigt eine niedrigere und PS mit 3.47 und 10.3 kg/mol ($M_{\mathrm{w}} < M_{\mathrm{e}}$) eine höhere Glastemperatur nahe der Oberfläche als im Volumen. Die Breite des Übergangs ist die Temperaturdifferenz zwischen dem Einsetzen der Amplitudenänderung und dem Endzustand, bei dem kein Gitter mehr erkennbar ist. Sie ist geringer für PS als für PMMA. Dies weist auf einen stärkeren kooperativen Charakter im Falle von PMMA auch nahe der Oberfläche hin.

Der Oberflächenbereich, der beim Zerfall der Gitter untersucht wird, kann verringert werden, indem die Gitterkonstante reduziert wird (5.1.2). Die AFM Messungen eines etwa zweieinhalb mal dünneren Oberflächenbereichs zeigt jedoch keine Änderung von $T_{\mathrm{dec},0}$.

Die Beugungsexperimente wurden auch bei unterschiedlichen, konstanten Temperaturen durchgeführt (Abschnitt 5.2). Durch Verschieben der Zerfallskurven auf der logarithmischen

Zeitskala ausgehend von einer Referenzkurve (gemessen bei $T = T_{\mathrm{ref}}$), konnte eine einheitliche Kurve erzeugt werden, die Masterkurve.

Aus dem Masterprozess resultieren die Verschiebungsfaktoren. Sie können auf Arrhenius-Verhalten geprüft werden. Wie für lineare Polymere erwartet, zeigen die Verschiebungsfaktoren überwiegend kein Arrhenius-Verhalten. Das PS Material ist fragil und für PMMA nimmt die Fragilität mit steigendem M_{w} ab. Eine "starke" Ausnahme ist PMMA mit M_{w}=65.0 kg/mol, das Arrhenius-Verhalten zeigt. Vorausgesetzt, dass die Verschiebungsfaktoren nicht dem Arrhenius-Gesetz gehorchen, können sie mit der William-Landel-Ferry (WLF) Gleichung angefittet werden. Die WLF-Parameter wurden für PMMA and PS unterschiedlicher Molekulargewichte bestimmt und mit den entsprechenden Werten aus rheologischer Volumenmessungen [PH] verglichen. Nimmt man an, dass der WLF-Parameter $c_1^g = 16 \pm 2$ bei T_{g} ist, wie es von Angell [Ang97] vorgeschlagen wurde, kann die Glastemperatur aus den dynamischen Messungen bestimmt werden. $T_{\mathrm{g,surf}}(c_1 = 16)$ und $T_{\mathrm{g,bulk}}(c_1 = 16)$ sind tendenziell geringer als die entsprechenden $T_{\mathrm{dec},0}$ und $T_{\mathrm{g,bulk}}$ Werte aus den Messungen mit Temperaturrampen und DSC aber zeigen einen ähnlichen Verlauf.

Der Vergleich der Fragilitäten (Temperaturabhängigkeiten der Polymereigenschaften nahe T_{g}) an der Oberfläche und im Volumen zeigt eine höhere Fragilität des PS an der Oberfläche. PMMA mit 4.2 und 65.0 kg/mol ist stärker nahe der Oberfläche als im Volumen. Dieser Unterschied kann durch ein größeres freies Volumen und eine geringere Kooperativität im Falle von PS im Vergleich mit PMMA erklärt werden.

9. OUTLOOK

Increasing the sensitivity of the measurements either by performing polarized diffraction and/or improving the detection of small grating constants further by high stability heating stages, feature tracking and masters with high periodicity and an adequate aspect ratio, could confirm the cooperative unit theory. It could give even more detailed insight into the size of cooperative units and the dynamic processes occurring at the surface. The ”fine structure” of the T-ramping data and also of the decay data could give more insight into the processes occurring at temperatures above the glass transition. The interesting dynamic processes are the formation and separation of cooperative units, the rotation of the side groups or the development of capillary or density waves near the surface. The processes should require different amounts of energy due to the different structure of PS and PMMA. The temperature ramps and also the decay curves showed peaks in the course of the diffracted intensity. An increase of the PSD was also seen in the AFM analysis and the surface of the polymer film became rougher, however, without a special periodicity. These peaks in the transition zone between the rubbery and liquid state raised speculations about the underlying processes which cause them. The investigation of the possible density gratings could be done by X-ray diffraction measurements at a synchrotron in combination with AFM surface measurements. The possibility to collect in situ AFM surface images while keeping the sample at a constant temperature and a successive PSD analysis could prove possible capillary waves.

10. APPENDIX

10.1 Ehrenfest Theorem

Assuming that

• the state functions volume V and entropy S are continuous at the glass transition

and

• S and V only depend on pressure and temperature both above an below the glass temperature

leads to the Ehrenfest equations (10.1), (10.2):

$$\frac{dT}{dp} = \frac{\Delta\kappa}{\Delta\alpha} \tag{10.1}$$

and

$$\frac{dT}{dp} = \frac{TV\Delta\alpha}{\Delta C_{\mathrm{p}}} \tag{10.2}$$

$\Delta\kappa$ is the difference between the isothermal compressibilities of the liquid and the glass. Equating the two relations results in the Ehrenfest relation (10.3):

$$\frac{\Delta\kappa\Delta C_{\mathrm{p}}}{TV\Delta\alpha^2} = 1 \tag{10.3}$$

The left hand side of equation (10.3) is referred to as the Prigogine-Defay ratio. Davies and Jones [DJ53] showed that this ratio is larger than one for glass-forming materials and the Ehrenfest relation is not true for these materials.

ACKNOWLEDGEMENTS

Last but not least I want to thank the people, who supported me and contributed to my work both scientifically and personally.
Thank you to:

- my adviser Prof. D. Johannsmann who provided the interesting topic, a forum for discussions and made me focus on the important things.
- Prof. W. Knoll, who gave me the chance to do my PhD in his exceptional group.
- Prof. T. Pakula and A. Hanewald, who provided the bulk rheology measurements and discussions about polymer dynamics.
- Andreas Hund, Chun Wang from the group of Prof. T. Krausch, Bayreuth, who provided the stepped silicon masters.
- Zhihong Zhang, who deposited some PTFE-like films.
- G. Dvorak who performed the DSC measurements.
- B. Menges for helpful questions, discussions and small lithographic gratings.
- M. Hamdorf for some of the large lithographic gratings.
- Herr Richter for all the helpful hints and discussions about temperature controlling and laser detection.
- Dr. S. Berg for helpful discussions, computer support and the team spirit.
- Dr. T. Dimitrova, the soul of our office and expert of foreign languages, who taught me the scientific language for advanced.
- Dr. ”Scott Ferguson” S. Fraser and Dr. Tommy Burch for smoothing the twist and turns in my English sentences, when proof reading my thesis.

- everybody who supported me working on my PhD, especially the ”interbar crowd”: Ralf, Toby, Menno, Thomas the whistler, Fernando, Alessandro, Lisa, Colin, Tania, Thomas Jakob, Stephan, Volker, Jörn, ...(please do not be mad if I forgot somebody)
- both my parents, who always supported my interests, projects, dreams and goals and my brothers who taught me early to enjoy working in a mens’ domain.
- Tommy Burch the person who has supported my critical thinking and helped me keep my balance of mind.
- the Deutsche Forschungs Gemeinschaft (DFG) for financial support.

List of Figures

Bibliography

[AG65] G. Adam and J. H. Gibbs. On the temperature dependence of cooperative relaxation properties in glass-forming liquids. *J. Chem. Phys.*, 43:139, 1965.

[Ang88] C. A. Angell. *J. Phys. Chem. Solids*, 49:863, 1988.

[Ang97] C. A. Angell. Why c_1=16-17 in the WLF equation is physical – and the fragility of polymers. *Polymer*, 38:6261–6266, 1997.

[Ang98] C. A. Angell. *Entropy, Landscapes, and Fragility in Liquids and Polymers, and the ΔC_{p} Problem*, chapter 3, pages 37–53. ACS Symposium Series 710. American Chemical Society, San Francisco, California, Apr. 1998.

[ANK95] A. Z. Akcasu, G. Nägele, and R. Klein. Remarks on the ”fast” and ”slow” mode theories of interdiffusion. *Macromolecules*, 28:6680–6683, 1995.

[ANM+00] C. A. Angell, K. L. Ngai, G. B. MacKenna, P. F. McMillan, and S. W. Martin. Relaxation in glassforming liquids and amorphous solids. *J. Appl. Phys.*, 88(6):3113–3157, Sept. 2000.

[ARA+95] P. Argitis, I. Raptis, C. J. Aidinis, N. Glezos, M. Baciocchi, J. Everett, and M.Hatzakis. An advanced epoxy Novolac resist for fast high-resolution electron-beam lithography. *J. Vac. Sci. Technol. B*, 13(6):3030–3034, Nov./Dez. 1995.

[BA92] R. Böhmer and C. A. Angell. *Phys. Rev. B*, 45:10091, 1992.

[Bas98] J. Baschnagel. *Dynamic Properties of Polymer Melts above the Glass Transition: Monte Carlo Simulations*, chapter 4, pages 53–77. ACS Symposium Series 710. American Chemical Society, San Francisco, California, 1998.

[BBPB00] J. Baschnagel, C. Bennemann, W. Paul, and K. Binder. Dynamics of a supercooled polymer melt above the mode-coupling critical temperature: cage versus polymer-specific effects. *J. Phys.: Condens. Matter*, 12:6365–6374, 2000.

[BCW+98] D. W. Branch, J. M. Corey, J. A. Weyhenmeyer, G. J. Brewer, and B. C. Wheeler. Microstamp patterns of biomolecules for high-resolution neuronal networks. *Med. Biol. Eng. and Comput.*, 36:135–141, 1998.

[BGS84] U. Bengtzelius, W. Götze, and A. Sjölander. Dynamics of supercooled liquids and the glass transition. *J. Phys. C*, 17(33):5915–5934, 1984.

[BNAP93] R. Böhmer, K. L. Ngai, C. A. Angell, and D. J. Plazek. Nonexponential relaxations in strong and fragile glass formers. *J. Phys. Chem.*, 99(5):4201–4209, Sept. 1993.

[BPBB99] C. Bennemann, W. Paul, J. Baschnagel, and K. Binder. Investigation of the influence of different thermodynamic paths on the structural relaxation in a glass-forming polymer. *J. Phys.: Condens. Matter*, 11:2179–2192, 1999.

[Büc55] F. Büche. *J. Appl. Phys.*, 26:738, 1955.

[CFG87] R. H. Colby, L. J. Fetters, and W. W. Graessley. *Macromolecules*, 20:2226, 1987.

[CG79] M. Cohen and G. Grest. *Phys. Rev. B*, 20:1077, 1979.

[CK97] S. Y. Chou and P. R. Krauss. Imprint lithography with sub-10 nm feature size and high throughput. *Microel. Eng.*, 35:237–240, 1997.

[CKR95] S. Y. Chou, P. R. Krauss, and P. J. Renstrom. Imprint of sub-25 nm vias and trenches in polymers. *Appl. Phys. Lett.*, 67(21):3114, Nov. 1995.

[CKR96] S. Y. Chou, P. R. Krauss, and P. J. Renstrom. Imprint lithography with 25-nanometer resolution. *Science*, 272:85–87, Apr. 1996.

[CMLP97] Z. Cui, R. A. Moody, I. M. Loader, and P. D. Prewett. Optimized process for electron beam nanolithography using AZPN 114 chemically amplified resisit. *Microel. Eng.*, 35:145–148, 1997.

[CP98] Z. Cui and P. D. Prewett. Proximity correction of chemically amplified resists for electron beam lithography. *Microel. Eng.*, 41/42:183–186, 1998.

[CT59] M. Cohen and D. Turnbull. *J. Chem. Phys.*, 31:1164, 1959.

[CT61] M. Cohen and D. Turnbull. *J. Chem. Phys.*, 34:120, 1961.

[CT70] M. Cohen and D. Turnbull. On the free-volume mode of the liquid-glass transition. *J. Chem. Phys.*, 52(6):3041, 1970.

[CWS90] K. G. Chiong, S. Wind, and D. Seeger. Exposure characteristics of high-resolution negative resists. *J. Vac. Sci. Technol. B*, 8(6):1447–1453, Nov./Dec. 1990.

[DFG97] G. B. DeMaggio, W. E. Frieze, and D. W. Gidley. Interface and surface effects on the glass transition in thin polystyrene films. *Phys. Rev. Lett.*, 78(8):1524–1527, Feb. 1997.

[DFM+98] E. A. Dobisz, T. N. Fedynyshyn, D. Ma, L. M. Shirey, and R. Bass. Electron-beam nanolithography, acid diffusion, and chemical kinetics in SAL-601. *J. Vac. Sci. Technol. B*, 16(6):3773–3778, Nov./Dec. 1998.

[dG81] P. G. de Gennes. *Journal de Physique*, 42:473–477, 1981.

[dG85] P. G. de Gennes. Wetting: statics and dynamics. *Rev. Mod. Phys.*, 57(3):827–863, July 1985.

[DGP+99] C. Donati, S. Glotzer, P. H. Poole, W. Kob, and S. J. Plimpton. Spatial correlations of mobility and immobility in a glass-forming Lennard–Jones liquid. *Phys. Rev. E*, 60:3119, 1999.

[DJ53] R. O. Davies and G. O. Jones. *Adv. Phys.*, 2:370–410, 1953.

[Doi96] M. Doi. *Introduction to Polymer Physics*. Oxford University Press, 1996.

[DSTR99] P. G. Debenedetti, F. H. Stillinger, T. M. Truskett, and C. J. Roberts. The equation of state of an energy landscape. *J. Phys. Chem. B*, 103:7390–7397, 1999.

[DVND99] K. Dalnoki-Veress, B. G. Nickel, and J. R. Dutcher. Dispersion-driven morphology of mechanically confined polymer films. *Phys. Rev. Lett.*, 82(7):1486–1489, Feb. 1999.

[EWO+02] M. Y. Efremov, J. T. Warren, E. A. Olson, M. Zhang, A. T. Kwan, and L. H. Allen. Thin-film differential scanning calorimetry: A new probe for assignment of the glass transition of ultrathin polymer films. *Macromolecules*, 35(5):1481, Feb. 2002.

[FBL+00] C. Fradin, A. Braslau, D. Luzet, D. Smilgies, M. Alba, N. Boudet, K. Mecke, and J. Daillant. Reduction in the surface energy of liquid interfaces at short length scales. *Nature*, 403:871–874, Feb. 2000.

[FDVD97] J. A. Forrest, K. Dalnoki-Veress, and J. R. Dutcher. Interface and chain confinement effects on the glass transition temperature of thin polymer films. *Phys. Rev. E*, 56(5):5705–5716, Nov. 1997.

[FDVSD96] J. A. Forrest, K. Dalnoki-Veress, J. R. Stevens, and J. R. Dutcher. Effect of free surfaces on the glass transition temperature of thin polymer films. *Phys. Rev. Lett.*, 77(10):2002, Sept. 1996.

[Fer80] J. D. Ferry. *Viscoelastic Properties of Polymers*, volume 3, chapter 11, pages 289–291. Wiley & Sons, Inc., New York, Chichester, Brisbane, Toronto, 3rd edition, 1980.

[FM00a] J. A. Forrest and J. Mattsson. Reductions of the glass transition temperature in thin polymer films: Probing the length scale of cooperative dynamics. *Phys. Rev. E*, 61(1):R53–R56, Jan. 2000.

[FM00b] K. Fukao and Y. Miyamoto. Glass transition and dynamics in thin polymer films: Dielectric relaxation of thin films of polystyrene. *Phys. Rev. E*, 61(2):1743–1754, Feb. 2000.

[FNdP00] D. S. Fryer, P. F. Nealey, and J. J. de Pablo. Thermal probe measurements of the glass transition temperature for ultrathin polymer films as a function of thickness. *Macromolecules*, 33:6439, 2000.

[FPK+01] D. S. Fryer, R. D. Peters, E. J. Kim, J. E. Tomaszewski, J. J. de Pablo, and P. F. Nealey. Dependence of the glass transition temperature of polymer films on interfacial energy and thickness. *Macromolecules*, 34:5627, 2001.

[Ful25] G. S. Fulcher. Analysis of recent measurements of the viscosity of glasses. *J. Am. Chem. Soc.*, 8:339, 1925.

[GBL+98] Y. Grohens, M. Brogly, C. Labbe, M.-O. David, and J. Schultz. Glass transition of stereoregular poly(methyl methacrylate) at interfaces. *Langmuir*, 14(11):2929, May 1998.

[GD58a] J. Gibbs and E. DiMarzio. *J. Chem. Phys.*, 28:373, 1958.

[GD58b] J. Gibbs and E. DiMarzio. *J. Chem. Phys.*, 28:807, 1958.

[GMF+01] J. Gierak, D. Mailly, G. Faini, J. L. Pelouard, P. Denk, F. Pardo, J. Y. Marzin, A. Septier, G. Schmid, J. Ferre, R. Hydman, C. Chappert, J. Flicstein, B. Gayral, and J. M. Gerard. Nano-fabriction with focused ion beams. *Microel. Eng.*, 57-58:865–875, 2001.

[GNPJ97] M. Geoghean, T. Nicolai, J. Penfold, and R. A. L. Jones. Kinetics of surface segregation and the approach to wetting in an isotopic polymere blend. *Macromolecules*, 30:4220–4227, 1997.

[GPZ+00] S. Ge, Y. Pu, W. Zhang, M. Rafailovich, J. Sokolov, C. Buenviaje, R. Buckmaster, and R. M. Overney. Shear modulation force microscopy study of near surface glass transition temperatures. *Phys. Rev. Lett.*, 85(11):2340, Sept. 2000.

[GS92] W. Götze and A. Sjölander. *Rep. Prog. Phys.*, 55:241, 1992.

[GS95] W. Götze and A. Sjölander. *Transp. Theory Stat. Phys.*, 24:801, 1995.

[GSG+00] T. Geue, M. Schultz, J. Grenzer, U. Pietsch, A. Natansohn, and P. Rochon. X-ray investigations of molecular mobility with polymer surface gratings. *J. Appl. Phys.*, 87(11):7712–7719, June 2000.

[GSS96] P. Gröning, A. Schneuwly, and L. Schlapbach. "Self-thickness-limited" plasma polymerization of an ultrathin antiadhesive film. *J. Vac. Sci. Technol. A*, 14(6):3043–3048, Nov./Dec. 1996.

[Ham99] Mark Hamdorf. *Beweglichkeit Polymerer Glasbildner an Grenzflächen*. PhD thesis, Johannes Gutenberg Universität, Mainz, Mar. 1999.

[Hec98] S. Hector. Status and future of X-ray lithography. *Microel. Eng.*, 41/42:25–30, 1998.

[Her99] S. Herminghaus. Dynamical instability of thin liquid films between conducting media. *Phys. Rev. Lett.*, 83(12):2359–2361, Sept. 199.

[HGH99] J. A. Hammerschmidt, W. L. Gladfelter, and G. Haugstad. Probing polymer viscoelastic relaxations with temperature-controlled friction force microscopy. *Macromolecules*, 32:3360, 1999.

[HHG] G. Haugstad, J. A. Hammerschmidt, and W. L. Gladfelder. Viscoelasticity in nanoscale friction on thin polymer films.

[HJ00] M. Hamdorf and D. Johannsmann. Surface-rheological measurements on glass forming polymers based on the surface tension driven decay of imprinted corrugation gratings. *J. Chem. Phys.*, 112(9):4262, Mar. 2000.

[HMG96] J. A. Hammerschmidt, B. Moasser, and W. L. Gladfelter. Polymer viscoelastic properties measured by friction force microscopy. *Macromolecules*, 29:8996–8998, 1996.

[Hod87] I. M. Hodge. Effect of annealing and prior history on enthalpy relaxation in glassy polymers. 6. Adam–Gibbs formulation of nonlinearity. *Macromolecules*, 20:2897, 1987.

[Hod94] I. M. Hodge. Enthalpy relaxation and recovery in amorphous materials. *J. Non-Crystal. Solids*, 169:211–266, 1994.

[HPP91] J. L. Harden, H. Pleiner, and P. A. Pincus. Hydrodynamic surface modes on concentrated polymer solutions and gels. *J. Chem. Phys.*, 94(7):5208–5221, Apr. 1991.

[JSGS98] R. W. Jaszeweski, H. Schift, J. Gobrecht, and P. Smith. Hot embossing in polymers as a direct way to pattern resist. *Microel. Eng.*, 41/42:575–578, 1998.

[JSS+99] R. W. Jaszewski, H. Schift, B. Schnyder, A. Schneuwly, and P. Gröning. The deposition of anti-adhesive ultra-thin teflon-like films and their interaction with polymers during hot embossing. *Appl. Surf. Sci.*, 143:301–308, 1999.

[JYT+01] X. Jiang, C. Z. Yang, K. Tanaka, A. Takahara, and T. Kajiyama. Effect of chain end group on surface glass transition temperature of thin polymer films. *Physics Letters A*, 281:363, 2001.

[KA95] W. Kob and H. C. Anderson. Testing mode-coupling theory for a supercooled binary Lennard–Jones mixture: the van Hoove correlation function. *Phys. Rev. E*, 51:4626–4641, 1995.

[Kau48] W. Kauzmann. The nature of the glassy state and the behavior of liquids at low temperatures. *Chem. Rev.*, 43:219–256, 1948.

[KC97] P. R. Krauss and S. Y. Chou. Nano-compact disks with 400 $Gbit/in^2$ storage density fabricated using nanoimprint lithography and read with proximal probe. *Appl. Phys. Lett.*, 71(21):3174, Nov. 1997.

[KDP+97] W. Kob, C. Donati, S. J. Plimpton, P. H. Poole, and S. C. Glotzer. Dynamical heterogeneities in a supercooled Lennard–Jones liquid. *Phys. Rev. Lett.*, 79(15):2827, Oct. 1997.

[KhHL99] D.-Y. Khang and h. H. Lee. Wafer-scale sub-micron lithography. *Appl. Phys. Lett.*, 75(17):2599, Oct. 1999.

[KJ01] S. Kawana and R. A. L. Jones. Character of the glass transition in thin supported polymer films. *Phys. Rev. E*, 63:021501, 2001.

[KJC94] J. L. Keddie, R. A. L. Jones, and R. A. Corey. *Faraday Discussions*, 98:219, 1994.

[KKI75] R. G. Kirste, W. A. Kruse, and K. Ibel. Determination of the conformation of polymers in the amorphous solid state and in concentrated solution by neutron diffraction. *Polymer*, 16:120, 1975.

[KL00] D.-Y. Khang and H. H. Lee. Room-temperature imprint lithography by solvent vapor treatment. *Apll. Phys. Lett.*, 76(7):870–872, Feb. 2000.

[KLKR01] T. Kerle, Z. Q. Lin, H. C. Kim, and T. P. Russell. Mobility of polymers at the air/polymer interface. *Macromolecules*, 34:3484, 2001.

[Koh74] R. Kohlrausch. Theorie des elektrischen Rückstandes in der Leidener Flasche. *Ann. Phys. Chem.*, 91:179–214, 1874.

[Kov64] A. J. Kovac. *Adv. Polym. Sci.*, 3:394, 1964.

[KRL$^+$] H. Kim, A. Rühm, L. B. Lurio, J. K. Basu, S. K. Sinha, D. Lumma, and S. F. J. Mochrie. Surface dynamics of polystyrene films. *IMMYT-Whitehead-Cat*, Sector 8.

[KTST98] T. Kajiyama, K. Tanaka, N. Satomi, and A. Takahara. Surface relaxation process of monodisperse polystyrene film based on lateral force microscopic measurements. *Macromolecules*, 31:5150, 1998.

[KTT97] T. Kajiyama, K. Tanaka, and A. Takahara. Surface molecular motion of the monodisperse polystyrene films. *Macrolecules*, 30:280, 1997.

[LFH$^+$99] S. Lüscher, A. Fuhrer, R. Held, T. Heinzel, and K. Ensslin. In-plane gate single-electron transistor in Ga[Al]As fabricated by scanning probe lithography. *Appl. Phys. Lett.*, 75(8):1134–1136, Aug. 1999.

[LFW78] H. W. Lehmann, K. Frick, and R. Widmer. Reactive sputtering of PTFE films in argon–CF_4 mixtures. *Thin Solid Films*, 52:231–235, 1978.

[LM96] T. P. Lodge and M. Muthukumar. *J. Phys. Chem.*, 100:13275, 1996.

[LRS$^+$97] Y. Liu, T. P. Russell, M. G. Samant, J. Stöhr, H. R. Brown, A. Cossy-Favre, and J. Diaz. Surface relaxations in polymers. *Macromolecules*, 30:7768–7771, 1997.

[Mar96] J. E. Mark. *Physical Properties of Polymers Handbook*. AIP Press, New York, 1996.

[MG00] J.-L. Masson and P. F. Green. Pattern formation in thin polymer films: A new morphology. *Mat. Res. Soc. Symp.*, 629, 2000.

[MIST$^+$01] C. Morin, H. Ikeura-Sekiguchi, T. Tyliszczak, R. Dornelius, J. L. Brash, A. P. Hitchcock, A. Scholl, F. Nolting, G. appel, D. A. Winesett, and K. Kaznacheyev. X-ray spectromicroscopy of immiscible polymer blends: Polystyrene-poly(methyl methacrylate). *J. Electron Spectroscopy*, 121:203, 2001.

[Mit93] V. S. Mitlin. Dewetting of solid surfaces: Analogy with sinodal decomposition. *J. Coll. Interface Science*, 156:491–497, 1993.

[Moy94] C. T. Moynihan. Assignment of the glass transition. In R. J. Seyler, editor, *ASTM STP 1249*, pages 32–49, Philadelphia, 1994. American Society for Testing and Materials.

[MR67] N. G. McCrum and B. E. Read. *Anelastic and Dielectric Effects in Polymeric Solids*. Dover, New York, 1967.

[MT97] D. Macintyre and S. Thoms. High resolution electron beam lithography studies on Shipley chemically amplified DUV. *Microel. Eng.*, 35:213–216, 1997.

[NFC+99] A. Notargiacomo, V. Foglietti, G. Capellini, M. Adami, P. Faraci, F. Evangelisti, and C. Nicolini. Atomic force microscopy lithography as a nanodevice development technique. *Nanotechnology*, 10:458–463, 1999.

[NKCD92] S. Nowak, O. K. Küttel, M. Collaud, and G. Dietler. Electron cyclotron resonance plasma experiment for in situ surface modification, deposition, and analysis. *J. Vac. Sci. Technol. A*, 10(6):3419–3425, Nov./Dec. 1992.

[NRP98] K. L. Ngai, A. K. Rizos, and D. J. Plazek. *J. Non-Cryst. Solids*, 235:435, 1998.

[NSS+00] E. La Nave, A. Scala, F. W. Starr, F. Sciortino, and H. E. Stanley. *Phys. Rev. Lett.*, 84:4605, 2000.

[OBK82] J. M. O'Reilly, H. E. Blair, and F. E. Karasz. Thermodynamic properties of stereoregular poly(methyl methacrylate). *Macromolecules*, 15:1083, 1982.

[OBLD00] R. M. Overney, C. Buenviaje, R. Luginbuhl, and F. Dinelli. Glass and structural transitions measured at polymer surfaces on the nanosacale. *Journal of Thermal Analysis and Calorimetry*, 59:205, 2000.

[OBT+98] L. E. Ocola, C. J. Biddick, D. M. Tennant, W. K. Waskiewicz, and A. E. Novembre. Negative chemically amplified resist characterization for direct write and SCALPEL nanolithography. *J. Vac. Sci. Technol. B*, 16(6):3705–3708, Nov/Dec 1998.

[PCT99] M. Poppeller, E. Cartier, and R. M. Tromp. Hot electron emission lithography: A method for efficient large area e-beam projection. *Microel. Eng.*, 46:183–186, 1999.

[PDL86] V. P. Privalko, S. S. Demchenko, and Y. S. Liptov. Structure-dependent enthalpy relaxation at the glass transition in polystyrenes. *Macromolecules*, 19:901–904, 1986.

[PH] T. Pakula and A. Hanewald. bulk rheological measurements.

[PLSW01] D. J. Pochan, E. K. Lin, S. K. Satija, and W.-L. Wu. Thermal expansion of supported thin polymer films: A direct comparison of free surface vs. total confinement. *Macromolecules*, 34:3041–3045, 2001.

[PN96] D. J. Plazek and K. L. Ngai. *Physical Properties of Polymers Handbook*, chapter 12. AIP Press, New York, 1996.

[PRN00] U. Pietsch, P. Rochon, and A. Natansohn. Formation of buried lateral density grating in azobenzene polymer films. *Advanced Materials*, 12(15):1129–1132, Aug. 2000.

[Rou53] P. E. Rouse. *J. Chem. Phys.*, 21:1272, 1953.

[RWH+01] N. Rehse, C. Wang, M. Hund, M. Geoghegan, R. Magerle, and G. Krausch. Stability of thin polymer films on a corrugated substrate. *Eur. Phys. J. E*, 4:69–76, 2001.

[SDS98] S. Sastry, P. G. Debenedetti, and F. H. Stillinger. Signatures of distinct dynamical regimes in the energy landscape of a glass-forming liquid. *Nature*, 393:554–557, June 1998.

[SHdMG01] H. Schift, L. J. Heyderman, M. Auf der Maur, and J. Gobrecht. Pattern formation in hot embossing of thin polymer films. *Nanotechnology*, 12:173–177, 2001.

[She00] S. S. Sheiko. *Imaging of Polymers Using Scanning Force Microscopy: From Superstructures to Individual Molecules*, volume 151 of *Advances in Polymer Science*. Springer-Verlag, 2000.

[SHJ01] R. Seemann, S. Herminghaus, and K. Jacobs. Dewetting patterns and molecular forces: A reconciliation. *Phys. Rev. Lett.*, 86(24):5534–5537, June 2001.

[SHS+89] K. J. Steward, M. Hatzakis, J. M. Shaw, D. E. Seeger, and E. Neumann. Simple negative resist for deep ultraviolet, electron beam, and X-ray lithography. *J. Vac. Sci. Technol. B*, 7(6):1734–1739, Nov./Dec. 1989.

[SJDG99] H. Shift, R. W. Jaszewski, C. David, and J. Gobrecht. Nanostructuring of polymers and fabrication of interdigitated electrodes by hot embossing lithography. *Microel. Eng.*, 46:121–124, 1999.

[SPT+95] M. Saillard, E. Popov, L. Tsonev, L. Scandella, and N.Kruse. Light-diffraction from rough gratings. *Applied Optics*, 34(22):4883–4891, Aug. 1995.

[SR98] P. F. Santangelo and C. M. Roland. Molecular weight dependence of fragility in polystyrene. *Macromolecules*, 31:4581, 1998.

[Ste98] J. Stecki. Extended capillary wave theory and the ellipsometric coefficient. *J. Chem. Phys.*, 109(12):5002–5007, Sept. 1998.

[STK99] N. Satomi, A. Tanakahara, and T. Kajiyama. Determination of surface glass transition temperature of monodisperse polystyrene based on temperature dependent scanning viscoelasticity microscopy. *Macromolecules*, 32:4474, 1999.

[Tan00] H. Tanaka. Viscoelastic phase separation. *J. Phys.: Condens. Matter*, 12:R207–R264, 2000.

[TFP+01] R. S. Tate, D. S. Fryer, S. Pasqualini, M. F. Montague, J. J. de Pablo, and P. F. Nealey. Extraordinary elevation of the glass transition temperature of thin polymer films grafted to silicon oxide substrates. *J. Chem. Phys.*, 115(21):9982, Dec. 2001.

[TH26] G. Tammann and W. Hesse. Die Abhängigkeit der Viskosität von der Temperatur bei unterkühlten Flüssigkeiten. *Z. Anorg. Allg. Chem.*, 156:245–247, 1926.

[TNdP00] J. Torres, P. Nealey, and J. de Pablo. Molecular simulation of ultrathin polymeric films near the glass transition. *Phys. Rev. Lett.*, 85:3221, 2000.

[TOG86] J. J. Tribone, J. M. O'Reilly, and J. Greener. Analysis of enthalpy relaxation in poly(methyl methacrylate): Effect of tacticity, deuteration, and thermal history. *Macromolecules*, 19:1732, 1986.

[TSI99] K. Takahara, H. Saito, and T. Inoue. Physical aging in poly(methyl methacrylate) glass: Densification via density fluctuation. *Polymer*, 40(13):3729–3733, June 1999.

[TTD00] K. C. Tseng, N. J. Turro, and C. J. Durning. Tracer diffusion in thin polystyrene films. *Polymer*, 41:4751–4755, 2000.

[TTG+96] K. Tanaka, A. Taura, S.-R. Ge, A. Takahara, and T. Kajiyama. Molecular weight dependence of surface dynamic viscoelastic properties for the monodisperse polystyrene film. *Macromolecules*, 29:3040, 1996.

[TTK97] K. Tanaka, A. Takahara, and T. Kajiyama. Effect of polydispersity on surface molecular motion of polystyrene films. *Macromolecules*, 30:6626, 1997.

[TTK00] K. Tanaka, A. Takahara, and T. Kajiyama. Rheological analysis of surface relaxation process of monodisperse polystyrene films. *Macromolecules*, 33:7588, 2000.

[TZ01] O. K. C. Tsui and H. F. Zhang. Effects of chain ends and chain entanglement on the glass transition temperature of polymer thin films. *Macromolecules*, 34:9139, 2001.

[VBB02] F. Varnik, J. Baschnagel, and K. Binder. Reduction of the glass transition temperature in polymer films: A molecular dynamics study. *Phys. Rev. E*, 65(2):021507/1–14, Feb. 2002.

[Vog21] H. Vogel. Das Temperaturabhängigkeitsgesetz der Viskosität von Flüssigkeiten. *Phys. Zeit.*, 22:645–646, 1921.

[WCBB99] B. C. Wheeler, J. M. Corey, G. J. Brewer, and D. W. Branch. Microcontact printing for precise control of nerve cell growth in culture. *J. Biomech. Eng.*, 121:73–78, Feb. 1999.

[WLF55] M. L. Williams, R. F. Landel, and J. D. Ferry. The temperature dependence of relaxation mechanisms in amorphous polymers and other glass-forming liquids. *J. Am. Chem. Soc.*, 77(14):3701, July 1955.

[WQSK98] K. Wilder, C. F. Quate, B. Singh, and D. F. Kyser. Electron beam and scanning probe lithography: A comparison. *J. Vac. Sci. Technol. B*, 16(6):3864–3873, Nov./Dec. 1998.

[WSY97] F. Wang, S. Saeki, and T. Yamaguchi. Temperature and pressure dependence of thermal expansion coefficient and thermal pressure coefficient for amorphous polymers. *Polymer*, 38(14):3485–3492, 1997.

[Wu70] S. Wu. Surface and interfacial tensions of polymer melts poly(methyl methacrylate), poly(n-butyl methacrylate), and polystyrene. *J. Chem. Phys.*, 74:632–638, 1970.

[WW70] G. Williams and D. C. Watts. Non-symmetrical dielectric relaxation behavior arising from a simple empirical decay function. *Trans. Faraday Soc.*, 66:80–85, 1970.

[WZW95] W. E. Wallace, J. H. Zanten, and W. L. Wu. Influence of an impenetrable interface on a polymer glass-transition temperature. *Phys. Rev. E*, 52(4):R3329–R3332, Oct. 1995.

[ZAL+97] C. E. Zybill, H. G. Ang, L. Lan, W. Y. Choy, and E. F. K. Meng. Monomolecular silane films on glass surfaces - contact angle measurements. *J. Organometallic Chem.*, 547:167–172, 1997.

[Zim56] B. H. Zimm. *J. Chem. Phys.*, 24:269, 1956.

[ZRS97] X. Zheng, M. H. Rafailovich, and J. Sokolov. Long-range effects on polymer diffusion induced by a bounding interface. *Phys. Rev. Lett.*, 79(2):241, July 1997.

The following papers were published during the time of the PhD:

K. Petersen, D. Johannsmann
Measurements of the surface glass temperature of PMMA from the decay of imprinted surface corrugation gratings: the influence of molecular weight
J. Non-Cryst. Solids **307-310**, *(2002) 532-537*